ANALYSIS OF ARCING FAULTS ON DISTRIBUTION LINES FOR PROTECTION AND MONITORING

A Thesis Submitted for the Degree of
Master of Engineering

by

Karel Jansen van Rensburg, B.Eng.

School of Electrical and Electronic Systems Engineering
Queensland University of Technology

2003

Keywords:

Arcing; breaking conductor; conductor dynamics; conductor swing; distance protection; downed conductor; fault locator; fault identification; fault voltage; high impedance faults; overhead line monitoring; overhead line protection; power quality; voltage dips; voltage sags

Abstract

This thesis describes an investigation into the influences of arcing and conductor deflection due to magnetic forces on the accuracy of fault locator algorithms in electrical distribution networks. The work also explores the possibilities of using the properties of an arc to identify two specific types of faults that may occur on an overhead distribution line.

A new technique using the convolution operator is introduced for deriving differential equation algorithms. The first algorithm was derived by estimating the voltage as an array of impulse functions while the second algorithm was derived using a piecewise linear voltage signal. These algorithms were tested on a simulated single-phase circuit using a PI-model line. It was shown that the second algorithm gave identical results as the existing dynamic integration operator type algorithm. The first algorithm used a transformation to a three-phase circuit that did not require any matrix calculations as an equivalent sequence component circuit is utilised for a single-phase to ground fault. A simulated arc was used to test the influence of the non-linearity of an arc on the accuracy of this algorithm. The simulations showed that the variation in the resistance due to arcing causes large oscillations of the algorithm output and a 40^{th} order mean filter was used to increase the accuracy and stability of the algorithm. The same tests were performed on a previously developed fault locator algorithm that includes a square-wave power frequency approximation of the fault arc. This algorithm gave more accurate and stable results even with large arc length variations.

During phase-to-phase fault conditions, two opposing magnetic fields force the conductors outwards away from each other and this movement causes a change in the total inductance of the line. A three dimensional finite element line model based on standard wave equations but incorporating magnetic forces was used to evaluate this phenomenon. The results show that appreciable errors in the distance estimations can be expected especially on poorly tensioned distribution lines.

New techniques were also explored that are based on identification of the fault arc. Two methods were successfully tested on simulated networks to identify a breaking

conductor. The methods are based on the rate of increase in arc length during the breaking of the conductor. The first method uses arc voltage increase as the basis of the detection while the second method make use of the increase in the non-linearity of the network resistance to identify a breaking conductor. An unsuccessful attempt was made to identifying conductor clashing caused by high winds: it was found that too many parameters influence the separation speed of the two conductors. No unique characteristic could be found to identify the conductor clashing using the speed of conductor separation. The existing algorithm was also used to estimate the voltage in a distribution network during a fault for power quality monitoring purposes.

TABLE OF CONTENTS

TABLE OF FIGURES AND TABLES

DECLARATION OF ORIGINALITY

The work contain in this thesis has not yet been previously submitted for a degree or diploma at any other higher education institution. To the best of my knowledge and belief, the thesis contains no material previously published or written by another person except where due reference is made.

Karel Jansen van Rensburg,
January, 2003

ACKNOWLEDGMENTS

The author would like to acknowledge the advice and guidance of his supervisor Associate Professor David Birtwhistle throughout this research, and to thank the Head of the School of Electrical and Electronic Systems Engineering of the Queensland University of Technology for the use of School Facilities and financial support. Special acknowledgement is made towards Associate Professor David Birtwhistle for the fundamental ideas regarding the identification of breaking conductors, more accurate method in estimating a fault on radial distribution networks as well as estimating voltage dips using an existing fault locator algorithm.

Dr. A. Tam of the School of Manufacturing and Mechanical Engineering is thanked for his helpful comments and discussion on the mechanical aspects of a breaking conductor.

Finally the author would like to thank his mother – Connie Medlen – for editing parts of the script.

1. INTRODUCTION

1.1 Accuracy of fault locator algorithms

Distance protection on overhead lines has two important roles. The first usage is the estimation of the distance to fault for effective discrimination during the fault. The second requirement for distance estimation is for maintenance and speedy power restoration purposes. The down time of a line is dramatically reduced if the protection relay can provide accurate distance estimation.

Most common faults on overhead lines, such as insulator failures and lightning strikes, will include some kind of flashover. These arcs will cause a non-linearity in the network. However, almost all impedance type fault locator algorithms are derived with the assumption that the fault has a constant resistance. This non-linearity caused by the arc will therefore have some influence on most impedance type distance to fault locator algorithms.

Funabashi *et. al.* have done simulations to test the influence of arc faults on the accuracy of frequency domain fault locator algorithms [1]. The results show that arcing has a definite influence on the accuracy of this type of algorithm. Radojevic *et. al.* introduce a square wave arc voltage estimation into the standard differential equation algorithm to cater for these variations in the resistance due to arcing [2]. The simulations done by Radojevic *et. al.* shows that this algorithm produces stable and accurate distance to fault estimations under arc faults. However, no detailed study on the influence of arcing on the standard differential equation algorithm is available.

It is well known that conductors will cause opposing magnetic fields during a phase-to-phase fault. These magnetic fields will force the conductors away from each other and increase the average distance between the conductors. Impedance type relays use a pre-set per unit inductance value to estimate the distance to fault. The accuracy of the algorithm will therefore decrease if the inductance changes during the fault.

During the literature review it was discovered that no work has yet been done on this phenomenon. The only available model for this phenomenon is a rigid body model assuming the conductors act as a pendulum [3]. The authors have verified this rigid body model through experimental work. However the experimental work was only done for small conductor deviations and it is believed that the model will loose its accuracy for large deflections. A three dimensional finite analysis model base on simple wave equations was used to simulate the conductor deflection and to investigate the influence this deflection will have on the accuracy of any impedance type fault locator algorithm. The aim of this study will be to determine which line parameters influence the amplitude and speed of the conductor deflection. Certain case studies will also be presented to show what the influence of conductor deflection will be on the accuracy of the impedance type fault locator.

1.2 Monitoring of overhead lines using properties of arcs

The possibilities of using relays for more advance functions become possible with the rapid development of computational power of computers. The unique characteristics of an arc can provide information on specific conditions along the line.

The detection of high impedance faults on medium voltage systems is still a major concern for most utility companies. Li and Redfern [4] reported in 2001 that to date no secure method exists for detecting downed conductors. Most of the existing methods try to identify high impedance faults by looking for traces of arcs between the conductor and ground [4]. However, high impedance faults cause in some cases very small to no current to earth. This will make it virtually impossible to detect the downed conductor since no arcs will be present. This thesis will investigate the possibility of detecting a downed conductor during the actual breaking of the conductor. It will be assumed that an arc will be present once the conductor breaks. The dynamic characteristics of a breaking conductor in conjunction with the properties of an arc can be used to detect a breaking conductor. This thesis will make a proposal for detection of a breaking conductor on a radially fed distribution network.

Conductor clashing due to wind is an intermitted fault that is difficult to trace. These faults will only occur under specific wind conditions and utility companies will be unsure of the exact reason causing outages. If the utility company is aware of the exact reason for the outage, preventative maintenance can be performed e.g. re-tensioning of line. However, no method exists that will identify a clashing conductor fault. The same model used for conductor deflection estimations, but with different initial conditions, can also be used to investigate the dynamic properties of two clashing conductors under high, turbulent wind conditions. The aim of the simulations is to produce an algorithm that will identify clashing conductors.

Most of this thesis makes use of the proposed algorithm of Radojevic *et. al.* [2]. This algorithm is capable of estimating arc voltage during a fault condition. One of the natural developments is the use of this estimation in calculating the voltage level on a faulted distribution network for the purpose of power quality monitoring. Chapter 7 briefly investigate the accuracy of this estimation as well as estimating the voltage level on the rest of the faulted network.

1.3 Aims and objective

It is the aim of this thesis to: (i) conduct research into the influence of arc faults on the accuracy of differential equation algorithms, (ii) model and investigate the influence of conductor deflection during phase-to-phase faults on the accuracy of impedance type fault locator algorithms, (iii) investigate proposals to identify certain fault conditions based on the properties of an arc.

2 LITERATURE REVIEW

This literature review examines aspects of protection and fault location in overhead power lines that might possibly be influenced by arcing. The development of the distance to fault algorithms will be investigated. Special attention will be given to assumptions, problems encountered and solutions to the problems that were encountered. The second type of faults that includes arcing is a downed conductor. A brief description on existing techniques for detecting a broken conductor will be given. An arc model is required to simulate these faults on an overhead line distribution network. The various models will be investigated to determine the best model to suit a network simulation.

2.1 Background on Distance to fault locators

The most basic discrimination protection scheme is the standard Inverse Definite Minimum Time protection relay. This relay will trip the breaker nearest to the fault based on the time setting of the relay. This type of protection is slow if there are two or more series breakers. This leads to the use of a distance based discrimination relay or so-called Impedance type relays.

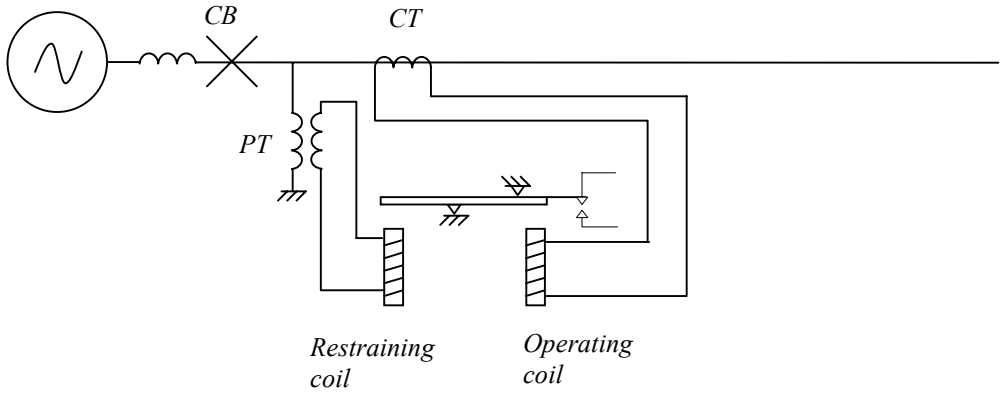

Figure 2.1: Electro-mechanical distance protection relay connected to line

Overhead lines are divided in pre-defined protection zones and the distance relays are set to trip if a fault is detected inside this zone. The original distance protection relays used the voltage and current signals from the instrument transformers to drive

a restraining coil and operating coil respectively. Figure 2.1 is a typical trip mechanism for an electro-mechanical distance protection relay. The relay will trip if the operating coil produces a larger force than the restraining force. High line current and low system voltage will typically cause a trip, which is caused by low load impedances. Modern digital relays used the current and voltage readings to calculate the impedance and thus the actual distance to fault.

Some of the advantages of using digital relays are [5]:

(a) The mechanical components make an electro-mechanical distance protection relay less accurate than a digital relay.
(b) The speed of operation of the relay can also be greatly improved, preventing unnecessary damage to equipment.
(c) A better-informed decision on auto re-closing can be made by the relay.
(d) Automatic detection of a faulty relay and removing itself from the network.
(e) Costs
(f) Integration of relay with the supervisory control and data acquisition system (SCADA) of the substation.

The advantages of digital relays are endless.

Digital relaying had its origin in the late 1960 and early 1970s with pioneering papers by Rockerfeller (1969), Mann and Marrion (1971), and Poncelet (1972). [5]. More than 1100 papers have been published since 1970 in this area of which nearly two thirds are devoted to the development and comparison of algorithms. However, the non-linearity of the arc resistance during faulted conditions has only been recognized recently by Radojevic [6] and Funabashi [1].

A detail description of all the distance to fault locator algorithms is beyond the scope of this thesis and only the main algorithms with some of the most important assumptions and variations will be discussed.

2.2 Frequency domain algorithms

2.2.1 Calculation of phasors

The frequency type algorithms convert the voltage and current signals into phasors (Amplitude and displacement angle). The most common and well-known method for these conversions is the Fourier transformation which includes complex and time-consuming calculations. Other mathematical techniques have been developed to avoid Fourier transformations in digital relaying. These techniques include:

(a) Fast Fourier Transformation
(b) Parameter Estimation
(c) Least Squares Fitting
(d) Discrete Fourier Transformation

Parameter estimation:
Parameter Estimation is a technique whereby N samples are used to solve a set of N equations with N variables [5]. The base frequency must be known for the calculation of the phasor. Any pure sinusoidal wave function with a fixed angle displacement can be represented by the summation of a sinusoidal- and co-sinusoidal function without any phase angle displacement. The amplitudes of the two trigonometric functions are the only unknown constants in such a function and they represent the phasor's real and imaginary components. Two equations can be obtained by sampling the signal twice (at two different time values). The phasor can be calculated by solving these two equations simultaneously. However, should this signal contain harmonics, two additional terms (co-sinusoidal- and sinusoidal function) must be added for each harmonic present in the signal. To represent M harmonics, 2xM unknown trigonometric function amplitudes will be present and 2xM equations are required to calculate the unknown phasors.

Least square fitting:
The method of least squares is a method for computing a curve in such a way that it minimizes the summation of the square of errors of the fit to a set of data points. This method for the calculation of the phasor is based on the same equations as discussed

in the previous paragraph. More samples are required than the actual unknown constants in the equation. The object of this method is to obtain values for the amplitudes of the trigonometric functions that will produce a minimum error which will reduce the influence of noise and harmonics that are not catered for in the original equation.

Discrete Fourier transformations:

The Discrete Fourier Transformation is derived from the standard Fourier Transformation. It can also be shown that it is a simplification of the Least Square Method. Let us assume that the matrix S consists of time dependant trigonometric values. By assuming a diagonal matrix for the function S^TS, it is possible to obtain the exact equation for the Discrete Fourier Transformation. Yang *et. al.* [5] proposed a Discrete Fourier Transform based algorithm to eliminate system noise and measurement errors. Results have shown that the method can extract exact phasors in the presence of frequency deviation and harmonics [5].

2.2.2 Evolution of Frequency based Distance to fault Algorithms

Digital fault locator algorithms are divided into two categories, one using data from one terminal of a single transmission line, and the other using data from both terminals. The former is superior from an economical viewpoint because it requires no data transfer over long distances. The latter is superior in the accuracy viewpoint of the fault location, but requires a data transfer system.

Funabashi classified the frequency domain fault locating algorithms [1] as follows:

(a) Impedance relay type method

(b) Current diversion ratio method

The impedance type locator algorithm assumes a bolted fault (zero fault resistance) and voltage drop per unit length of line is needed to locate the fault position. The current diversion algorithm is applicable to a loop-network. In the current diversion algorithm the assumption is made that the fault current is diverted between the faulted line and the healthy circuit and it is therefore possible to calculate the distance to fault if the assumption is made that the voltage drop per unit length is the same for both

lines. However, it seems that the development of fault locator algorithms in the frequency domain focused mainly on impedance type algorithms for transmission lines.

Transmission lines do not have branches, as is the case for distribution lines. It is also acceptable to assume constant fault resistances on transmission lines since arc voltages are relatively small in comparison with the system voltage. Figure 2.2 is a typical single line diagram that is most commonly used for the derivation of the different frequency domain algorithms. It shows a fault of resistance R_f , being fed from both the local supply (point of measurement) as well as the remote supply.

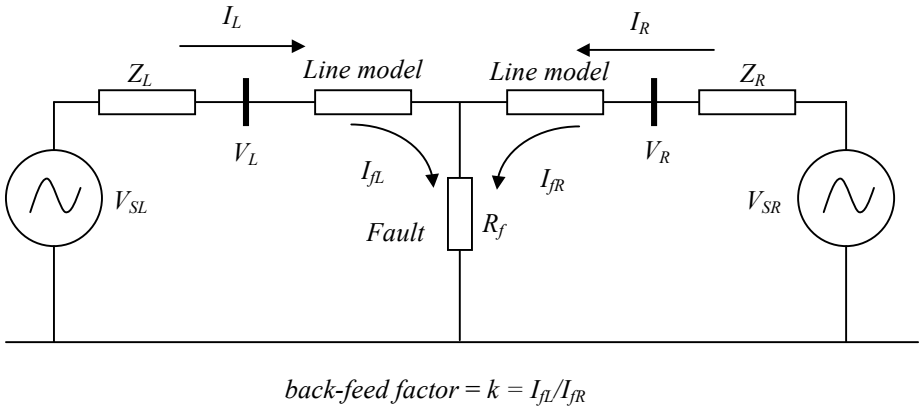

Figure 2.2: Single line diagram of a fault on a transmission line.

Since these original single-terminal algorithms were first presented, the algorithms have evolved into more sophisticated forms. The main objective of most of the new algorithms was to address one of the major problem areas. These problem areas can by summarised as follows:

(a) Need for fault resistance compensation.
(b) Unsymmetrical arrangement of the line
(c) Back feed from a remote source or other phases.
(d) Pre-fault load condition compensation.
(e) Mutual inductance of parallel lines
(f) Non-linearity of arcs.

Takagi [7] presented one of the first papers addressing inaccuracies in fault locator algorithms. The phenomenon of a fault in a single-phase circuit is solved using two equivalent circuits, one carrying a load current component and a second circuit carrying a fault current component in accordance with the principle of superposition. The algorithm is derived using a single line diagram based on Figure 2.2. The transmission line is modelled using a distributed parameter model. This model will therefore include line capacitance, which will influence distance estimations on very long transmission lines. Takagi show that this algorithm is described by Equation (2.1). A complete derivation of this algorithm is shown in [7].

$$\ell = \frac{\mathrm{Im}(V_s \bullet I_s'')}{\mathrm{Im}(zI_s \bullet I_s'')} \tag{2.1}$$

where

ℓ	Estimated distance to fault
V_s	Voltage at the measuring terminal
I_s''	Current difference between the pre-fault and after fault conditions
I_s	Current at the measuring terminal
z	Impedance per unit length

It is recognised that the algorithm will only be accurate for distance to fault less than 100km since Takagi [7], in the derivation of Equation (2.1), assumed that $\tanh(x\gamma) \approx x\gamma$ where x is the distance to fault and γ is the propagation constant of the line. For lines longer than 100km, Takagi shows that an approximation factor must be subtracted from the estimate distance to fault to increase the accuracy. The effect of the pre-fault load flow is cancelled by using the current component I_s''. This current is calculated by subtracting the pre-load current from the faulted current. The effect of the fault resistance is reduced by mathematical manipulation while deriving Equation (2.1). A further modification to Equation (2.1) included the effect of mutual inductance of conductors of the same or other parallel circuits. Takagi conducted a field test on a 71.2km long transmission line consisting of two parallel lines [7]. Nine faults were incepted over the test period that was mainly caused by heavy snow on the insulators. A maximum error in the distance to fault estimation of 2.6% was recorded during the test period.

Takagi [8] published a second paper, introducing the "current distribution factor" for transmission lines with sources on both ends (Figure 2.1). This factor is today more commonly known as the back-feed factor. The back-feed factor or "current distribution factor" is defined as the ratio of the fault current components flowing from the remote and local source respectively as shown by Figure 2.2. The purpose of the back-feed factor was to eliminate the effect of remote source back feed. This is done by estimating the remote current flowing into the fault as the product of the back-feed factor and measured fault current at the local point. Furthermore, Takagi demonstrated that this back-feed factor is a function of the position of the fault and that the back-feed factor should be a real value if it is assumed that the source and line impedance are inductive only. Using this, a non-linear equation is obtained and solved with the Newton-Rapson method.

Wiszniewski [9] developed an algorithm that can be used to determine the error in the distance to fault estimation due to fault resistance and remote sources feeding into the fault. He identified the error from impedance methods of fault location as a phase shift between the current measured at one end of the line and that through the fault resistance. The correcting equation has therefore been derived from the assumption that the equivalent circuit (including the fault resistance) is linear. Wiszniewski [9] also used the back-feed factor for his algorithm and showed the following interesting results pertaining to the current distribution factor:

(a) The back-feed factor is independent of the source voltages.

(b) The back-feed factor is a function of the network impedances

(c) The back-feed factor is almost totally a real value. The worst-case scenario would occur if the fault were at the remote end of the line. Wisniewski showed that in general, the back-feed factor's phase angle would not exceed 10° under such circumstances.

Wiszniewski also deducts the pre-fault current and voltage measurements from the measured values during the fault conditions to account for pre-load conditions. The correcting equation reduces the effect of the resistance on the line impedance, on the basis that the phase angle of the calculated impedance ought to be the same as the line impedance. This algorithm can be used in conjunction with any impedance type fault

locator algorithm that specifically calculates the impedance at the measuring point during the faulted condition.

A new algorithm for a distance to fault locator was presented by Eriksson, Saha and Rockefeller in 1985 [10]. This algorithm uses pre-fault and fault currents and voltages at the measurement point of the transmission line to determine the distance to fault. However, an estimated value for the source impedance is required, as this impedance determines the apparent fault impedance with novel compensation for fault resistance drop. This algorithm eliminates the errors caused by previous impedance type algorithms and reduces the complexity of the calculations by eliminating the zero-sequence currents in the algorithm. Further modifications to the algorithm were made to include the effect of mutual inductance of parallel lines.

Sachdev and Agarwal [11] in 1985, proposed to use an impedance type fault locator relay at the local measuring point. Information (voltage and current signals) from both the local and remote incomer/feeder is used to calculate the true fault impedances. A communication system connecting the local and remote points is required for this configuration. The algorithm was derived from an equivalent single-phase sequence component diagram for a single-phase to ground fault as shown by Figure 2.2. The authors stress that the voltage and current signals do not require to be synchronised. The algorithm also subtracts the line charging current after the first distance estimation to increase the accuracy on long lines. This procedure should, in theory, produce exact results. Simulations done by Sachdev and Agarwal [11] showed that the error in the distance estimation is as high as 8% for faults in the centre of a 115 mile, 500kV line with a fault resistance of 25Ω. A later paper by Sachdev and Agarwal [12] reported a smaller error in the centre of an identical simulated line. However, the source impedance of the remote supply was increased and thereby reducing the in-feed current.

Cook proposed two algorithms that also make use of data from both ends of the line [13]. These algorithms were derived from impedance phasors. As shown by Eriksson [10], an assumed value for the remote source impedance can be used to compensate for remote back feed current if no communication link exists. Cook's paper [13] presents results of accuracy test simulations. Although the results show

that the algorithm is highly accurate, the results could not be compared with those from the algorithm of Sachdev and Agarwal as different values of fault resistance were simulated.

The work of Ibe and Cory is based on a proposal by Kohlas more than 15 years earlier to use a distributed parameter line model for fault location [14]. Ibe and Cory use modal analysis to solve the partial differential equations of the distributed parameter line model to calculate the square of the voltage over the full length of the line. The effect of the fault on the voltage will be a minimum at the point of fault. For a bolted fault, the voltage would be 0V at the fault point and a V-shape graph of the voltage against line length is produced with the minima at the point of fault. This algorithm should produce results independent of the fault resistance, pre-load conditions or back feed current. The author has however indicated that some difficulties have been experienced with experimental tests i.e. no minimum in the voltage function exist if the point-of-wave of the fault is below 30°. It was also found that the magnitude and rate of rise of the wave travelling away from a fault fall, as the point-of-wave of the fault approaches a zero crossing. The author proposed the use of the second derivative of the voltage with reference to x (distance from measuring point), which proved to be successful.

Sachdev and Agarwal [12] criticised the methods of Takagi [7], Wiszniewski [9] and Eriksson's [10] algorithms. Sachdev argued that source impedances are not readily available and network configuration changes from time to time will modify the effective source impedances and therefore also the back-feed factor. An algorithm, using measurements at both ends of the transmission line, was again proposed. This, however, is not necessary for the synchronisation of the local and remote measurements. The algorithm is derived from the equivalent single-phase sequence component circuit for a single-phase to ground fault and was initially based on line models without any capacitance. To improve accuracy it is required that the algorithm is executed twice. After the first execution, the approximate total shunt capacitance for both ends of the fault can be calculated. The symmetrical components of the charging currents can be calculated by using the estimated capacitance values as well as the measured voltages at the line ends. It is shown that

this iterative process increases the accuracy by reducing the error on a 150km line to within 1%.

In 1991, Jeyasury and Rahman [15] compared the four most important single and two terminal algorithms (by Takagi (1982) [7], Wiszniewski (1983) [9], Ericksson (1985) [10] and Cook (1986) [13]) that had been developed since 1980. Surprisingly (i) Sachdev and Agarwal's [12] algorithm was not part of the evaluation, although it was recognised by Jeyasury and Rahman [15] and (ii) the oldest algorithm developed by Takagi (1982) [7] produced the most accurate results. The execution time of the algorithm was 370μs, only 50μs slower than Cook's double terminal algorithm. In a later paper [16] Jeyasury and Rahman acknowledge the work of Sachdev and Agrawal [12] although they suggested that inaccurate results are obtain for faults near the midpoint of the transmission line. This statement, however, is in contrast with the results published by Sachdev and Agrawal [12]. Sachdev and Argrawal showed by simulations that a maximum distance to fault estimation error of 2.5km (2.6%) for a 25Ω fault in the centre of a 150km transmission line could be expected [12]. Jeyasury and Rahman proposed their own two terminal algorithm which does not need synchronisation of the measured data of the local and remote measuring points. No simplifying assumptions were made during the derivation of the algorithm. It can therefore be assumed that the algorithm will be accurate although no accuracy tests were included in the paper [16]. The main difference between this algorithm and the one proposed by Sachdev and Agrawal, is that Jeyasury and Rahman did not make use of the sequence component circuits.

Waiker, Elangovan and Liew [17] developed a set of 12 equations to be used in the analysis of the 10 possible faults that may occur on an overhead line. This work was based on an algorithm produced by Phadke, Hlibka and Ibrahim in 1977 [18]. The algorithm was developed for single terminal protection and makes provision for a constant resistance fault. It allowed for pre-fault conditions by subtracting the pre-fault load conditions from the current during the fault condition. The error due to the arc resistance is still only an estimation since the exact faulted current, I_f, is a function of the fault resistance and load. Both of these two quantities are unknown during the fault. Three constants are defined that are dependant on the fault type with the following values; a^0, a^1 or a^2 ($a=1\angle 120°$). The method has computational

advantages over the previous methods that used symmetrical components. Waiker, Elangovan and Liew made a comparative study of the computational load of his own algorithm with that developed by Phadke in 1979 [19]. It was concluded the time to execute Waiker's algorithm would be at least six times faster than the original algorithm proposed by Phadke.

Johns, Moore and Whittard [20] presented a more accurate algorithm for single-end fault locators in 1995 introducing a totally new concept in the development of this algorithm. This algorithm is based on the assumption that the impedance is real at the point of fault. By using the phase difference between the voltage and current as well as the line impedance, it is possible to calculate the position where the voltage and current are in phase. The same two assumptions, as made by Eriksson *et. al.* [10] and Cook [13] in the mid eighties were employed to develop the algorithm. These assumptions were; (i) the remote source impedance is known and (ii) the fault current is equal to the difference between the line current under faulted conditions and the pre-fault current. Johns *et. al.* [20] however explore the influence of changes in the remote source impedance. It was concluded that for small fault resistances ($R_f < 5\Omega$) the influence of ±30% change in source impedance would produce an error in accuracy of less than 1%.

In 1998 Liao and Elengovan [21] transformed the algorithm developed by Waikar *et. al.* [17] into a two terminal fault locator algorithm. The algorithm was reduced in complexity and the terms with the assumed remote source impedance could be replaced by real time data. The number of required constants was dependent on the type of fault, and was increased to five. The computation time of this new algorithm was reduced by a third compared with the original algorithm first proposed by Waiker *et. al.* [17].

Saha, Wikstrom and Rosolowski [22] developed an algorithm that specifically reduces the effect of parallel lines. This work follows on earlier work done by Liao and Elengovan [21] as well as Zhang. This algorithm however compensates for shunt capacitance in much the same way as first proposed by Sachdev and Agarwal [12]. Saha *et. al.* [22] showed with simulations that the compensation for line capacitance

reduce the maximum distance to fault error on a 300km line from 2% to less than 0.3%.

2.2.3 Conclusion

The frequency domain impedance type relay algorithms were first developed in 1972 and were based on the assumption of zero fault resistance. The first problem that was identified in the early algorithms was the influence of pre-load conditions on the accuracy of the fault locator. Subtracting the pre-fault current from the actual fault current to calculate the true fault current solved this problem. The second obstacle was the influence of the fault resistance. Two methods were developed:

(i) The first method that is the cheapest and most reliable solution in terms of maintenance, assumed a value for the remote source impedance and required voltage and current measurements at a single point. This method is however not ideal since system changes can cause errors in the accuracy.

(ii) Johns [20] developed an algorithm that was unaffected by small changes in the remote source impedance and small fault resistances. Sachdev and Agarwal [12] proposed the use of remote measurements to compensate for back feed. This method has been researched and developed extensively for the past 15 years.

The influence of shunt capacitance on long lines was first addressed by Sachdev and Agarwal [12]. The distance to fault is first calculated without any capacitance. After the first estimations of the distance and shunt capacitance, the capacitance currents are calculated and subtracted from the measured currents and the distance to fault are re-calculated. In recent years, more attention is given to the influences of parallel lines on the accuracy of the algorithms.

Wiszniewski [9] identified one of the unresolved problems in 1983. He indicated that these algorithms are only valid for linear systems. All algorithms used in the frequency domain, were developed from models with constant fault resistance. Since arcs cause non-linear fault resistance, this will most definitely influence the accuracy of the algorithms. One of the earliest experimental studies carried out on this subject was that by Warrington, who investigated the effect arcing faults would have on system protection. Funabashi *et. al.* [1] did a sensitivity study on Takagi's algorithm and determined the influence of the non-linearity of the arc on the accuracy of the

algorithm. It was shown that an increase in the degree of non-linearity of the arc, increases the location error.

2.3 Time domain algorithms

Much less literature is available on time domain fault locator algorithms. Time domain algorithms make use of differential equations for a transmission line and use a standard RL circuit as model (Figure 2.3) for an overhead line. The basic circuit equation is given by Equation (2.2).

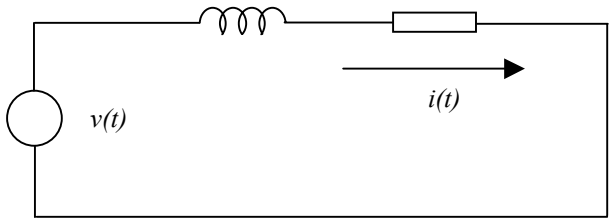

Figure 2.3: Series L-R circuit used as equivalent circuit to derive differential equation fault locator algorithms.

$$v(t) = L\frac{di(t)}{dt} + i(t)R \tag{2.2}$$

In Equation (2.2) *v(t)*, *i(t)*, *L*, *R* represents the voltage, current, inductance and resistance respectively. The resistance, *R*, includes both the line and fault resistance. It is further assumed that the fault impedance is resistive only. The inductance, L, represents the total line reactance. The resistance and inductance is calculated by the integration of Equation (2.2) between two successive sampling points [5]. A problem in the accuracy exists should the current and its derivative be small. This would typically occur due to DC offsets. Median filters are used as a solution to this problem as well as to increase the soundness of the output [23].

Akke and Thorp [23] showed that isolated estimates from a differential equation could be very poor. A comparison was made between a post-filtering system (with a

4ms time constant) and a median filter. Equation (2.3) defines a median filter of order N, where x_i is the individual estimates and x_{eff} is the effective output of the filter.

$$x_{eff} = \left[\prod_{i=1}^{N} x_i \right]^{1/N} \tag{2.3}$$

Akke and Thorpe used a standard pi-circuit model with a 10mΩ fault resistance for simulation purposes in MATLAB. The results indicate that a 17th order median filter should at least be used. This median filter decreases the response time of the algorithm. It will need at least 17 samples to converge to the correct output.

The generalized equation error (GEE) approach is a second method for improving the soundness of individual estimates. The most resent literature available on this method was presented by Segui et. al. in 2001 [24] although a paper on this method was first presented in 1982 by Bornard and Bastide [25]. Segui *et. al.* classified the different differential equation algorithms and she also generalised the GEE and divide it into two steps:

(a) Transformation of the differential equation into a sampled or discrete equation. This can be either the standard differential equation or the numerical integration of the differential equation.

(b) The use of parametric resolution techniques for individual estimates or equations. Examples of the more well-known and practical techniques are the Kalman filter, Forgetting factor, least square and recursive least square methods [24].

The result of the first step (a) of the GEE approach shown above is a matrix equation, describing the error for each individual sample point as a function of the line parameters and sampled data. The second GEE step (b) will estimate the parameters to obtain a minimum error. Segui [24] made simulations, using constant fault resistance, to show the effect of the parametric resolution techniques under specific conditions such as transients and harmonics. The disadvantage of these methods is high computational loads on the relay microprocessors due to complex matrix calculations.

The differential equation algorithms are affected by the same problems that are present in the frequency domain fault locator algorithms. This includes back feed due to non-zero fault impedances. The standard differential algorithm uses a constant back-feed coefficient (as defined by Takagi *et. al.* [8]) for the estimation of the back-feed current. Fikri [26] argued that this assumption will only be valid after the transients have past. In order to improve the speed of the algorithm, Fikri proposed an algorithm to estimate the back-feed current. In the derivation of this equation, it was assumed that the network impedances are fixed and equal to those obtained from the most recent pre-fault estimation. Fikri stress that in practice, the effective generator impedance changes rapidly from synchronous to subtransient values after fault inception. It was shown that the distance to fault predicted by locators converges within 5ms, and a trip signal is given within 10ms. The effect of capacitance was addressed in much the same way as in the algorithms produced by Sachdev and Agarwal [12]. This algorithm was, however, only tested on constant fault resistances.

The non-linearity of arcing in faults was for the first time introduced in the fault locator algorithm by Radojevic, Terzija and Djurie [6]. A third term was introduced to Equation (2.2) that estimates the arc voltage as a square wave. This assumption and parameter estimations of Radojevic was based on earlier work done on arcing by Terzija and Koglin [27-29]. Terzija indicated that an arc can be estimated as a square wave and introduced the least square method for obtaining arc voltage amplitude. It was proposed that a decision on automatic re-closing should be based on the amplitude of the calculated arc voltage. Temporary faults are normally flash-over faults between two phases or across an insulator. These faults would be cleared after the arc is extinguished. These types of faults consist of a long arc with large arc voltage amplitudes. The estimated arc voltage amplitude can therefore be used to identify these temporary faults.

Radojevic derived Equation (2.4) from the equivalent single-phase sequence component circuit for a single phase to ground fault on a three phase system based on the assumption that the arc voltage can be estimated to be a square wave.

$$u_k = \left\{ r i_{k+} \frac{x}{2T\omega_0} \left[i_{k+1} - i_{k-1} + K_L \left(i_{0(k+1)} - i_{0(k-1)} \right) \right] \right\} \ell + \operatorname{sgn}(i_{0k}) U_a + i_{0k} R_e + \varepsilon_k \qquad (2.4)$$

In Equation (2.4) $K_L=(x_0-x)/x$ is a function of the line inductance, x_0 is line per unit length zero sequence inductance, x is the line per unit length positive sequence inductance, $R_e=(r_0-r)\ell+k_aR_F$ is an equivalent resistance, r_0 is line per unit length zero sequence resistance, ω_0 is the fundamental angular velocity and ε_k is the error modelling all measuring errors, model errors and random variances of the arc. The back-feed constant $k_a= i_F/i_0$ is assumed to be constant although Fikri rejected this under transient conditions. It should therefore be expected that this algorithm would be slower to converge than Fikri's algorithm with the back-feed current estimation equation. No value for this back-feed coefficient is required and is part of the constant value R_e that will be automatically calculated.

Radojevic's algorithm uses the least square method as the parametric resolution technique. By defining a data window, containing N samples, N-1 equation can be created with 3 unknown values. Using the Least Square Method, the best-fit values for the distance to fault, arc voltage amplitude and equivalent resistance is calculated. Radojevic used typical values of 100 samples with a sampling rate of 5kHz. This will define a data window of 20ms. The main disadvantage of the algorithm is that it assumed constant arc voltage amplitude for the duration of the data window. The error in the accuracy would increase should a variance in the arc voltage be present. Radojevic recognise this, and proposed that the data window should be shortened. The ideal response would be if the data window were only 3 samples long, creating two equations, while the arc voltage is assumed to be zero. Simulations done by Radojevic *et. al.* [6] for such a short data window shows a highly unstable distance to fault estimation with singularities present around the current zero period.

These singularities are due to the rapid increase in the arc resistance during low fault currents. Although Firki [26] never tested his algorithm on an arc fault, these same singularities will most probably be present in his algorithm. The algorithm uses the assumption that the line parameters (including the arc resistance) are constant over two samples. However, the arc resistance is relatively high and it is changing rapidly at low currents. The algorithm presented by Radojevic is the first algorithm that

caters for non-linearity in the fault resistance. Although the general accuracy of the algorithm is high, unacceptablely high errors occur due to back-feed should a high resistive fault occur near the end of the line. With respect to back-feed errors, it seems that Firki's algorithm is still superior to Radojevic's algorithm. The main difference between these two algorithms is that Radojevic assumes a pure real back-feed factor while Fikri uses a two terminal approach with real time impedance estimation of the remote source.

2.4 High Impedance Fault Locators

High impedance faults (HIF's) are in general difficult to detect by conventional protection equipment such as distance or over current relays. The main problem in detecting energized conductors that have fallen to the ground is that the resulting fault current may be insignificant and hence difficult to detect by conventional relays. Table 2.1 provides typical current levels for different surface materials [30, 31]. Downed conductors on dry asphalt, sand or gravel may not be detected, since these surfaces may not produce an arc or fault current. Most medium voltage distribution networks are in highly populated urban areas. The downed energised conductor therefore represents an immediate safety hazard for the general public.

This is not a new problem and Redfern reported that in 1949 an AIEE committee concluded that there was at that time no successful solution to the problem. An endless amount of methods and algorithms have been produced over the last twenty years. However, should a relay be sensitive enough to trip on most high impedance faults, one can expect unwanted nuisance trips. A short summary of the most prominent algorithms are discussed in the following paragraphs:

Table 2.1: Typical current levels for different surface materials for a system voltage of 11kV

Surface	*Condition*	*Current*[30]	*Current*[31]
Sand	Wet		26A
	Dry	0A	9A
Asphalt	Wet		37mA
	Dry	0A	96mA
Lawn	Wet	50A	57A
Gravel	Wet		31A
	Dry		115mA
Concrete	Wet		63A
	Dry	75A	32A
Soil	Wet		46A
	Dry		11A
Tree	Wet		4.89A
	Dry		23A

Proportional Relaying Algorithm [32]

The variable fault and zero sequence currents seriously affect the ground over current relay's sensitivity. This algorithm calculates the fault current, by using the zero sequence current and line neutral current. The calculated fault current phase angle and amplitude is more constant. This increases the over current earth fault relay's sensitivity. Stage tests done by Huang *et. al.* indicate an identification rate of 77% and can only detect currents above 15A [33].

Ratio Ground Relay Algorithm:[34]

This type of relay was design to detect open circuit conductors. It was developed to overcome the effect of load variations. The amplitude of the zero sequence current is compared with the difference between the amplitude of the positive and negative sequence currents. This method is more sensitive than evaluating the zero sequence current alone. Huang concluded that the algorithm has a 100% identification ratio [33]. The commercial relay using the same algorithm has however identified only 77% of the faults.

Third Order Harmonic Current Relaying Algorithm

Hughes Aircraft Company developed an algorithm that compares the third order harmonic current's amplitude and phase angle with the fundamental current's amplitude and phase angle. Huang concluded that the relay's identification rate was 77% with a minimum required fault current of at least 15A [33]. Haung also made

the following comment on this type of relay after testing the algorithms: “All of the characteristics for the ratio of the harmonic current to the fundamental current relaying algorithms are worse than those of the harmonic current amplitude relaying algorithms. Therefore, they can be abandoned”. The Nordon High Impedance Fault Analysis System [35] algorithm responds to a change in the 3rd harmonic current on the distribution network. Data on the harmonics of the existing system is required for the correct setting of the relay. Atwell *et. al.* [35] showed with tests that currents as small as 3% of the CT’s nominal current were successfully detected. The installation and commissioning of this relay poses a problem as existing harmonic levels can easily influence the relay. Atwell was however confident that the commissioning of this type of relay would become easier as more knowledge is gained about this type of relay.

Energy Algorithm [36]

The energy algorithm monitors the level of energy contained in a specific range of frequency components. The energies are summed over the full fundamental frequency period. The non-harmonic energies are used as indicators for arc identification. A significant rise in the non-harmonic energies would indicate a high impedance fault. Aucion conducted staged fault tests with a prototype relay [37]. The relay was using an energy algorithm to detect arcing faults. The tests indicate that the relay required at least 20-50A to operate.

Voltage Unbalance

The Kearny Manufacturing Company Open Conductor Detection system detects the loss of voltage at each end of a line. Should a fault occur, a signal is sent to the circuit breaker to isolate the feeder. This system was developed and tested in 1992 [4]. Senger *et. al.*[38] made some improvements to this system by adding extra sensors along the line. These extra sensors will give an idea of the location of the downed conductor. The sensors furthermore use magnetic fields to detect a phase loss. No contact exists between the sensor and the power network. A communication network is however required to transmit the information back to the feeder isolator/circuit breaker.

Randomness Algorithms [39]

This algorithm is an extension of the Energy Algorithm. The Randomness Algorithm accommodates the large variations of the arc between two cycles. The energy is monitored at a specific frequency and bandwidth (2-3.6kHz). A fault is registered if the energy varies according to two specific criteria between 30 consecutive cycles. The tests done by Benner *et. al.* indicated that the algorithm failed only once to operate. It was also stated that no false detections was made during the testing period. Benner however did not indicate what the minimum required fault current for operation was.

Digital and Signal Processing

A wide variety of techniques exists that will identify the waveforms associated with high impedance, downed conductor faults. These methods include using the crest factor [40], wavelets [41], Kalman filtering [42], transient recognising, advanced neural network processes and half cycle asymmetries and current flickering [43]. What is important to recognise is that all of these algorithms is designed to identify the high impedance arcing phenomena on a line. The biggest problem presented by these methods is the necessity for arcing. No detection is possible if the downed conductor is lying on highly insulated material like Asphalt.

Secure fault detection

Aucion and Jones suggested that, since no single algorithm is available, a multiple set of algorithms should be used in parallel [44]. The algorithm must check simultaneously for arcing, load loss and over current conditions. Both arcing and load loss should be detected before the feeder is tripped on a high impedance fault. Researchers at Texas A&M University developed a relay for General Electric Company using four simultaneous algorithms [45]. The faults are categorised in three classes, requiring at least two of the four algorithms to activate the relay.

The philosophy of al the existing algorithms is based on the detection of an arc. The relays would fail to operate if no arc is produced. In 2001 Redfern's report [4] concluded: "…downed conductor detection still represents one of the major challenges facing the electricity power supply industry. Considerable work has

already been invested in finding a viable solution however the perfect answer still remains to be found."

2.5 Free Burning Arc Modelling in Power Networks

Arcing is a common phenomenon during fault conditions on overhead lines. It is expected that the arc will cause inaccuracies in fault locator algorithms due to non-linearity in the arc. This was shown by Funabashi [1]. It is therefore important that the properties of the arc are fully understood for any future development of fault locators. The possibility also arises in the development of new techniques, identifying certain conditions on the power line, thereby helping with the maintenance of the installation. In this section, an overview of arc models will be investigated with the aim at using the most suitable model for simulation purposes.

Arc models are classified by van der Sluis [46] in three categories:

(a) Physical models
(b) Black box models
(c) Parameter models

Physical arc models are based on the actual physical process of the arc. These models use the principals of fluid dynamics, thermodynamics and Maxwell's equations. These physical models are normally used in the development of circuit breakers. These physical models assume a straight, cylindrical arc with a uniform radius. Examples of such models can be found in physics tertiary publications [46, 47]. Rutgers, Koreman and van der Sluis introduce a new physical model, describing the conductance after current zero [48]. This model calculates the conductance by modelling the dynamic behaviour of the charge carriers after current extinction. This method is used to determine if a re-strike is possible or not during a simulation.

In black box models, the arc is described by simple mathematical equations. These equations give the relation between the arc conductance and measurable parameters such as arc voltage and current. Typical well-known black box models are the Cassie model [49] and the Myar model [50]. The equations describing these two models are a solution to the general arc equation of the physical models. The Cassie model

assumed that the arc channel is cylindrical with a constant temperature but variable diameter. Since the temperature and therefore the conductance are of constant value, the radius must reduce if the energy inserted into the system is reduced. The Cassie model is suited for modelling of an arc in the high current regions, when the plasma temperature is 8000K or more [46]. The Mayr model describes the arc conductance around current zero. This model assumed a cylindrical arc channel with a constant diameter. The arc column loses its energy by radial heat transport, and the temperature varies accordingly. Browne [51] proposed a combination of the two models, using the Cassie equation during high current conditions and the Mayr model for the current zero periods.

A number of studies were done to determine experimentally the characteristics of long, free burning arcs. Table 2.2 summarise the results of a few of the most important works. These empirical equations were obtained from experimental results and may be used to calculate the stationary arc conductance. In Goda, Johns and Duric's models, the voltages tend to be constant, independent of current, at high currents. The equations of Cornick and Stokes, indicates the voltage is still dependant on current at high current arcs. Maecker have predicted this phenomenon [47]. Stokes has done a comparison between his experimental data and a physical model. He concluded that the theoretical studies of Maecker confirm his experimental work.

Most studies [1, 53, 55] use the Mayr model, as described by Equation (2.5), to calculate the time dependency of the conductance of the arc. The time constant τ is an indication on the rate of heating of the arc gap. Typical values that was assumed for long, free burning arcs, were 0.625ms [52] and 0.4ms [55]. Johns however indicated that the time constant τ is a variable and should be dependant on the arc length and peak current [29]. The time constant τ, arc length z_g and peak current I_p relationship was derived from experimental data and is given by Equation (2.7).

Table 2.2: Summary of most important equation for steady state arc voltage calculations

Ref	Author	Date	Basic Empiric Equation
[52]	Cornick	1981	$i_a(t) = K_1 u_a(t) + K_2 (u_a(t))^7$ where K_1 and K_2 is derived from the piecewise linear graphs obtained experimentally by Stom.
[53]	Johns Al-Rawi	1984	$u_a(t) = 75 z_g I_0^{-0.4}$ where I_0 is defined as the peak current and $I_0 \in (1,55)$ Ampere
[54]	Stokes Oppenlander	1991	$u_a(t) = (20 + 0.5 z_g) \cdot (i_b(t))^{-0.88}$ where $i_b(t) = \begin{cases} I_0 & \lvert i_a(t)\rvert < I_0 \\ \lvert i_a(t)\rvert & \lvert i_a(t)\rvert \geq I_0 \end{cases}$ $I_0 = 10 + 0.2 z_g$
[27]	Djuric Terzija	1995	$u_a = \left(U_e + U_b \frac{I_0}{i_b(t)} + R_\delta \lvert i_b(t)\rvert \right) sign(i_a)$ where $i_b(t) = \begin{cases} I_0 & \lvert i_a(t)\rvert < I_0 \\ \lvert i_a(t)\rvert & \lvert i_a(t)\rvert \geq I_0 \end{cases}$
[55]	Goda et. al.	2000	$u_a(t) = z_g \left(0.95 + 0.005 (i_b(t))^{-1}\right)$ for high current, long air gap arcs only.

$$\frac{dg}{dt} = \frac{1}{\tau}(G - g) \tag{2.5}$$

$$R = \frac{1}{g} \tag{2.6}$$

$$\tau = \frac{\alpha I_p}{z_g} \tag{2.7}$$

In Equation (2.5), G is the static conductance of the arc, g is the time variable conductance while α in Equation (2.7) is a constant that is dependant on the current classification. Johns used a value of α=2.85×10^{-5} for heavy current arcs (50kA

region). The value of the peak current, I_p, is calculated by assuming bolted fault conditions. If Equation (2.7) is used to calculate the time constant with an assumed fault current of 2000A and arc length of 100cm, a value of 0.56ms is obtained. This results correlate with the fixed values as used by Funabashi and Goda.

It is concluded that the following conditions would be the best method to simulate an arc on the network:

(a) Calculate the static arc conductance by using the empirical equations of Stokes [54];

(b) Use Mayr's Equation (2.5) and Equation (2.7) to calculate the time varying resistance of the arc [1, 53, 55];

(c) Use an time constant of 0.5ms.

2.6 Summary

The literature review shows that most of the work done on overhead line faults concentrates on frequency domain algorithms while less attention were paid to time domain algorithms. Research is focused on the accuracy of the algorithms with special attention being paid to inaccuracies caused by back feed from a remote source. One paper investigates the influence of arcing on the accuracy of frequency domain algorithms while no work to date have investigates the influence of arcing on time domain differential equation algorithms. There is therefore a definite need in determining the effect of arcing on the accuracy of the time domain fault locator algorithm. Conductors under phase-to-phase fault conditions will deflect under magnetic forces and cause a change in the total inductance of the line. This change in the inductance will influence the accuracy of impedance type fault locator algorithms. The parameters that will influence the accuracy as well as the magnitude of the influence are unknown since no investigation to date has covered this phenomenon.

A differential type fault locator algorithm was recently introduced that assumes the arc voltage to be square-wave like. This method can be used to estimates the arc voltage during a fault. The arc voltage holds some information regarding the properties of the fault. There therefore exists a possibility of developing a more

intelligent relay using the properties of the fault arc to identify the type of fault at a remote point on the line.

3 INFLUENCES OF ARCING ON DIFFERENTIAL EQUATION TYPE FAULT LOCATOR ALGORITHMS

Differential equation type algorithms form the mainstream time domain fault locator algorithms. Funabashi *et. al.* showed that arcing causes inaccuracies in frequency domain algorithms [1]. Radojevic *et. al* have modified the standard time domain differential equation algorithm to accommodate arcing on the network [2]. Segui published a comprehensive study on differential Equation algorithms [24]. This includes the different parametric estimation techniques and the influence of capacitance on the different algorithms. However, no comparative testing has yet been done to test the influence of an arc on the accuracy of differential equation algorithms. The aim of this section will be to investigate the influence of arcing on the accuracy of the differential equation algorithm. The effectiveness of the square wave approximation of the arc voltage by Radojevic *et. al.* will also be compared with the standard differential Equation type algorithm.

A new type of differential equation algorithm is presented in this section and will be used to investigate the influence of arcing on time domain impedance type algorithms. This algorithm is based on the convolution operator and can be defined as the fourth type differential Equation algorithm [24]. This equation will be used to determine the effect of arcing on standard differential equation algorithms. The algorithm was originally tested under constant fault resistance conditions to determine the effectiveness of the algorithm. Simulations are conducted on single-phase circuits with a standard pi-circuit as well as a distributed parameter line model. These simulations showed that the algorithms compare well with the existing algorithms. One of the newly proposed algorithms was also transformed into a three-phase fault locator algorithm using an equivalent sequence component single-phase circuit for unsymmetrical faults. The algorithm for three-phase systems performed better under constant resistance faults in comparison to the single-phase algorithm.

A line-to-ground arc fault is introduced onto a 20km long line to determine the influence of the arc on the differential type algorithm. It is shown that an arc will cause large instability on the output of the standard differential equation type fault

locator algorithm. The algorithm of Radojevic *et. al.* was also tested with simulated arc fault. The results show that this algorithm's output is more stable than the standard differential type algorithm.

3.1 Differential Equation algorithm on a single phase circuit

Figure 2.3 is a typical circuit used to derive the standard differential equation algorithms for single-phase circuits. All differential equation type fault locator algorithms are derived from a standard differential circuit Equation (2.2) using differential linear dynamic operators, integral dynamic operators or filter linear dynamic operators [24]. A fourth technique is proposed using the convolution operator. Equation (2.2) can be written in the Laplace domain as Equation (3.1). Equation (3.2) is obtained by the inverse Laplace transformation of Equation (3.1).

$$i(s) = \frac{v(s)}{R + sL} = \left(\frac{1}{L}\right)\left(\frac{1}{R/L + s}\right)v(s) \tag{3.1}$$

$$i(t) = \left(\frac{1}{L}e^{-\frac{t}{L/R}}\right) \otimes v(t) \tag{3.2}$$

3.1.1 Estimating the voltage signal as an array of impulse functions

A numerical approximation of the voltage signal is needed to simplify Equation (3.2). The voltage signal can be estimated as a series of pulses with a time spacing of Δt and area equal to the sampled voltage amplitude. Equation (3.3) is the solution to the convolution operation of the impulse estimated voltage function and the transfer (impedance) function in the time domain. The complete mathematical derivation of Equation (3.3) is shown in Appendix I.

$$i_{k+1} = i_k e^{-\frac{\Delta t}{L/R}} + \frac{1}{L}\Delta t v_k \tag{3.3}$$

The total inductance from the point of measurement will give an indication of the distance to fault. Both the inductance L and resistance R in Equation (3.3) are unknown values while the voltage and current are known (measured). Two independent equations are necessary to calculate the total inductance from the point of measurement to the fault position. These two equations are based on Equation (3.3), and are obtained from three consecutive current and voltage samples. Equation (3.4) is obtained by the simultaneous solution of these two independent equations. This equation can be used to estimate the distance to fault and is the fourth type of differential equation fault locator algorithm derived from the convolution operator. A more complete mathematical derivation of Equation (3.4) is shown in Appendix I.

$$\ell = \frac{\Delta t}{L}\left[\left(\frac{v_{k-1}i_k - v_k i_{k-1}}{i_k i_k - i_{k-1}i_{k+1}}\right)\right] \tag{3.4}$$

In Equation (3.4) the variable ℓ represents the distance to fault. Note that L here represents the inductance of the line per unit length and not the total inductance as used in the previous equations. The accuracy of this algorithm will be highly dependent on the correctness of approximating the voltage signal as an array of impulses. This algorithm can also be derived from a more commonly known differential equation.

Equation (3.5) is a standard differential equation describing the circuit in Figure 2.3. This equation can be re-written in the form indicated by Equation (3.6). Equation (3.6) and Equation (3.3) is identical for all small values of $\Delta t \cdot (R/L)$. Equation (3.6) is the first two terms of the Taylor expansion of Equation (3.3). However, the simultaneous solution of the distance to fault obtained from two independent equations for three consecutive samples will be identical to that of Equation (3.4). Equation (3.4) is therefore also the distance to fault locator algorithm derived from the differential Equation (3.5). The difference between these two methods will only become evident when transforming the algorithm to cater for three phase circuits (Section 3.2).

$$v_k = L\frac{\left(i_{k+1} - i_k\right)}{\Delta t} + i_k R \tag{3.5}$$

$$i_{k+1} = \left(1 - \frac{R}{L}\Delta t\right) i_k + \frac{1}{L}\Delta t \cdot v_k \tag{3.6}$$

3.1.2 Estimating the voltage signal as a linear function

The previous section shows that it is possible to derive a fault locator algorithm from Equation (3.2) by simplifying the voltage signal as an array of impulse functions. A second method of simplifying Equation (3.2) is by estimating the voltage signal as a linear function ($m_v t+v_0$) between two consecutive samples. Equation (3.2) can be simplified to Equation (3.7) by applying the convolution operator on the transfer function and linear estimated voltage signal. The voltage gradient m_v is calculated by subtracting two consecutive voltage samples divided by the sample period. The time constant τ and total line inductance L in Equation (3.7) are unknown variables. Two independent equations are again required to calculate the unknown time constant τ and inductance L. Equation (3.8) is the solution of the two simultaneous Equations and is a more complex solution than Equation (3.4) since the time constant τ (= L/R) has to be solved numerically.

$$i_{k+1} = \left(\frac{1}{L}\right)\left(m_v \Delta t \tau + \left(v_k \tau - m_v \tau^2\right)\left(1 - e^{-\frac{\Delta t}{\tau}}\right)\right) + i_k e^{-\frac{\Delta t}{\tau}} \tag{3.7}$$

$$\left(i_{k+1} - i_k e^{-\frac{\Delta t}{\tau}}\right)\left(m_{v_{k+1}} \Delta t + \left(v_{k+1} - m_{v_{k+1}} \tau\right)\left(1 - e^{-\frac{\Delta t}{\tau}}\right)\right)$$

$$-\left(i_{k+2} - i_{k+1} e^{-\frac{\Delta t}{\tau}}\right)\left(m_{v_k} \Delta t + \left(v_k - m_{v_k} \tau\right)\left(1 - e^{-\frac{\Delta t}{\tau}}\right)\right) = 0 \tag{3.8}$$

The distance to fault ℓ is calculated by solving for time constant (τ) numerically with Equation (3.8). Equation (3.7) is then used to estimate the total inductance or distance to fault. The estimation done in this algorithm should be more accurate than the algorithm obtained from the impulse like voltage estimation. The voltage signal was estimated by a piecewise linear voltage signal between two consecutive voltage samples instead of an array of pulses. A complete derivation of Equation (3.7) and (3.8) is shown in Appendix I. It must be noted that Equation (3.8) is a rather

impractical equation due to its complexity and will only be used as a control for the evaluation of the less complex Equation (3.4) in the single phase simulation tests.

3.1.3 Accuracy of the algorithms under constant fault resistances

The main concern about the accuracy of these newly proposed algorithms is the correctness of the voltage estimations. The accuracy of the algorithms will be tested for a simple single-phase to ground fault condition with a constant fault resistance. The simulations will be done for various fault resistances to determine the influence of the fault resistance on the accuracy of the algorithms.

The main concerns for testing the algorithms for various fault resistances are obtained from inspection of Equation (3.3). A large resistance will cause a small time constant and the first term on the right hand side may become negligibly small. In such circumstances it is expected that the current will be a pure function of voltage and inductance. This is however not right since the current should be determined by the system voltage and resistance for larger resistance values. The fault resistance can therefore play a major role in the accuracy of the algorithm.

The circuit in Figure 3.1 is used to determine the effect of the system resistances on the accuracy of the algorithms. The circuit represents a supply with source impedance, pi-modelled line and constant resistance fault. The voltage and current waveforms were calculated by using standard differential circuit equations in MATLAB. The distance to fault ℓ was set to 15km with a time step of 20μs. The algorithms were also evaluated in MATLAB. The standard sampling period in this work were assumed to be 5kHz based on the same sampling frequency used as an example by Radojevic *et. al.* [2] in testing their proposed differential equation algorithm.

The error is defined as the standard deviations of the last 20ms as a percentage of the true distance to fault, which is used as the mean value in the standard equation to calculate the standard deviation. A second set of data was also obtained by doubling

the line inductance as shown in Figure 3.1 to determine the influence of inductance on the accuracy of the algorithms.

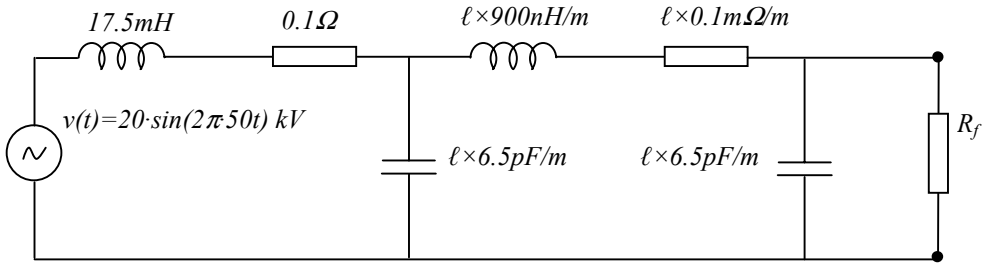

Figure 3.1: Circuit used to derive the circuit equations with a distance to fault of 15km

A third existing differential equation algorithm was used as a control algorithm. This is an integral dynamic operator type differential equation algorithm that was used by Kudo *et. al.* for implementation in a commercial relay [56].

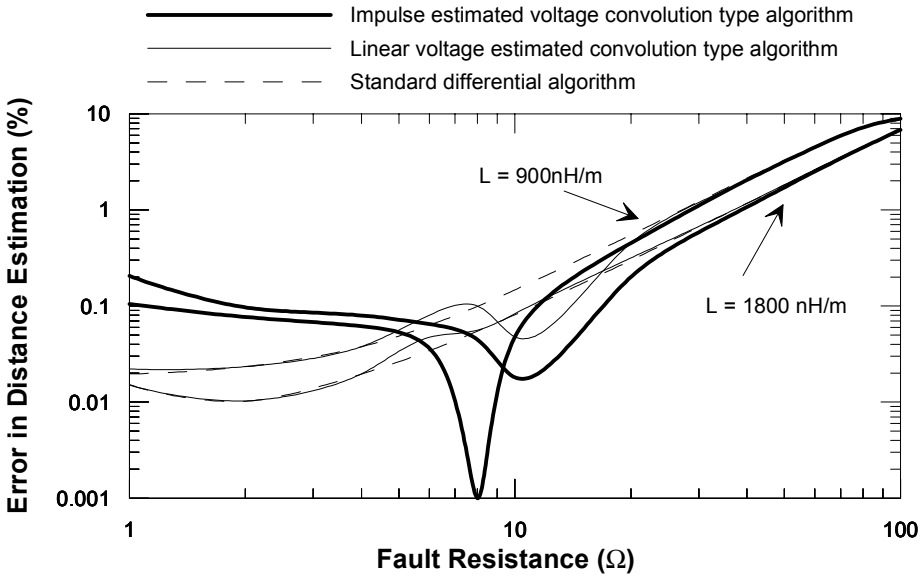

Figure 3.2: Error in estimation of distance to fault using various algorithms as a function of fault resistance R_g (Circuit as in Figure 3.1 with variation in L as indicated in graph).

Figure 3.2 clearly shows that the accuracy of the algorithms is poor for large fault resistance. The accuracy of the algorithm using a pulse as voltage estimation is however not worse than the control algorithm and the convolution type algorithm using a linear voltage estimation. The results however show that the linear estimated

voltage convolution type algorithm give almost identical results to the control (integral dynamic operator type) algorithm.

The accuracy of the convolution algorithm with pulse estimation also decreases for very large X/R ratio values. The algorithm's output signal oscillated around the true distance to fault. The oscillation decreases with time while the accuracy increases. The reason for this decrease in accuracy is found in a paper by Akke and Thorp [23]. The DC offset transient is much longer for these high X/R values, which are directly proportional to the time constant of the circuit. The DC offset causes low current gradients at low current values. The small current gradient causes a small de-numerator in Equation (3.4) while the small current value causes a small numerator in Equation (3.4). The result is noise divided by noise, which will give inaccurate results. The convolution algorithm with pulse estimation is more susceptible to this problem than the control algorithm (integration algorithm) and convolution algorithm using the linear voltage estimation.

3.1.4 Accuracy of algorithms for variation in sampling frequencies

The second parameter that might influence the accuracy of Equation (3.3) is the sampling period. The first term on the right hand side of Equation (3.3) will also become negligibly small for large sample periods and will, once again, make the current dependant on the system voltage and inductance only. The influence of the resistance will become negligibly small.

The same differential circuit equations for the circuit in Figure 3.1 were used to determine the influence of the sampling frequency on the accuracy of the algorithm. The algorithms' sampling period were varied logarithmically between 20μs and 800μs. This was done for four different X/R ratios. The simulation results in Figure 3.3 show that the accuracy of the algorithms is not affected for sampling periods up to 200μs, but changes dramatically for sampling periods larger than 200μs. Surprisingly, the accuracy of the impulse approximation convolution type algorithm for small X/R system ratios increase with a decrease in sampling frequency. This increase is only temporary and the accuracies decrease again for large sampling periods.

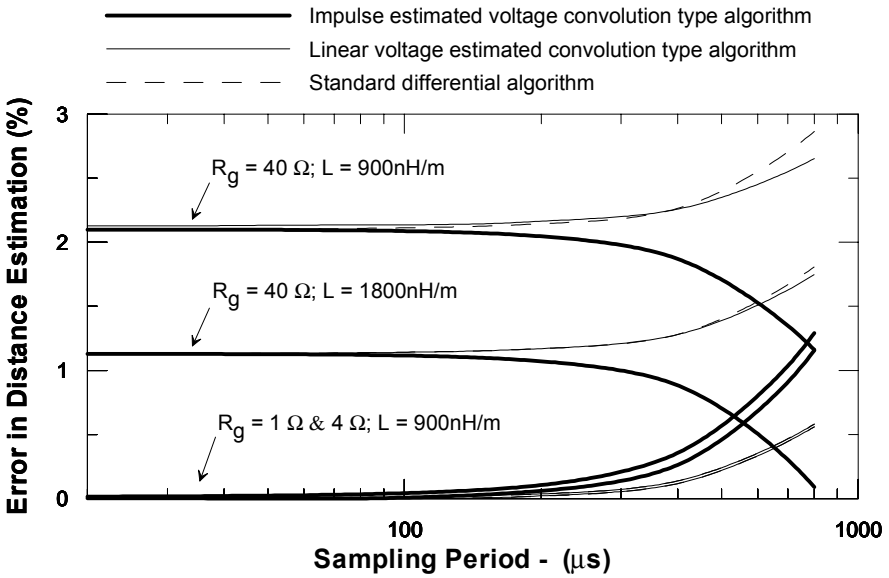

Figure 3.3: Influence of the sampling period on the accuracy of the algorithms. Simulations were done for various fault resistance and total line inductance values.

3.1.5 Single-phase simulations using a distributed parameter line model

The previous simulations were all conducted using a pi-modelled line. The final three-phase model will be based on distributed parameter lines to increase the accuracy of the simulations. In this section, part of the simulations done in Section 3.1.3, will be repeated with a distributed line model instead of a PI-modelled line. The same distance to fault (15km), source impedance, line inductance, line capacitance and line resistance will be used.

The distributed parameter line model is based on the Bergeron's travelling wave method used by Electromagnetic Transient Program (EMTP) [57] and is part of the standard models that are available in SIMULINK. In this model, the loss less distributed LC line is characterized by the surge impedance and travelling speed of the wave. These values are purely dependant on the capacitance and inductance of the line. The model does not represent accurately the frequency dependence of the resistance, capacitance and inductance of real overhead lines and it also ignores skin

effects in the conductor and the ground. The distributed parameter model is however still more accurate at high frequencies than the standard PI-model.

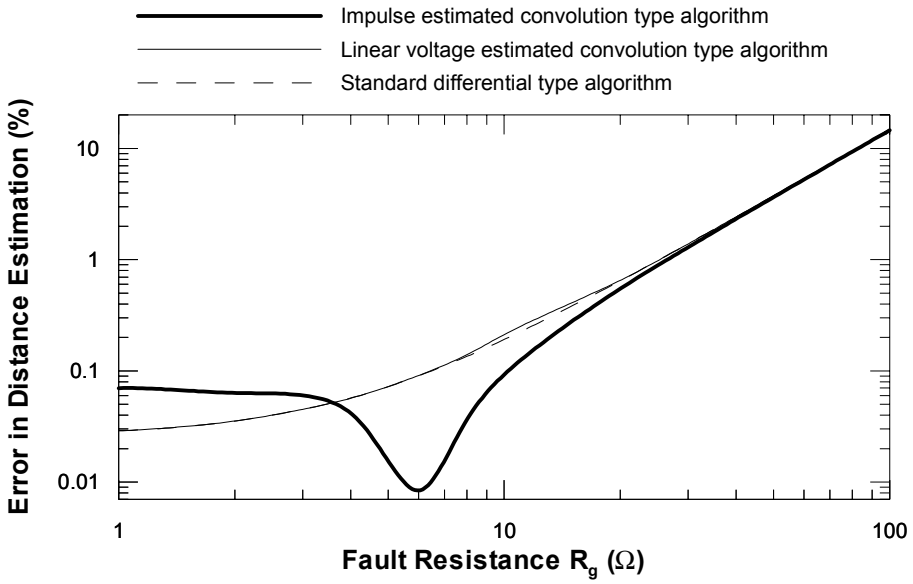

Figure 3.4: Accuracy of fault locator algorithms on single-phase distributed parameter line model for various fault resistances up to 100Ω. Distance to fault = 15km; line inductance = 0.9mH/km; line resistance = 100.0mΩ/km; Line capacitance = 13.0nF/km. Refer to Figure 3.2 for accuracy tests on an identical network with a pi-model line.

The accuracy of the different fault locator algorithms using a single-phase distributed line is shown in Figure 3.4. The circuit parameters are identical to that shown in Figure 3.1 with the exception of the line model. The results in Figure 3.4 compares well with the results obtain from the PI-modelled line (Figure 3.2) for fault resistances smaller than 80Ω. The larger errors obtained for the distributed line model for large fault resistances show the importance of accurate line models in accuracy tests of fault locator algorithms.

The same accuracy tests for a simulated fault on a distributed parameter line model were also done with different circuit parameters. The line parameters were calculated using the symmetric sequence circuits connected for a single-phase to ground fault (refer to Section 3.4). The effective series impedance for such a single-phase circuit is given by Equation (3.9) and will also apply for sequence resistance components. This equation is derived with the assumption that al three sequence

component currents are equal (bolted fault). Leakage capacitance is however modelled by a shunt capacitors. Because the calculation of an equivalent shunt capacitance is highly complex, the zero sequence line capacitance will therefore be used in the single-phase model. The following line parameters were calculated by using Equation (3.9) and line impedance values in Table 3.1: *Line inductance* 1.9978mH/km, *resistance* of 137.28mΩ/km and *capacitance* of 10.489nF/km. The distance to fault was kept on 15km, which is identical to that of the previous simulations.

$$X_{L_{eq}} = \frac{2}{3} X_{L1} + \frac{1}{3} X_{L0} \tag{3.9}$$

The results for these simulations are shown in Figure 3.5. The accuracy of the fault locator algorithms was less dependent on the fault resistance than during the simulations of the previous circuit. The main reason for this smaller dependency is the larger line inductance and resistance per unit length. The fault resistance has therefore a smaller influence on the overall X/R ratio of the faulted network.

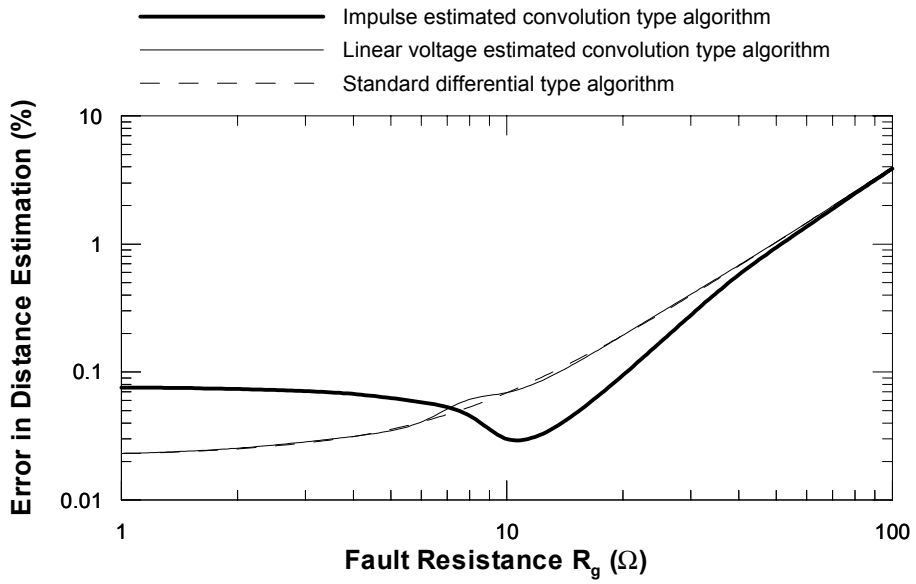

Figure 3.5: Accuracy of fault locator algorithms on single-phase distributed parameter line model for various fault resistances up to 100Ω.
Distance to fault = 15km; line inductance = 1.9978mH/km; line resistance = 137.28mΩ/km; Line capacitance = 10.489nF/km.

3.1.6 Conclusion of single-phase simulations

Two new differential equation type algorithms for single-phase systems were presented in this section. An existing integral type differential Equation algorithm was used as a control to evaluate the performance of these algorithms under constant fault resistance conditions for various sampling frequencies. The results indicated that the performance of these two algorithms is just as good as the existing integral type differential Equation algorithm. It was seen that the impulse estimated convolution type differential Equation algorithm is more susceptible to inaccuracies due to DC offsets than the control algorithm. The results of the linear estimated convolution type differential equation algorithm is almost identical to the control algorithm. The algorithm is however much more complex and has, therefore, no commercial use.

The results also indicated that the accuracy is influenced by the X/R ratio as seen from the measuring point. The accuracy of the differential type fault locator algorithms decreases if the X/R ratio decreases.

3.2 Differential Equation algorithms for three phase circuits

An equivalent single-phase circuit for a unsymmetrical fault on a three-phase circuit will consist of positive, negative and zero sequence impedances. The individual sequence impedances will influence the specific current sequence component. This difference poses a major challenge for the time domain impedance type fault locator algorithms. The standard differential equation algorithms require that the equivalent loop impedance be used. This loop impedance is estimated by Equation (3.9). This method however ignores pre-load conditions. The Radojevic *et. al.* [6] algorithm addresses this problem by only using the measured and zero sequence currents. The calculation of the zero sequence current in the time domain is a simple addition of all three sampled phase currents. In this section it will be shown that the convolution operator differential equation algorithm can also easily be transformed into a three-phase network algorithm that does not require the use of positive and negative sequence currents and voltages. The more complex convolution type algorithm that

uses the linear estimated voltage signal was too complex to be transformed in the same way.

3.2.1 Transformation of the algorithm using the impulse voltage estimation

Unsymmetrical Earth Faults

Figure 3.6 shows an equivalent single-phase circuit for a three-phase circuit with a single-phase to ground fault where the line capacitance is ignored. A complete mathematical derivation of a differential equation describing Figure 3.6 can be found in [58]. However, Figure 3.6 assumes that the line resistance consists of positive sequence resistance, zero sequence resistance and fault resistance whereas Johns *et. al.* have combine the sequence resistances into a single resistance [58]. The use of sequence component resistances is necessary to simplify the derivation of the final algorithm.

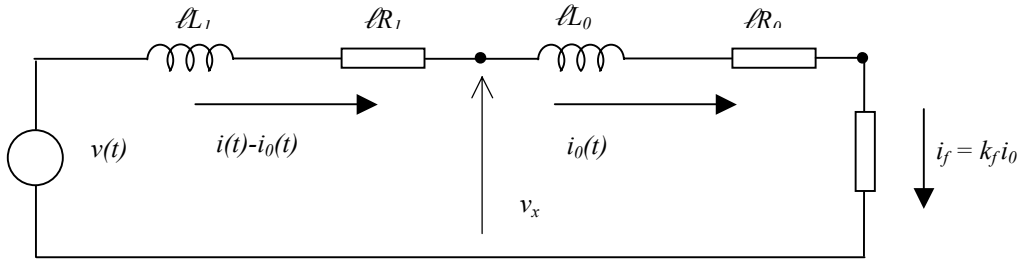

Figure 3.6: Equivalent single-phase circuit for a single-phase to ground fault on a three phase circuit.

$$i_{k+1} - i_{0_{k+1}} = \left(i_k - i_{0_k}\right)e^{-\frac{\Delta t}{\tau_1}} + \left(\frac{\Delta t}{\ell L_1}\right)\left(v_k - v_{x_k}\right) \tag{3.10}$$

$$i_{0_{k+1}} = i_{0_k}e^{-\frac{\Delta t}{\tau_0}} + \left(\frac{\Delta t}{\ell L_0}\right)v_{x_k} \tag{3.11}$$

Equations (3.10) and (3.11) are derived from Figure 3.6, describing the current of that specific part of the circuit as a function of the voltage and circuit parameters. These two equations are based on Equation (3.3) that is derived by using a convolution operator. The back-feed factor k_f became a part of the zero sequence

time constant τ_0. It is assumed that the back-feed factor will be constant over a three-sample data window. The variable v_x is eliminated by combining Equation (3.10) and (3.11) and will contain two unknown values (zero sequence time constant τ_0 and distance to fault ℓ). Again, two independent equations are needed to calculate the two unknown values. These two equations are established by using the current and voltage values of three consecutive samples. The final algorithm for a single-phase to ground fault is presented by Equation (3.12). A complete derivation of Equation (3.12) is shown in Appendix I.

$$\ell = \frac{\Delta t}{L_1}\left(\frac{q_{k+1}v_{k-1} - q_k v_k}{p_k q_{k+1} - p_{k+1} q_k}\right) \tag{3.12}$$

where

$$p_k = \left(i_k - i_{0_k}\right) - \left(i_{k-1} - i_{0_{k-1}}\right)e^{-\frac{\Delta t}{\tau_1}} + \left(\frac{L_0}{L_1}\right)i_{0_k}$$

$$q_k = \left(\frac{L_0}{L_1}\right)i_{0_{k-1}}$$

$$\tau_1 = \frac{L_1}{R_1}$$

The true zero and positive sequence inductance are unknown. However, the unit length positive and negative sequence inductance are known and the ratio (L_0/L_1) can therefore be calculated. The same principle applies to the positive sequence time constant. It is impossible to apply the same principles to the existing differential equation algorithms described by Segui [24]. The only known method was introduced by Radojevic *et. al.* by using complex matrix calculations. This is one of the main advantages of the convolution operator type differential equation algorithm.

Unsymmetrical Phase-to-Phase fault:

The algorithm for a phase-to-phase fault was derived using the same method presented for a single-phase to ground fault. Only the results will be given since the derivation is almost identical to that shown in the previous section. The same basic

Equation (3.12) is used but with different p and q values which will be calculated using Equation (3.13a) and (3.13b).

$$p_k = i_{a_{k+1}} - i_{a_k} e^{-\frac{\Delta t}{\tau_1}} + i_{b_{k+1}} \tag{3.13a}$$

$$q_k = -i_{b_{k-1}} \tag{3.13b}$$

3.2.2 Simulation of faults on a radial fed medium voltage network

It is now possible to test these algorithms on three-phase circuits to determine the accuracy of the algorithm. The influence of different faults on the differential equation algorithm was tested using SIMULINK and MATLAB. The fault signal was generated using SIMULINK while MATLAB was used to apply the algorithm. A radial fed medium voltage circuit was used since this work is concentrating on arcing in distribution systems. The line model is based on the Bergeron's travelling wave method as discussed in Section 3.1.5. The basic circuit used to simulate the line is shown in Figure 3.7 while Table 3.1 contains the details of the circuit parameters.

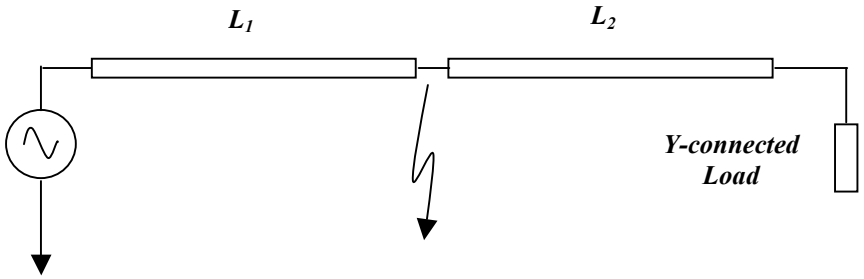

Figure 3.7: A faulted radial fed distribution network. The line parameters are shown in Table 3.1.

The line network parameters are based on the default settings of the models. The line inductance and capacitance closely resemble typical values calculated for a symmetrical line with conductor spacings of 700mm. The supply impedance was selected to obtain a 2kA fault level at the point of supply.

Table 3.1: Network parameters used for simulation of faults on three-phase radial fed circuits as shown in Figure 3.7

Power Element	*Parameter*	*Size*	*Unit*
Voltage Source	Frequency	50	Hz
	Amplitude	8950	V
	Supply resistance	0.1	Ω
	Supply Inductance	0.01	H
Overhead Line	Resistance (Zero sequence)	386.4	mΩ/km
	Resistance (Positive sequence)	12.73	mΩ/km
	Capacitance (Zero sequence	7.751	nF/km
	Capacitance (Positive sequence)	12.74	nF/km
	Inductance (Zero Sequence)	4.126	mH/km
	Inductance (Positive Sequence)	0.9337	mH/km
Load	Y connected Resistance (Floating Neutral)		
Static Arc Model	Static Model: Stoke's Equations[54]		
Dynamic Arc Model	Mayer model: Time constant	0.5	ms

The static arc characteristics are based on Stoke's empirical Equations obtained from experimental work on long, free burning arcs [54]. The dynamic properties of an arc are modelled by Equation (2.5) and the complete arc model is based in SIMULINK. The first set of simulations was done with a constant fault resistance to validate the derived algorithm for three phase systems.

3.2.3 Accuracy of the algorithm under a constant fault resistance fault

The differential equation algorithms were tested under constant fault resistance conditions on single-phase systems. The second set of simulations in Section 3.1.4 used impedances based on a single phase to ground fault on a three-phase network. The line parameters in Table 3.1 were used to calculate the equivalent circuit parameters (inductance and resistance) using Equation (3.9).

The derived differential equation algorithm was tested for a single phase to ground fault on a three-phase simulated network based on the parameters in Table 3.1. The line L_2 in Figure 3.7 was removed while the remaining line's (L_1) length was set to 15km. This system therefore represents the same three-phase system used to derive the parameters for the single-phase distributed line model in Section 3.1.5 with the results of the accuracy tests shown in Figure 3.5.

The accuracy of the algorithm for a three-phase network is compared in Figure 3.8 with the equivalent single-phase simulation results of Section 3.1.5. The three-phase system produces more accurate results for fault resistances larger than 20Ω. Line charging current due to line capacitance is the main reason for the more inaccurate results of the single-phase circuit algorithm.

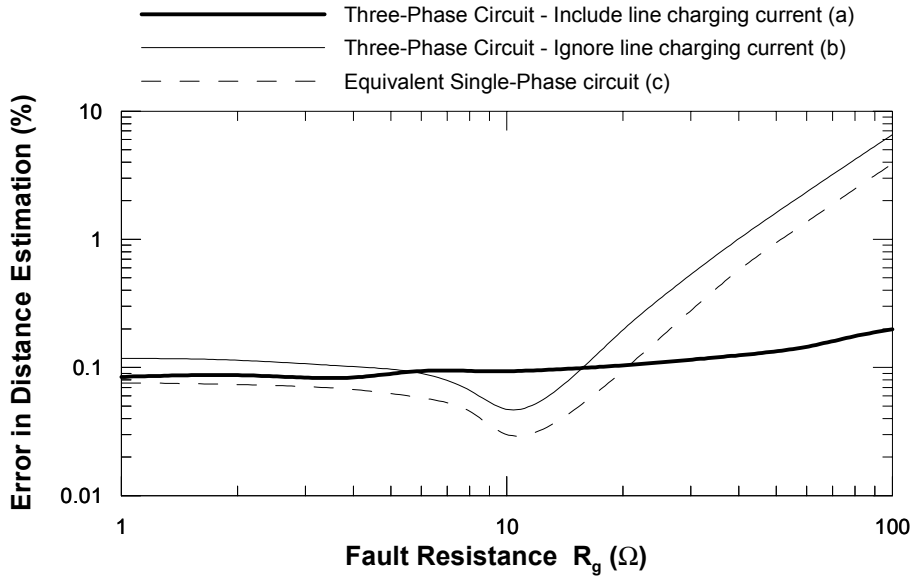

Figure 3.8: Accuracy of fault locator algorithms for three-phase and equivalent single-phase circuits.
True distance to fault of 15km – tests conducted on (a) three-phase circuit with algorithm including the positive sequence line charge current; (b) three-phase circuit with the algorithm ignoring positive sequence current and (c) equivalent single-phase circuit with line inductance and resistance based on Equation (3.9) also shown in Figure 3.5.

A third graph with the same characteristics as the single-phase model is also shown in Figure 3.8. This graph represent the results obtain from the algorithm for a three-phase circuit with a slight modification in the calculation of the zero sequence current. The calculation of the zero-sequence current component was modified to ignore the phase currents in the two healthy phases that consists mainly of line charging current. The zero sequence current is normally represented by a third of the summation of all three phases. In the single-phase representation it is normally assumed that the current in the two healthy phases are zero and the zero sequence current is therefore a third of the actual measured current.

The estimated impedances for the single-phase model that were used in paragraph 3.1.4 make use of Equation (3.9). This equation is derived by the assumption that the current is zero in the healthy phases. The accuracy of the three-phase algorithm, with the approximation of the zero sequence current component, closely resembles the results of the single-phase algorithm (Figure 3.8). From this graph it is safe to conclude that the positive sequence current due to the capacitance of the line causes inaccuracies in the single-phase models.

The three-phase algorithm produce better results since the capacitive component of the current is excluded from the estimated zero sequence current. The error that is produced by the algorithm is much less dependent on the fault resistance than the equivalent single-phase model.

3.2.4 Dependency of algorithm accuracy on load current

The presented algorithm is derived from an equivalent single-phase circuit in such a way that the distance estimation should be independent of the load current. The positive, negative and zero sequence voltage potentials between the measuring point and point of fault is a pure function of the measured sequence component currents and impedances in that part of the circuit. These values are all measured at the feeder. The voltage across the fault is equal to the product of the fault resistance and the total zero-sequence current component. The measured zero sequence current at the feeder is equal to the current flowing through the fault if no neutral to ground, on the load side of the measuring point, exists.

This is typical for distribution systems that are using Dyn type of transformers on the load side. This scenario was simulated on a 20km line with a delta-connected load at the end of the line and a constant resistance fault at the centre of the line. The load and fault current were varied by changing the respective values of the load and fault resistances. The results of the simulations are presented in Figure 3.9.

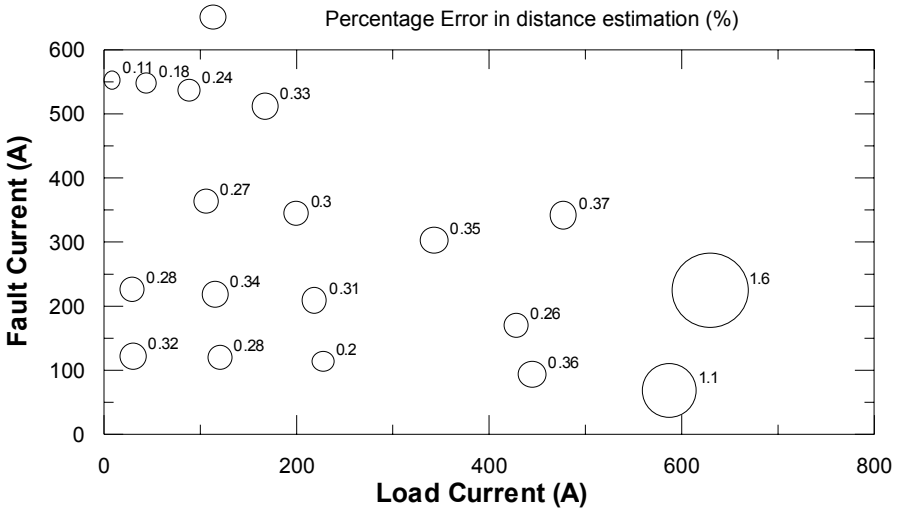

Figure 3.9: Error in distance to fault estimation of the three-phase differential type algorithm under loaded conditions.
The area of the "bubble" on the graph represents the size of the error. The load current is defined as the current in the faulted phase flowing into the load while the fault current is the actual current through the fault resistance.

A maximum error on the estimated distance to fault was 1.6% during a condition where the fault current was less than 40% of the load current. From these results it can be concluded that the proposed algorithm is independent of the load current if no current path to ground other than that of the fault exists on the load side of the feeder.

The presented algorithm does make provision for back feed currents from remote supplies. This is based on the assumption that the back feed zero sequence current is proportional to the zero sequence current measured at the local feeder. The same simulations were run as discussed above with the exception that the load neutral is earthed. This was done to test if the assumption will hold for alternative zero sequence paths that also feed zero sequence currents into the fault.

The results of these simulation showed that this assumption does not hold. An error of 134% was calculated for a distance estimation with a 124A load current and 122A fault current. Under the same conditions with no neutral to earth an error in the distance to fault was calculated to be less than 0.28% indicating, without doubt, that the assumption does not hold. It shows the advantage of using Dyn transformers in distribution systems when accuracy of distance protection relays is important.

It is worthwhile to mention that the algorithm for phase-to-phase faults will be load or resistance dependant. The current feeding into a phase-to-phase load will be unknown due to sequence current flowing from the load side. However, the accuracy will be improved if the fault resistance is reduced since a smaller voltage drop over the fault resistance is expected. Fortunately phase-to-phase faults normally have small resistive values and one can assume that the load current will not have a major influence on the accuracy of the algorithm.

3.2.5 Simulation of a long, free burning arc

This section will show some typical results obtained from the proposed model for long free burning arcs on an overhead line. The different static arc models were already discussed in the literature review. The arc will be modelled with the Mayr model Equation (2.5) for the dynamic behaviour of arc resistance as well as the empirical equation of Stokes [54]. This Equation is showed in Table 2.2 and will be used to calculate the static arc resistance required for the above-mentioned model.

The time constant τ of Equation (2.5) is empirically derived from cyclograph (experimental voltage-current plots) to obtain the best fit. The empirical Equation (2.7) presented in the literature review shows the relationship between the time constant, current and arc length. The time constant is primarily responsible for the initial rate of rise on the cyclograph. The ratio of the peak voltage V_p and 27% of the peak current I_p is always constant. The voltage gradient at this peak voltage is shown to be 15V/cm for high current arcs [53].

This work concentrates on high current faults on medium voltage lines. The arc length will vary between a few centimetres up to two meters while the fault current will be around 2000A. A constant time constant will be used in the simulations of the arc. It has been demonstrated that a 0.5ms time constant is ideal for medium voltage systems. The system was tested on a simulated distribution line with a peak fault current of 1kA.

The arc current and voltage for this specific simulation is shown in Figure 3.10 while the arc resistance is shown in Figure 3.11. The time constant influences the shape of the arc voltage which will become more square-wave like for a decrease in the time constant while it will become more sinusoidal wave-like for an increase in the time constant.

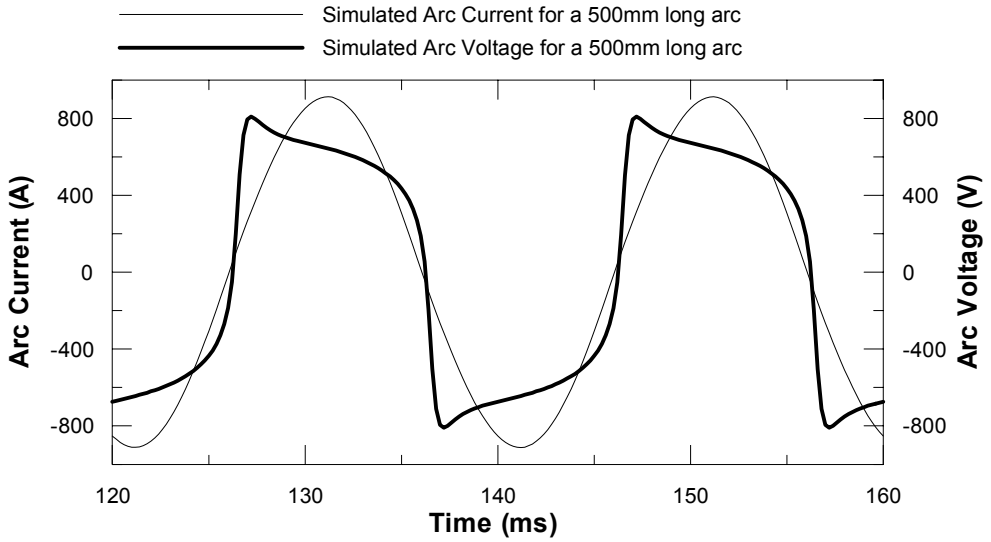

Figure 3.10: Arc voltage and current for a 500mm, 1000A peak simulated arc caused by a single-phase to ground fault in the centre of a 20km line

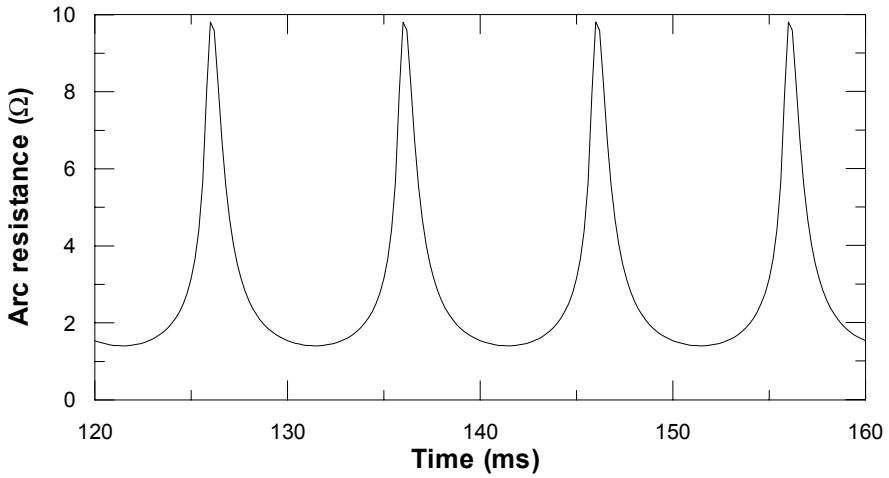

Figure 3.11: Arc resistance of a 1000mm long, 1000A peak simulated arc.

The larger arc model time constant will reduce the possible rate of arc resistance change. The time constant plays an important role especially during the current zero periods, where the static arc resistance increase rapidly as the arc current decreases to

zero. Smaller time constant will allow the true simulated arc resistance to increase to larger peak values than those for a larger time constant.

3.2.6 Accuracy of the differential type algorithm under arcing conditions

It has been demonstrated in the previous section that the presented algorithm is stable under existing testing methods using constant resistance faults. An arc was introduced onto the circuit to test the influence on the accuracy of the differential equation algorithm. The initial test showed a very unstable output and a post-median filter was introduced to increase the stability of the algorithm [23]. The instability of the algorithm was measured by calculating the standard deviation as a percentage of the true distance to fault.

The influence of the non-linearity will increase as the arc length increases. The first simulations that were conducted were used to test the influence of the arc length on the accuracy and stability of the algorithm. The distance to fault was 5km, 10km and 15km respectively on a 20km line with a load resistance of 50Ω. A post median filter of the 40^{th} order (8ms data window) was used to cope with the large variance in the output. It was found that a larger window is required than the proposed 5ms data window [23] due to the non-linearity of the arc resistance. The error was again calculated as the standard deviation from the true distance to fault. The error and standard deviation value of the filtered and unfiltered output is shown in Figure 3.12 and Figure 3.13 respectively. The error in the distance to fault estimation increases with the increase in the arc length. The large error of the unfiltered estimation is due to the large instability of the algorithm's output and is of the same amplitude as the error in the estimated distance to fault. This large error indicates the necessity of the median filter to improve the accuracy of the algorithm to more acceptable levels.

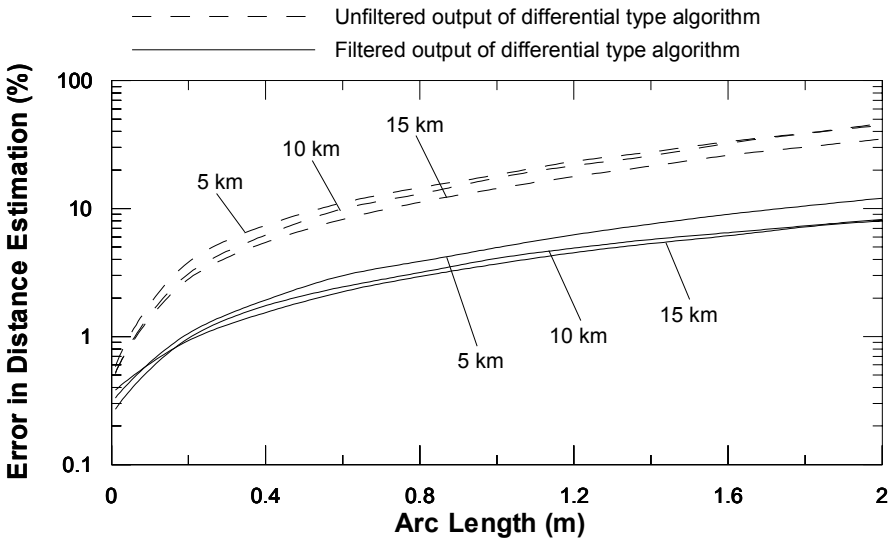

Figure 3.12: Accuracy of differential Equation algorithm for various arc lengths. Faults simulated for distance to fault of 5km; 10km and 15km on a 20km overhead line.

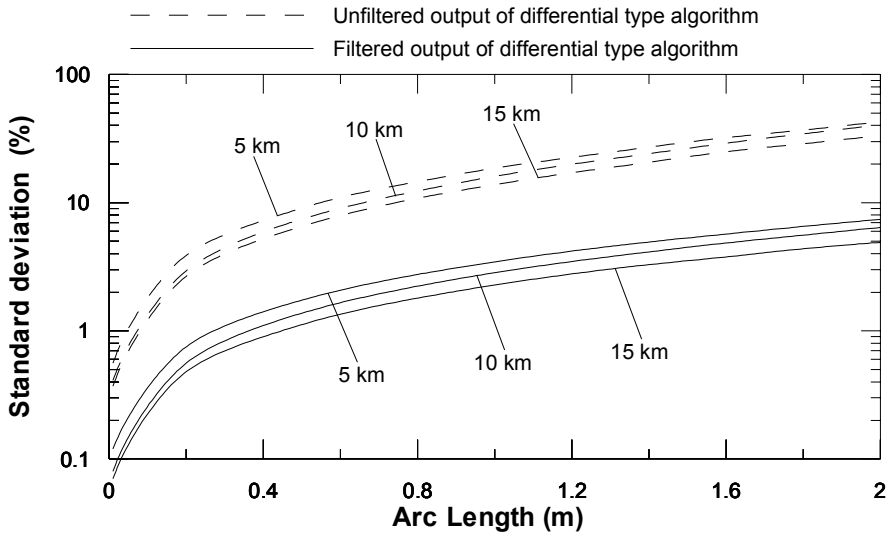

Figure 3.13: Standard deviation of the output signal of the algorithms for various arc lengths. Faults simulated for distance to fault of 5km; 10km and 15km on a 20km overhead line.

It has already been demonstrated that the error increases with the increase in the fault resistance and happens without non-linear arcing properties or pre-load conditions. The next set of simulations was done to determine whether the increase in error with the increase in arc length is due to an increase in non-linear properties or resistance. The rms value of the true arc resistance for the various arc lengths were calculated for each fault that was simulated at 10km. These resistance values were used to

simulate a constant resistance fault at 10km. The results are presented in Table 3.2 and clearly indicate that the errors obtained with the constant resistance faults are much smaller than the errors for the equivalent arc length. The decrease in the accuracy of the algorithm for an increased arc length is therefore purely due to the increase in the non-linear properties of the arc and not the actual increase in the rms value of the fault resistance.

Table 3.2: Errors of differential type fault locator algorithm due to a fault at the centre of a 20km long distribution line. The first set of errors is due to a constant resistance equal to the RMS value of the arc resistance shown in the second column.

Rrms(Ω)	*l(m)*	e_{cons}%	e_{arc}%
0.781	0.2	0.22	1.06
1.503	0.4	0.22	1.93
2.235	0.6	0.22	2.99
2.984	0.8	0.22	3.86
3.754	1.0	0.22	4.95
4.544	1.2	0.22	6.24
5.361	1.4	0.21	7.56
6.221	1.6	0.21	9.01
7.110	1.8	0.21	10.46
8.054	2.0	0.21	12.04

All of the accuracy tests were conducted without any filtering of the input voltage and current signals. The accuracy tends to increase slightly on long arcs if these signals are filtered. During these tests a 2m long arc fault was simulated in the centre of a 20km distribution line. The voltage and current signals were filtered with an 8^{th} order low past Butterworth filter with a cut off frequency of 640Hz. The accuracy of this scenario increases from 12.03% to 10.74% while the stability improved by 0.3%. Because the result indicates no major increase in accuracy, filters were therefore not used in the testing of the accuracy of the algorithm.

3.2.7 Accuracy of the algorithm under dynamic arc length conditions

The variation of the arc length should, in theory, not have any influence on the accuracy of the algorithm. The algorithm uses incident values over a very short data window of three consecutive samples. No physical change in the arc is expected

within such a small period to cause inaccuracies in the algorithm. This hypothesis was tested on a simulated distribution line as described in Section 3.2.2. The rate of increase in the arc length was varied between 1m/s and 20m/s. The error was calculated for a period ranging from 10ms before to 10ms after the arc length reaches a length of 1m. The instability of the algorithm output was also calculated for the same period. Only the results of the algorithm using the median filter were evaluated (Figure 3.14) since the instability was unacceptably large (30%) without the post-median filter.

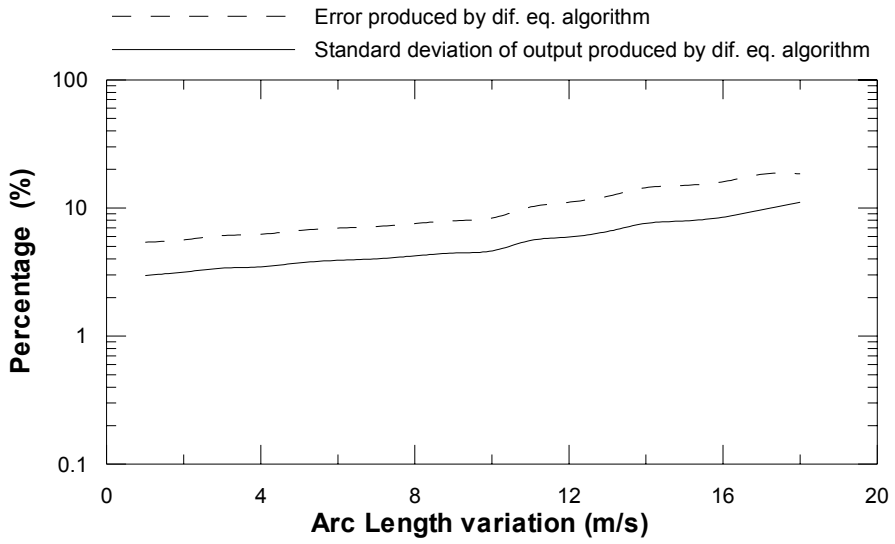

Figure 3.14: Influence of arc length variation on the stability and accuracy of the standard differential type algorithm.
Faults simulated at the centre of a 20km line.

The algorithm performed poorly even with a post-median filter during a variation in the arc length. The accuracy decreased by almost 13% while the instability increases with 8% for an increase in the rate of change of the arc length to 18m/s.

3.2.8 Estimation of the error cause by non-linearity of arcs

The instability of the differential equation algorithm under arc faults is caused by the variation in fault resistance. It is important to understand the exact causes of this instability for future development of time domain distance to fault locator algorithms. All differential equation algorithms make use of the assumption that the

fault resistance is constant over a predefined data window. This assumption is not true during arc faults. The resistance of an arc is higher during the current zero periods than during the maximum current periods. There will be a definite variance in the resistance for a predefined data window period. The derivation of the error for a three-phase circuit is highly complex. An equation will be derived for a three-phase circuit where it is assumed that the pre-load current is negligibly small.

Equation (3.14) is a modified standard differential equation to accommodate the variance in the arc resistance.

$$v'_{k+1} = v_{k+1} - i_k \delta R = L \frac{(i_{k+1} - i_k)}{\Delta t} + i_k R \tag{3.14}$$

In Equation (3.14), δR represents the variance in resistance for the predefined sample period. This equation is identical to Equation (3.5), except the reduction in voltage with the product of the current and resistance variation. The reduced voltage sample (v'_{k+1}) can replace the voltage sample (v_{k+1}) in Equation (3.12). This will only be valid for negligibly small pre-load currents. The error is described by Equation (3.15) where p and q is the same variables as defined by Equation (3.12)

$$\varepsilon = -\frac{\Delta t}{L_1}\left(\frac{q_k i_k \delta R}{p_k q_{k+1} - p_{k+1} q_k}\right) \tag{3.15}$$

The error was calculated for a simulated arc fault in the centre of the 20km distribution line. The load resistance was 1kΩ and the arc length was 1000mm. The unfiltered output of the algorithm as well as the summation of the error term and the true distance to fault is shown in Figure 3.15. The graph clearly shows that the instability of the output of the algorithm is primarily caused by the variation in the arc resistance.

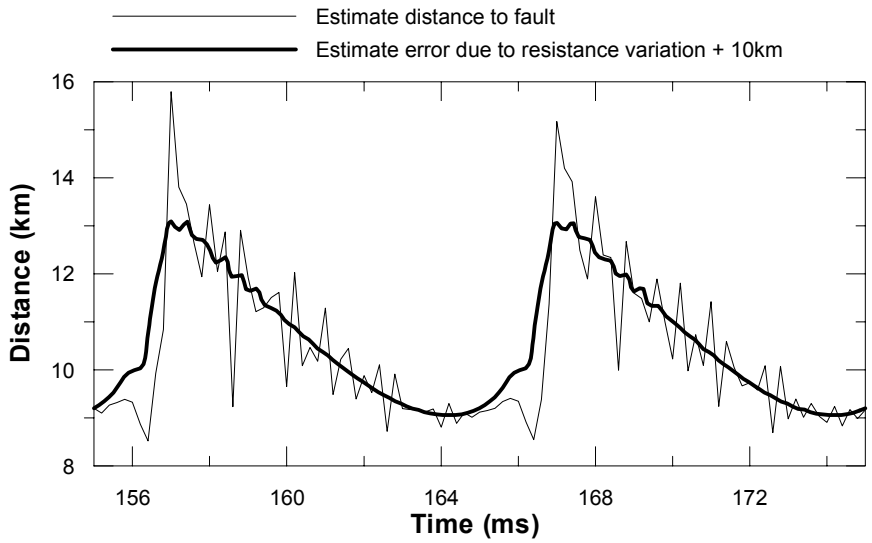

Figure 3.15: Error in the distance estimation due to resistance variation caused by arcing. Simulations done for a distance to fault of 10km; No-load conditions and arc length of 1m.

Equation (3.15) cannot be used to reduce the error since the resistance variation is unknown from the point of measurement. The equation can be used to understand the causes of the instability of the algorithms. It seems normally that the instability can be reduced by the increase in the sampling frequency. This will supposedly reduce the resistance variation between two consecutive samples. However, the instability will increase if the variation in current between two consecutive samples is reduced (Equation (3.15)) which will be the case if the sampling frequency is increased. The sampling frequency of the simulation was increased from 5kHz to 50kHz (20μs sampling period) and an arc fault with a length of 1m at the centre of the 20km distribution line was simulated. It was found that the instability has, in actual fact, increased by 1% to 17% for this faster sampling frequency of 50kHz. It is therefore clear that the increase in sampling frequency will not necessarily cause a more stable output during arc faults.

The arc resistance will have only small variances during the peak of the sinusoidal current waveform and one can expect more accurate results from the fault locator. The instability of the output is also directly proportional to the arc current (Equation (3.15)) and the error will therefore be greatly amplified during these periods although there are only small variances in the fault resistance. It is therefore not advisable to do selective sampling by only sampling in periods where one expects more constant

fault resistance values since the error is amplified by the large value of the current sample.

3.3 Evaluating Radojevic's modified differential Equation algorithm

Radojevic *et. al.* [2] proposed a modified differential algorithm that will include the variances in fault resistance due to arcing. This method uses the least square method as parametric estimation technique. The algorithm has two distinct features:

(i) The algorithm makes provision for an arc fault by approximating the arc voltage as a square wave. This feature makes it possible to use the least square method as parametric estimation technique to obtain a highly stable output. Radojevic *et. al.* showed that the output of the algorithm is unstable if this square wave approximation is excluded from the algorithm [6].

(ii) The algorithm makes provision for pre-loading without requiring the calculation of the positive and negative sequence current and voltage components. The derivation of the algorithm is based on the same principles and circuit (Figure 3.6) as discussed in Section 3.2.1 [6].

A data window is defined in which certain parameters are required to be constant. These parameters are the arc voltage amplitude, resistance (excluding the arc resistance), backfeed factor and circuit inductance. The square wave approximation of the arc voltage takes care of the variation in the resistance. The assumption for the constant parameters is therefore true for the resistance and inductance. The arc voltage is, however, highly dependent on the arc length. Faults that are incepted by conductor clashing or animals will cause a variation in the arc length and voltage. It is therefore necessary to test the influence of this variation in the arc length on the accuracy of the algorithm. The algorithm also assumes a perfect square wave arc voltage waveform. This is however only an estimation. A typical simulated arc voltage waveform for a long free burning arc is shown in Figure 3.10. True arc voltage waveforms for long, free burning arcs are not perfect square waveforms. The next section will investigate the accuracy of the algorithm under these non-square arc voltage waveforms.

3.3.1 Influence of arc faults on the accuracy of the algorithm

The algorithm was tested by using the same faults as described in Section 3.2.6. The algorithm performed better on long arcs than the convolution type differential equation algorithm. The results for different lengths of arc faults at different positions of the 20km simulated line are shown in Figure 3.16. The maximum error for the tests was 6.7%. This was obtained for an arc fault in the centre of the 20km simulated line with an arc length of 2000mm. The output of the algorithm was very stable. A maximum standard deviation of 0.12% was simulated during these tests. The equivalent resistance was also used to determine the properties of the algorithm under constant fault resistances. It was also evident that the non-linearity of the arcing influences the algorithm negatively. Table 3.3 shows that the error with a constant resistance equal to the rms value of the resistance of a 2000mm long arc is 0.09%. This inaccuracy is smaller than the 6.7% error simulated for a 2000mm arc at the centre of the 20km line. The algorithm performs better than the proposed differential equation algorithm with the post-median filter. The error of this algorithm was 12% in comparison with Radojevic's algorithm that produces a 6.7% error in the distance estimation for the same scenario.

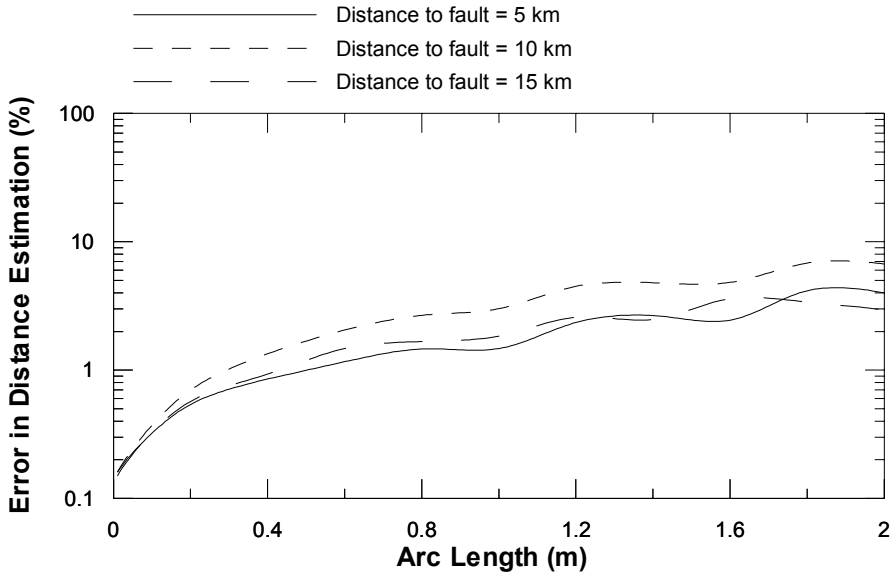

Figure 3.16: Accuracy of Radojevic *et. al.* differential Equation algorithm for various arc lengths.

Faults simulated for distance to fault of 5km; 10km and 15km on a 20km overhead line. Refer to Figure 3.12 for a comparison with the standard differential Equation algorithm.

Table 3.3: Errors of differential type fault locator algorithm due to a fault at the centre of a 20km long distribution line.
The first set of errors is due to a constant resistance equal to the RMS value of the arc resistance shown in the second column.

Rrms(Ω)	*l(m)*	e_{cons}%	e_{arc}%
0.78	0.2	0.07	0.70
1.50	0.4	0.07	1.34
2.24	0.6	0.07	2.05
2.98	0.8	0.07	2.67
3.75	1.0	0.08	3.01
4.54	1.2	0.08	4.51
5.36	1.4	0.08	4.80
6.22	1.6	0.08	4.82
7.11	1.8	0.08	6.82
8.05	2.0	0.09	6.69

The errors that were obtained in these simulations were smaller than what were reported by Radojevic *et. al* [6]. The primary difference between the simulations of this work and that of Radojevic *et. al.* is the line configuration. Radojevic *et. al.* concentrated on long transmission lines while this work is aimed at shorter radial fed distribution lines. One of the factors that influence the accuracy is the back-feed from remote supplies. A second factor that has a major impact on the accuracy of differential type fault locators is the existence of neutrals that are earthed on the load side of the measuring equipment. These earthed neutrals can be either that of a remote source or a load. Radojevic made use of remote sources with earthed neutrals that cause the larger errors that were reported in the paper [6].

3.3.2 Influence of arc length variation on the accuracy

The data window of Radijevic's algorithm was set on 200 samples (40ms). The algorithm assumes constant arc voltage amplitude in this period. It is expected that the algorithm will lose accuracy if the arc length is varied. This was tested on a simulated line as described in Section 3.2.2. The rate of the increase of the arc length was varied from 1m/s to 18m/s. Transients begin to influence the results for arc length increases larger than 18m/s. An arc length increase of 20m/s will cause an arc length of 2m within 50ms. This is the normal time required for the algorithm to converge. Tests at speeds higher than 20m/s will have no real meaning as the

algorithm is still converging. The error and stability were calculated for the period 10ms before to 10ms after the arc length reached a length of 1m.

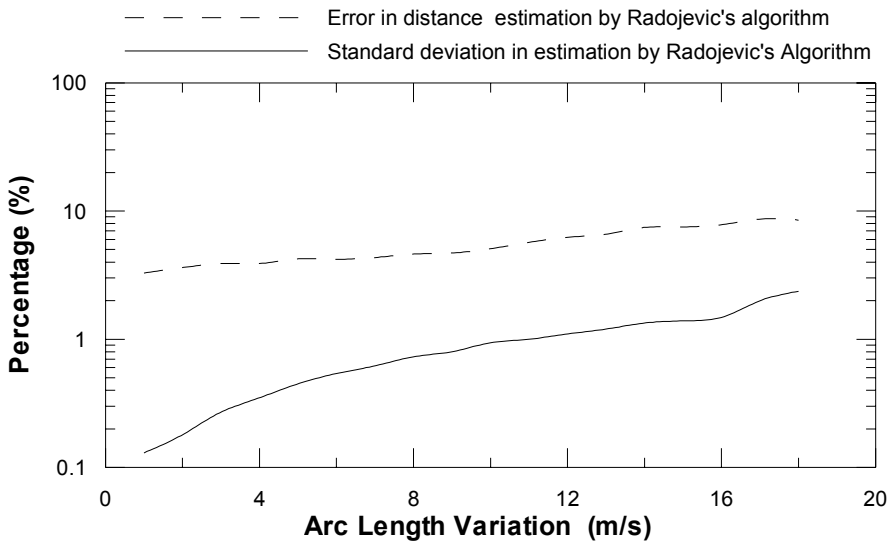

Figure 3.17: Influence of arc length variation on the stability and accuracy of the algorithm. Faults simulated in centre of a 20km line.

The results in Figure 3.17 show that the accuracy decreases with the increase in the arc length speed variation. These tests also indicated that the stability of the algorithm decreases with the increase in the rate of change of the arc length. In this specific test the accuracy decreased by only 1% due to the arc length variation. This algorithm outperformed the standard differential Equation algorithm that made use of a median filter as the parametric resolution technique (refer to Figure 3.14). There was, however, a large increase in the instability of the algorithm in comparison with a constant arc although the stability of the output was still better than the standard differential type algorithm with a post-median filter.

3.4 Conclusion

A new differential equation type distance to fault locator algorithm has been introduced in this chapter. The convolution operator is the fourth numerical approximation technique [24]. The relationship between the convolution operator using a pulse and the differential linear dynamic operator approach were pointed out by comparing Equation (3.3) and (3.6). It was shown that the two techniques differ only by the Taylor expansion of the natural exponential function. This new

differential equation algorithm was transformed to accommodate unsymmetrical faults on three-phase circuits. The algorithm also caters for pre-load conditions for earth faults if no earth-return paths other than the fault exist on the load side of the feeder.

An existing algorithm that uses the least square method as the parametric resolution technique was also evaluated in this section. Simulations showed that both these differential equation algorithms' accuracies decrease with the increase in fault resistance. The least square parametric resolution technique of this existing method outperforms the post-median filter technique used by the newly proposed algorithm under arcing conditions. This post-median filter was however required to stabilise the output under arc fault conditions.

All differential equation algorithms assume constant resistance during three consecutive samples. An arc fault causes instability due to the variation in the resistance during the pre-defined data window of three consecutive samples. It is however impossible to decrease the instability by increasing the sampling frequency due to the decrease in difference between two consecutive current samples. The proposed algorithm of Radojevic *et. al.* with the estimated square wave outperform the standard differential algorithm under arc fault conditions. The output of the algorithm is much more stable than a standard differential equation algorithm with a 40^{th} order post-median filter.

4 INFLUENCES OF MAGNETIC FORCES DUE TO PHASE-TO-PHASE FAULTS ON THE ACCURACY OF IMPEDANCE TYPE FAULT LOCATORS

In the previous section the influence of the non-linearity of an arc on the accuracy of a differential equation type fault locator algorithm was investigated. The algorithms assume a constant resistance over the sampling period. It was shown that the variation in resistance may cause instability in the fault locator algorithm. The algorithms calculate the total inductance between the point of measurement and the fault. It is assumed that the inductance per unit length of the line is known. The distance to fault is estimated by dividing the estimated inductance by the known inductance per unit length. This inductance value is predetermined in accordance with the line configuration and it is assumed to be constant during the fault.

Phase-to-phase faults on a network cause two equal currents with opposing directions on the two faulted phases. This will excite opposing forces on the conductors forcing them apart. The line inductance is dependent on the distance separating the conductors. An increase in the distance between the two conductors will cause an increase in the inductance. The distance to fault locator will produce wrong estimations since the estimated total inductance will be divided by an incorrect inductance per unit length.

In this section, a finite element conductor model based on existing non-linear wave equations derived from Newton's first law is used to evaluate the dynamic response of the conductors during a phase-to-phase fault. The investigation will focus on the influence of such dynamic behaviour during the fault on the accuracy of the fault locator algorithm.

4.1 Modelling of the conductor deviation during fault conditions

The *Transmission line reference book* [3] proposes a simple rigid body model to calculate displacement of the cable during the phase-to-phase fault condition. It

assumes a rigid body pendulum type arrangement in calculating the conductor displacement. The horizontal force is calculated using the distance between the mass centre points of the two parabolic-shaped conductors. However, a cable will lose its rigid body properties for large deviations from the rest position [59]. The steady state conductor deflection during a fault condition may be small enough to be calculated assuming a rigid body model. It is however important that the maximum amplitude of conductor displacement be calculated during the transient period to determine the maximum effect on the fault locator algorithm. The assumptions of the rigid body model cannot be expected to provide accurate results due to mechanical transients. The conductor needs to be treated as a flexible mass to allow more freedom of movement.

In-plane oscillation (taut-string) and out-of-plane swing have been evaluated as two separate movements for small amplitudes [60]. Equation (4.1) is a standard wave equation for a free, out-of-plane (swinging) oscillation of a single suspended cable viewed in plan [60]. The constant H represents the horizontal cable tension; ρ the cable mass per unit length and v the horizontal displacement from the centre line (natural rest position). The equation is only valid for out-of-plane oscillations without any external horizontal forces such as opposing magnetic fields as well as large oscillation amplitudes that will affect the horizontal component of the tension (H). This standard non-linear wave equation is only suitable for small amplitude oscillations. It cannot be used in the evaluation of the conductor movement during fault conditions since it is expected that the horizontal component of the cable tension will not be constant due to horizontal forces caused by magnetic fields.

$$H\frac{\partial^2 v}{\partial x^2} = \rho\frac{\partial^2 v}{\partial t^2} \tag{4.1}$$

The calculation of the extra tension on the cable due to the magnetic field poses a major problem because an increase in the horizontal component of the tension will cause a decrease in the maximum conductor deflection. Inclusion of this additional tension is vital for more realistic results. The simplest method for the calculation of the extra tension is by calculating the amount of stretching the conductor has undergone and this requires that the calculations be based in all three dimensions.

A three dimensional Cartesian axis is defined such that the line is swinging around the x-axis, while gravity is in the negative y-direction. The out of plane oscillation is therefore in the z-direction. The vector $\boldsymbol{r_i}$ with its individual components r_x, r_y and r_z is the displacement vector describing the position of a line-element i with a length of $|\boldsymbol{dr_i}|$ and individual components consisting of components dr_x, dr_y and dr_z. Figure 4.1 is a schematic diagram of such a line element.

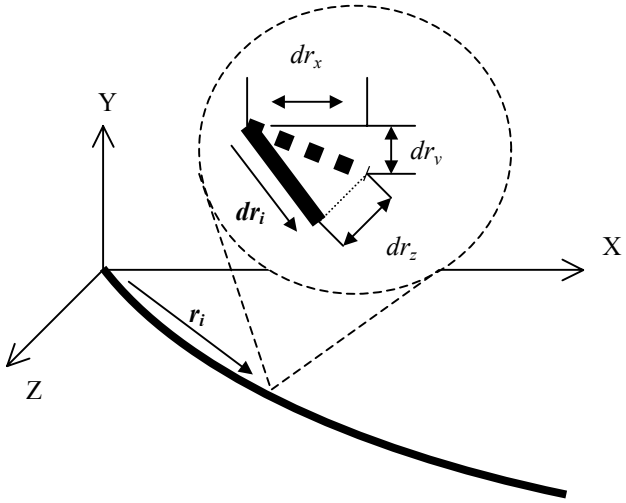

Figure 4.1: Schematic diagram of position vector $\boldsymbol{r_i}$ for an infinite small conductor element $\boldsymbol{dr_i}$

Equation (4.2) and (4.3) are two uncoupled scalar equations describing the in-plane and out-of-plane oscillation in the Cartesian axis defined by Figure 4.1 during a phase-to-phase fault. Phase-to-ground faults will not cause conductor deflection since only one conductor is carrying the fault current while it returns through the ground. In Equation (4.2) and (4.3), T_0 represents the initial mechanical conductor tension and T the additional tension due to cable movement and external forces. These equations are derived on the principles presented by Irvine [60] and are based on Newton's first law. There are no resulting forces on the small element ($\boldsymbol{dr_i}$) that would tend to change its position in the x-direction. The displacement of the element can therefore be calculated in the y- and z-direction from two scalar equations.

At the minimum point of the sag in a span, the line element length is equal to the horizontal component of the line element ($|\boldsymbol{dr_i}| = dr_x$ and $dr_y = dr_z = 0$). The values

of the line element vector will cause infinities in the y-z plane at the centre of the line. It was therefore necessary to assume that the cable tension component in the yz plane is negligibly small in comparison to the total cable tension. It can be shown that the vertical force is a maximum of 1.5% of the horizontal force at the supporting point of the conductor for a 200m span length Paw-Paw conductor that is tensioned to 10% of the ultimate tensile strength (Table 4.1). These calculations are based on the parabolic approximation of a sag span given by Equation (A2.1) (Appendix II). It is therefore safe to assume that the cable tension in the yz plane is negligibly small in comparison with the forces in the xz and the xy planes.

Tension waves will also travel at a relativistic speed in steel cables [38]. Any local change in the tension of the cable will equalise at the speed of light throughout the cable. The tension $T+T_0$ in Equations (4.2) and (4.3) is therefore a pure function of time and independent of the position on the cable.

The first term on the right hand side of Equation (4.2) and (4.3) represents the product of the horizontal component of the tension (in the xz-plane for Equation (4.2) or xy-plane for Equation (4.3)) and the second derivative of the displacement in the z or y direction with respect to x. This term is based on the same principles used to derive Equation (4.1) and will produce the resulting force on the infinitely small line conductor in the z and y direction respectively. The second term on the right hand side of Equation (4.2) represents the magnetic force. This term is based on the standard equation in calculating the forces between two parallel conductors carrying identical currents in opposite directions [61]. In Equation (4.2), the constant $\mu_0 = 4\pi\times10^{-7}$ is the magnetic permeability of air while the variable i represents the line current. It is assumed that the movement of the two conductors is identical and will therefore only exert a horizontal force on the second conductor. The second term of Equation (4.3) is the gravitational acceleration in the negative y-direction.

The initial conditions for the differential Equation (4.3) are a standard parabolic equation for a line in static equilibrium. The initial displacement of the conductor in the z-direction is assumed zero. This will be true if there is no wind forces act on the conductor (Equation (4.2)).

$$\frac{\partial^2 r_z}{\partial t^2} = \frac{\sqrt{dr_x{}^2 + dr_z{}^2}\,(T + T_0)}{\left|d\bar{r}\right|^2 \rho}\left(\frac{\partial^2 r_z}{\partial x^2}\right) + \frac{\mu_0 i^2}{4\pi d} \cdot \frac{dr_x}{\left|d\bar{r}\right| \rho} \tag{4.2}$$

$$\frac{\partial^2 r_y}{\partial t^2} = \frac{\sqrt{dr_x{}^2 + dr_y{}^2}\,(T + T_0)}{\left|d\bar{r}\right|^2 \rho}\left(\frac{\partial^2 r_y}{\partial x^2}\right) - g \tag{4.3}$$

A stiffness factor was originally included in both Equation (4.2) and (4.3) [62]. The change in the line profile over the total span is very small and no real damping was expected. The original simulations included damping due to stiffness as shown in [62]. The results obtain from the simulations that include stiffness were identical to those without any damping due to stiffness. The influence of the stiffness is therefore insignificantly small and was therefore discarded. This was done to reduce the complexity of the equation for evaluation purposes in the next section.

The two differential Equations (4.2) and (4.3) can easily be solved numerically to obtain the displacement of the cable and the increase in length as a function of time [63]. MATLAB was used to simulate the conductor displacement for various conditions. The line was divided into 200 elements with all 200 position vectors being calculated for each time step. After each time step the extra tension T in the cable is calculated by using Equation (4.4).

$$T = \frac{EA}{L}\Delta\ell \tag{4.4}$$

In Equation (4.4), E represents the Young-Modulus of the conductor, A the cross sectional area of the conductor, L the span length of the line and $\Delta\ell$ the increase in the conductor length with reference to the steady state condition under a constant tension T_0.

4.2 Validation of proposed simulation procedure

The proposed model was used to investigate the displacement of a conductor during fault conditions. The investigation focused on ACSR conductors which are the most widely use conductor in standard distribution networks. Table 4.1 shows manufacturing data obtained from a well-known Australian manufacturer of bare conductors. Three conductors were chosen based on their mass and UTS specification. The Paw-Paw conductor is a heavy conductor with high current carrying capabilities. The Grape conductor is seen as an average conductor while the Apple conductor is a small, lightweight conductor. The effective Young-modulus (Table 4.1) was calculated using the ratio of the cross sectional area of the specific material with reference to the overall cross sectional area.

Table 4.1: Specification of Australian Standard Metric Conductors

Data supplied by [64]

Name	*Apple*	*Grape*	*Paw-Paw*
UTS (kN)	14.9	63.7	179
Area of Aluminium (mm²)	41.8	144	583
Area of Steel (mm²)	7.68	37.6	88.7
Effective Density (kg/m)	0.171	0.675	2.25
Effective Young Modulus (MN/mm²)	0.08757	0.09404	0.08468
Overall Diameter of Conductor (mm)	9	17.5	33.8

The displacement of a Grape conductor under a 12kA fault was first simulated. The two phases carrying the fault current are on the same level with a 750mm horizontal separation. The asymmetry of fault currents was ignored since it is dependable on the exact time of fault inception as well as the X/R ratio of the system. The span length is 80m while the tension in the cable is assumed to be 25% of the ultimate tensile strength (Table 4.1). The result of this simulation is shown by Figure 4.2.

It is evident from this simulation that the deflection of the conductor under fault conditions is considerable. The conductor displacement in the centre of the span is almost triple the original conductor spacing of 750mm. The horizontal profile of the conductor only starts to take the shape of a parabola after 125ms. However, a three-dimensional analysis shows that the centre of the conductor swings further upwards than the rest of the conductor after 225ms. These results clearly indicated that the rigid model is not a true representation of the conductor displacement [3].

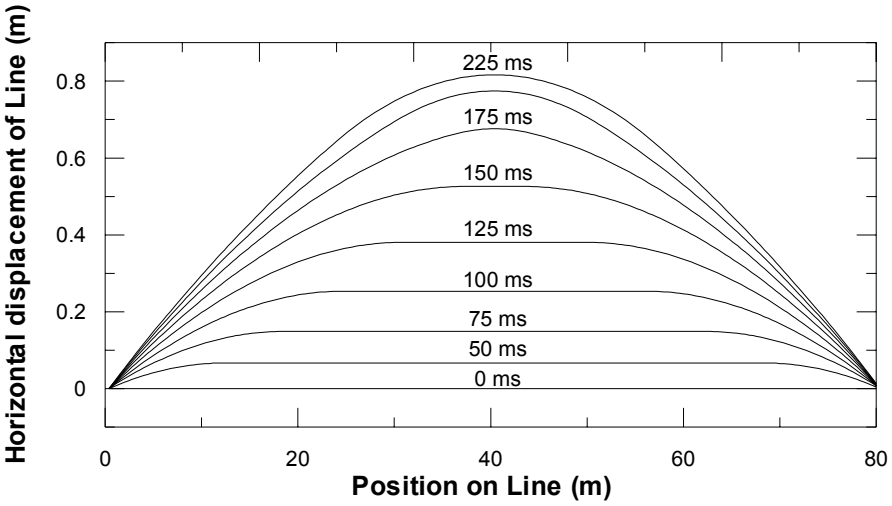

(a)

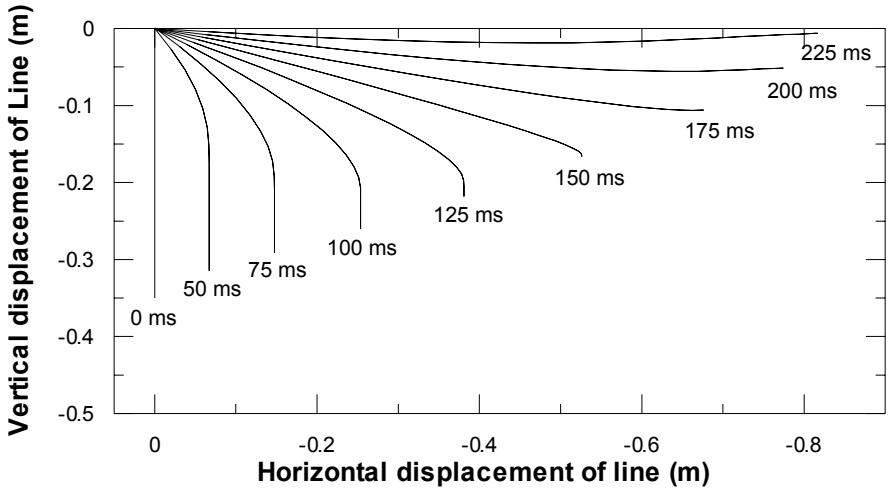

(b)

Figure 4.2: Estimated dynamic behaviour of a Grape conductor carrying a 12kA phase-to-phase fault current.
Conductor tension before fault = 25% of UTS; phase spacing = 750mm; span length = 80m. Graph (a) shows the horizontal displacement in plan; Graph (b) shows the displacement of the conductor as seen along the x-axis (Figure 4.1)

The line sag at the start of the fault is 0.35m. At 225ms, the "sag" is virtually horizontal with a deflection of 0.8m. The calculations also indicate that the line length increases by 17mm. Equation (4.5) can be used to calculate the difference between the true conductor length L, span length $S=80m$ and sag D [65]. It shows that the difference between the conductor length and span length (L-S) is only 4mm for a sag of $D=0.35m$. This difference in conductor length and span length (L-S) increase to 21mm for a sag of $D=0.8m$. These values indicate that the conductor length should therefore have increased by 17mm (21mm-4mm) when it reaches a

"sag" of 0.8m. This increase in the conductor length correlates well with the simulation values. These results validate the calculations in the increase in conductor length due to additional tension caused by the external forces and momentum of the conductor.

$$L - S = D^2\left(\frac{8}{3S}\right) \tag{4.5}$$

The model is also verified with experimental data obtained from the *Transmission line Reference book* [3]. The experiments were done with two parallel Dove conductors with a span length of 91m, sag of 1.32m and a conductor spacing of 910mm. The maximum deviation and time after fault that occurred were experimentally measured for a fault current of 2kA. The proposed model gave a maximum deviation of 0.22m after 0.9 seconds. The experimental results indicate a maximum conductor deviation of 0.19m after 0.9 seconds. The results of the rigid model are more accurate for this test case. It must be mentioned that the experimental case was only for low current faults causing a small deviation where the rigid body model is acceptable. It can be concluded that the model is accurate enough to be used to calculate the influence of the conductor displacement during the fault on the accuracy of the impedance type fault locator algorithm.

4.3 Influences off conductor deflection on algorithm accuracy

Time domain fault locator algorithms require at least 30-40ms to converge [6, 24]. Frequency domain fault locator algorithms require at least 50-60ms to converge [1]. This may even be longer since these algorithms are influenced by the DC offset of the fault current. The algorithms must also check for stability after convergence before it can operate. It is therefore evident that the displacement of the line due to magnetic forces on the overhead line may influence an impedance type fault locator algorithm.

It was already mentioned that the impedance type fault locator algorithms assumes that the inductance of the line during fault conditions is constant. If the line inductance increases during the fault condition, the estimated distance to fault will

decrease. The error that will be caused by the change in the inductance will therefore be equal to the ratio of the calculated line inductance per unit length to the actual inductance per unit length of the line during the fault condition. This ratio will be defined as the fraction of the true distance to fault. The inductance is dependent on the distance between the two conductors and will increase if this distance is increased. From this it is evident that the fault locator algorithm will under estimate the distance to fault due to the conductor deflection under fault current conditions.

The inductance of a line is dependent on the conductor configuration. This work will concentrate on a simple symmetrical line with a triangular configuration, which is widely used in rural distribution lines. Phase 1 and 3 are on the same horizontal level while phase 2 is above but equally spaced between phase 1 and 3. The average positive and negative sequence inductance per unit length of such a line is given by Equation (4.6) where *s(x)* is the spacing between two conductors, *S* the span length and *r* is the conductor radius [66].

$$L = \frac{1}{S}\int_0^S 10^{-7}\left(0.5 + 2\log_e\left(\frac{s(x)}{r}\right)\right)dx \tag{4.6}$$

The model developed in section 4.1 as well as Equation (4.6) was used to calculate the error in the estimated distance to fault. The previous equations show that there are various parameters that will influence the conductor deflection and therefore also the accuracy of the fault locator algorithms.

Equation (4.7) is used to derive the parameters that will influence the accuracy of the algorithm. This equation is derived from Equation (4.1) with the inclusion of the magnetic force. Equation (4.7) shows that the solution of the displacement v will increase with the increase of current I and decrease with the increase in cable tension H or conductor spacing d. The conductor mass ρ will only have an influence on the time scaling of the solution. The initial cable tension and mass will however have a major impact on the time of the response. The cable tension will increase the response time while an increase in the conductor mass will decrease the response time of the line during a fault.

$$\frac{\partial^2 v}{\partial\left(t\sqrt{H/\rho}\right)^2} = \frac{\partial^2 v}{\partial x^2} - \frac{\mu_0}{4\pi}\left(\frac{I^2}{H \cdot d}\right) \tag{4.7}$$

Influence of cable parameters on the accuracy of the fault locator

The influence of different conductors is demonstrated in Figure 4.3. The group of conductors consists of a heavy (Paw-Paw), medium (Grape) and light (Apple) ACSR conductor. The cable tension was set on 25% of the conductor's specific ultimate tensile strength with a conductor spacing of 750mm and span length of 60m (see Table 4.1).

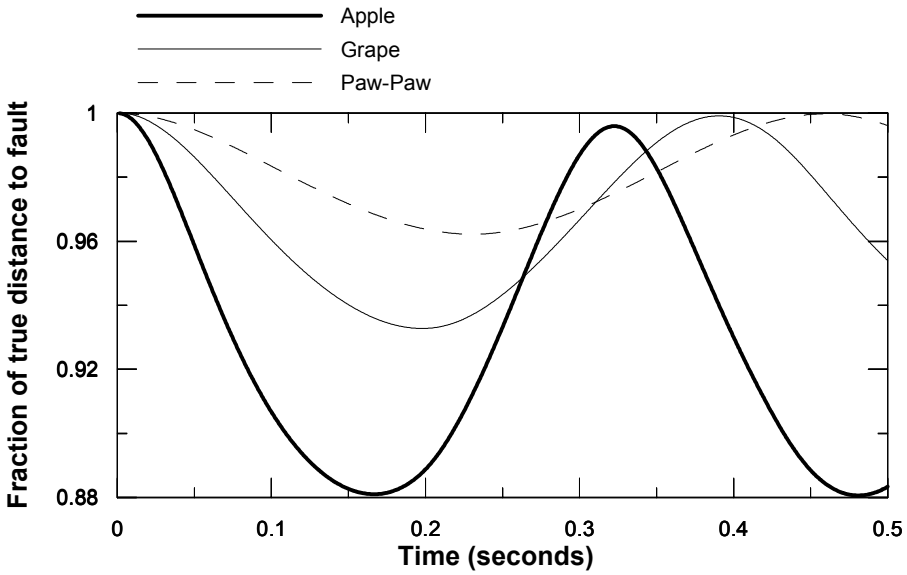

Figure 4.3: Influence of different conductors on the accuracy of algorithm during a phase-to-phase fault. Span length = 60m; Conductor tension = 25% UTS; Conductor spacing = 0.75m

Figure 4.3 indicates the interdependencies of the conductor parameters as well as the accuracy. It has previously been shown that the conductor mass primarily influences the time scaling of the solution. The major reason for the differences in estimated errors is due to the tension in the cable. Because the Paw-Paw conductor has a much higher initial tension, the amplitude of the solution of Equation (4.6) will be much smaller. The overall diameter of the Paw-Paw conductor is also much larger than that of the Apple conductor. This will require a much larger increase in tension for a

specific increase in conductor length as oppose to a lighter conductor such as Apple conductor.

The initial tension and cable diameter plays a positive role in the accuracy of the algorithm. The accuracy of a fault locator will be higher for heavy lines with high initial conductor tensions. Light conductors such as Apple, on the other hand, can easily cause estimation errors larger than 10% during fault conditions due to the fast response and high amplitude of the conductor displacement during a fault.

Influences of conductor spacing on the accuracy of the fault locator

Equation (4.7) shows that the solution of the differential equation will be inversely proportional to the conductor spacing *d*. The line inductance is logarithmic proportional to the spacing of the conductor. The same deflection for larger spacings between conductors will have a smaller influence on the inductance. This is a highly non-linear relationship. The relationship was tested for various conductor spacings for a 8kA simulated fault current on a line constructed with a Grape conductor. The initial tension of the conductor is 25% of the UTS with a ruling span length of 60m.

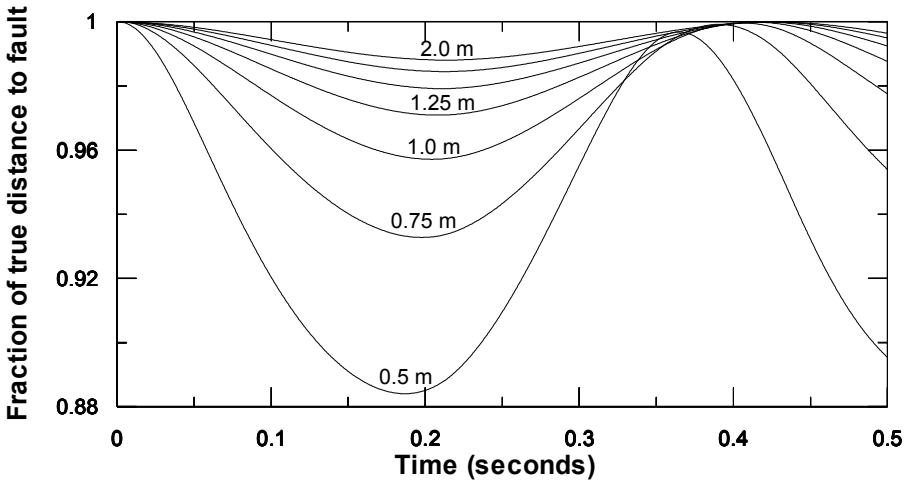

Figure 4.4: Accuracy of fault locator for various conductor spacings; Conductor type: Grape; Conductor tension: 25% of UTS; Span Length = 60m

The results in Figure 4.4 show that the inaccuracy for large conductor spacings tends to become negligibly small. This large conductor spacing will typically be found on 66kV distribution lines. The error is however significant for conductor spacings of

750mm and smaller which are common for 3.3kV and 11kV distribution lines. From these results it is evident that inaccuracies due to inductance variance are most likely to occur on 3.3kV and 11kV lines.

Influences of the ruling span length on the accuracy of the fault locator

The span length of the conductor is not included in the simplified differential Equation (4.7). However, the span length will have two indirect influences on the cable tension that will influence the solution of the differential Equation (4.7).

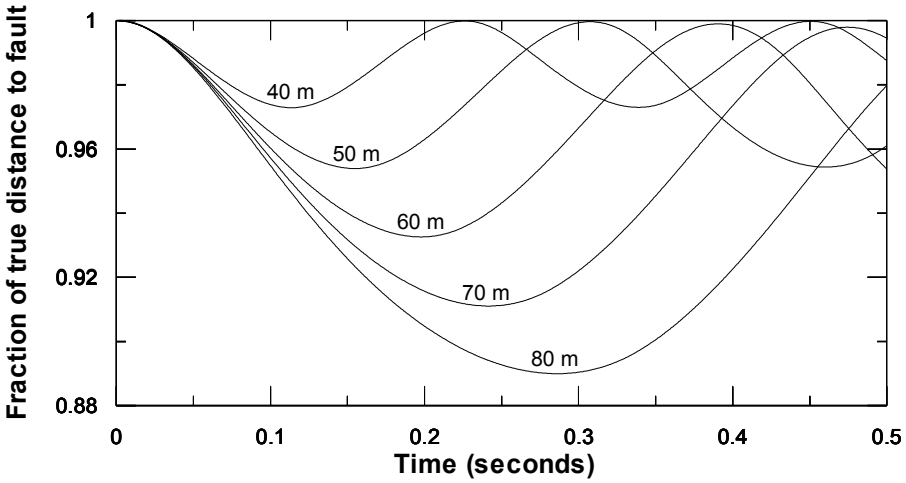

Figure 4.5: Accuracy of fault locator for various span lengths;
Conductor type: Grape; Conductor tension: 25% of UTS;
Conductor spacing = 750mm; fault current = 8kA.

The first influence on the cable tension can be derived from Equation (4.5). This equation shows that the sag *D* will increase for an increase in span length *S* but with a constant difference between conductor length and span length (*L*-*S*). The second influence can be seen from the calculation of conductor length increase due to extra tension in the conductor. The increase in length is proportional to the percentage length increase and not the actual conductor length increase. The conductor length increase for a long span length will therefore be greater than for a short span length although for the same increase in conductor tension. These two factors will cause a larger increase in conductor tension (*H*) on a short span length than on a long span length. The solution of Equation (4.7) is inversely proportional to the conductor

tension and fault locator algorithms will therefore be more accurate for short span length lines.

Various span lengths were simulated for a line constructed with Grape conductor and tensioned to 25% of the UTS. The spacing of the conductor was set to 750mm with a fault current of 8kA. The results of these simulations are shown in Figure 4.5.

Influences of the fault current on the accuracy of the fault locator

The solution of the horizontal displacement v in Equation (4.7) is directly proportional to the square of the fault current. A high fault current will therefore cause a larger magnetic force and conductor displacement. Figure 4.6 indicates the influence of different fault currents for a Grape conductor with a conductor spacing of 750mm, ruling span length of 60m and initial cable tension of 25% of the UTS of the conductor. The influence of inductance variations for fault current below 4kA is negligibly small for this specific configuration.

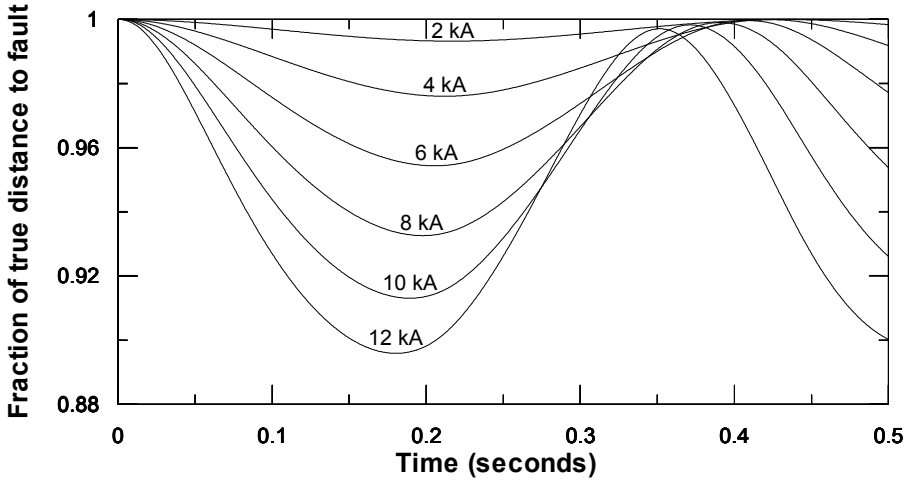

Figure 4.6: Accuracy of fault locator for various fault currents;
Conductor type: Grape; Conductor tension: 25% of UTS;
Span Length = 60m

Influence of the initial tension on the accuracy of the fault locator

The cable tension consists of the initial cable tension due to gravitation as well as the added tension due to the displacement of the conductor. The solution to Equation (4.7) will be inversely proportional to the initial cable tension *H*. Figure 4.7 indicates the influence of different initial cable tensions on the accuracy of an impedance type fault locator. The simulation was done for Grape conductor parameters with a conductor spacing of 750mm, fault current of 8kA and ruling span length of 60m. The ultimate tensile strength of a Grape conductor is 63.7kN. The maximum initial tension of the cable may not be larger than 32kN (50% of UTS). The initial cable tension does not have any major influence on the results within the first 100ms. There will be a significant increase in the error for low tensioned lines with a long relay operation time.

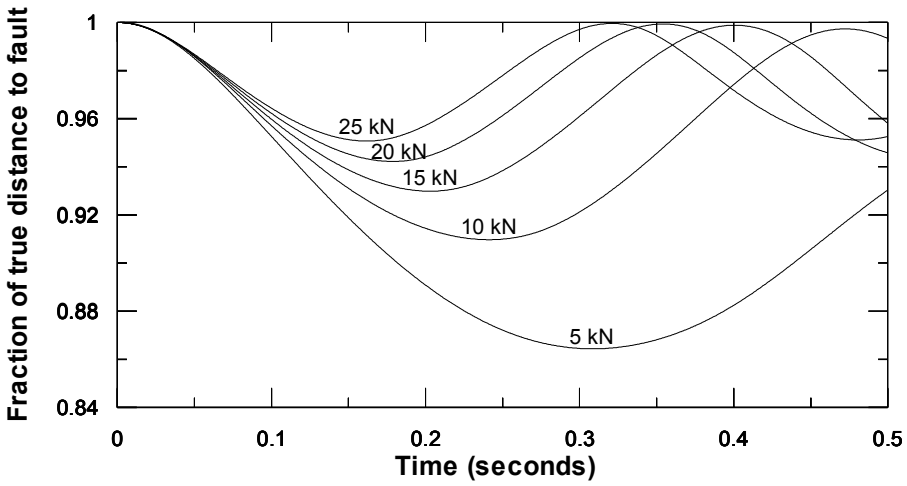

Figure 4.7: Accuracy of fault locator for various initial conductor tensions; Conductor type: Grape; Span Length = 60m, Fault current = 8kA

4.4 Discussion

The finite element simulation model showed that the deflection of conductors under a phase-to-phase fault might cause significant errors in the fault locator. The most important parameters influencing this error are conductor spacing, conductor tensioning, span length and fault current. Medium voltage distribution lines are typical lines that are at risk. The simulations show that an error in the distance estimation of up to 15% can be expected from fault locators on a distribution line due to the cable deflection under fault conditions. The error is also highly dependent on

time. The time required by the relay to converge and check for stability is critical to reduce the possible fault.

This phenomenon can easily cause false trips for faults close to the boundaries of the zones. A fault can initially be correctly identified to be outside the protection zone. Circuit breakers on MV networks can take up to 500ms to clear a fault. In that period, the distance estimation can be reduced by 10-15% due to conductor displacement by magnetic forces on the conductor. The fault will therefore be wrongly identified by the fault locator relay after 100-200ms to be within the protection zone and will cause the feeder to trip.

Fault levels on distribution systems have large fault levels near to the transformers. The fault level at the end of the line will be much smaller due to the high line impedance. Estimation errors as a percentage of the true distance to fault for close in faults will be much bigger than for faults at the end of the line due to magnetic forces. However, the error in the actual distance will be small for close in faults due to the overall small distance to the fault.

The simulations did not include asymmetric fault currents. Only symmetrical fault currents were used for the evaluation of the displacement of the conductors under fault conditions. The peak amplitude of the fault current at fault inception can be up to twice the steady state fault current. This is influenced by the X/R ratio and the vector position of the current at fault inception. The X/R ratio will also determine dc-offset decay time. This initial dc offset will further increase the speed and amplitude of the conductor deflection as described by the simplified Equation (4.7). The asymmetry of the fault current will therefore have a further negative effect on the accuracy of a fault locator algorithm.

The Australian Standards on high voltage switchgear [67] defines three X/R decay curves. “Curve (iii)” [67] should be used for close-in faults where the X/R ratio is determined by the transformer. It is shown in [67] that the dc-offset current would have only decay to 50% of its original value after 90ms. “Curve (ii)” should be used where transmission lines dominates the source impedance. It is shown in [67] that the dc-offset current for “Curve (ii)” will reach 40% of its original value after 90ms.

The dc-offset will influence the results of both close-in faults and faults far out on the line. The exact influence of the fault current on the maximum amplitude of the conductor displacement is however highly variable as the exact current vector position at fault inception is unknown.

Ideally it should be possible to estimate the possible error and make positive corrections to the relay output. All the parameters influencing the amplitude are constant or known except the initial cable tension, which is highly variable and influenced by factors such as ambient temperature, wind and load current. Figure 4.7 show that the cable tension will have a minor role in the accuracy of the first 100ms of the fault. However, it has a major role in the amplitude and response time of the conductor displacement after this. It is therefore impossible to try to estimate the possible error due to the conductor displacement.

4.5 Conclusion

A simple model was introduced to evaluate the dynamic behaviour of overhead lines under external forces. This model is based on existing equations and methods for cable design with a slight variation in the calculation of additional tension as well as the introduction of magnetic forces in the wave equations. The model was used to determine the dynamic behaviour of a conductor under a phase-to-phase fault condition and compared against available experimental data. It will be easy to calculate the dynamic behaviour of a conductor with additional loads such as wind load and dampers. This model can also be used in the evaluation of dynamic forces on the poles due to a variation on wind loads or magnetic forces caused by faulted conditions.

The simulation results show that the displacement of a conductor during fault conditions could cause error as large as 15% on small, poorly tensioned 3.3kV and 11kV lines. This should, however, not be a major problem for high voltage distribution and transmission lines due to the large spacings between the conductors. These lines have however much higher fault levels that can cause some negative influence on the accuracies of fault locator algorithms. These under estimation of

distance to faults can cause false trips of feeders due to faults outside the relay protection zone.

5 DETECTION OF A BREAKING CONDUCTOR

There exists no secure method in the detection of downed conductors [4]. The methods that are used as well as new proposals are all aimed at the detection of arcing to ground. Since an arc is not always present on a high impedance fault, these algorithms fails to detect high impedance faults on materials such as dry asphalt. Another method [38] that is currently being tested is by using remote units along a distribution line to detect phase failures. A remote unit via a dedicated communication line alerts the master unit at the feeder should a phase failure be detected. The dedicated communication line makes this option expensive and only viable on short lines.

In this section, a novel idea is explored in detecting a downed conductor. The focus shifts from detecting the arc between the conductor and ground to identifying the arc cause by conductor separation. The unique characteristics of such an arc will be used to identify a breaking conductor. These characteristics were estimated using the dynamic characteristics of a broken conductor.

5.1 Theory of dynamic behaviour of breaking conductors

Most of the recent work done [68] on the dynamic behaviour of cables is based on highly extensible cables. These works are based on numerical modelling of dynamic phenomena such as wave movement and breaking of extensible cables. This excludes steel, copper or Aluminium Conductor Steel Reinforced Cable (ACSR) that are normally used in overhead line designs.

Gravitation and elastic forces will tend to cause the broken ends of the conductor to accelerate away from each other when the conductor breaks. Gravitation will cause the conductor to “swing” downwards and the elastic force will cause the conductor to retract. This retraction will accelerate the conductor ends to a constant speed.

Gravitational force is the weakest of the four existing forces in nature and might be negligible in this investigation. The acceleration of the cable due to pure gravitation

will be compare to the acceleration of the conductor end due to elasticity. No dependencies will be assumed between the acceleration caused by gravitation and due to elasticity. The effects of gravity can be ignored if the acceleration of the broken end due to elasticity is much larger than that caused by gravity.

A failure in the middle of the span will be evaluated here as a base case. It must be mentioned that the following mathematical model is only an approximation of the dynamic behaviour of the conductor. There is however no use in using an absolute accurate dynamic model for conductor separation due to the approximations of the arc properties.

The derivation of the acceleration of the broken end is shown in Appendix II. This Appendix covers the derivation for acceleration due to gravitational forces (Equation (5.4)) as well as elastic forces (Equation (5.8) and (5.9)).

5.1.1 Displacement caused by gravitational forces

Equation (5.1) describes the sag of a conductor with mass per unit length of ρ and cable tension H. This equation was derived from the standard parabolic approximation for sag calculations [65]. The origin of the co-ordinate system is selected to be on one of the fixed points of the line. It is further assumed that two fixed points of the conductor is on the same height. X is the centre of the conductor span. The length of the conductor is approximated by Equation (5.2) [65].

$$f(X,H)=\frac{\rho}{2H}x^2-\frac{X\rho}{H}x \tag{5.1}$$

$$L\approx x\left(1+\frac{x^2\rho^2}{6H^2}\right) \tag{5.2}$$

$$f(X)=-\sqrt{\frac{3}{2}X(L-X)} \tag{5.3}$$

Equation (5.3) gives the maximum sag as a function of the conductor length and position of the centre of the span. This equation is obtained by substituting Equation (5.2) into Equation (5.1).

It is also assumed that the conductor is horizontal at the midpoint. Once it failed, gravitation will be the only vertical force on the end. For the first few meters of movement, the failed end of the line will stay horizontal. The end of the failed line will thus follow the locus of Equation (5.3) in order for it to stay horizontal. The variable X would decrease from its original value of X_0.

The vertical acceleration of the conductor must be equal to the gravitational acceleration since no other vertical force exists on the end of the conductor. Therefore, the second derivative of Equation (5.3) must therefore be equal to the gravitation constant g. Equation (5.4) shows the solution for X of this deferential equation will describe the horizontal displacement of the failed end point of the conductor as a function of the original sag D_0, time t, gravitational acceleration g and conductor length L.

$$X(t) = \frac{1}{2}\left(L + \sqrt{L^2 - \frac{2}{3}g^2t^4 - \frac{8}{3}gt^2D_0 - \frac{8}{3}D_0} \right) \tag{5.4}$$

5.1.2 Displacement caused by conductor retraction

The horizontal displacement due to retraction of the two ends of a broken conductor is assumed to be independent of gravitational movement. The use of energy conservation equations is a simple method used to calculate the displacement of a mass under the influence of an ideal spring. This same principle will be use in the calculation of the displacement of the failed end due to elasticity. Equation (5.5) describes the energy balance of a cable that is stretched $\Delta\ell$ meters whereas the variables used in Equation (5.5) are defined by Figure 5.1. Equation (5.5) states that the total potential elastic energy before the break in the conductor is equal to the potential elastic energy after the break plus the summation of the kinetic energy of all n individual element Δx_i as defined by Figure 5.1.

The retraction speed of highly extendable cable is governed by the speed of wave propagation [62] in the cable. This speed gives an indication of the rate of dynamic

change in the forces in the conductor. After the failure of the conductor, the force at the break point becomes zero whereas the tension in the rest of the cable is still the same as before the failure. The tension in the length of the cable will decrease to zero at the same rate as the speed of propagation of a wave in the cable. This propagation will start at the point of failure.

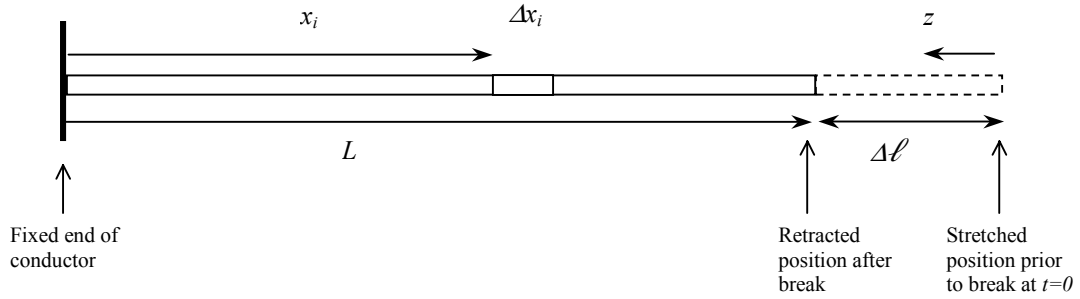

Figure 5.1: Definition of variables for a typical stretched conductor during retraction.

(Equation 5.5)

$$\frac{1}{2}k(\Delta\ell)^2 = \frac{1}{2}k(\Delta\ell - z)^2 + \sum_{i=0}^{n}\frac{1}{2}(\Delta x_i \rho)\left(\frac{dx_i}{dt}\right)^2 \tag{5.5}$$

Equation (5.6) describes the wave propagation speed in a cable with a constant Youngs modulus normally associated with steel cable [68]. The speed of wave propagation in steel cable is $2\text{x}10^6$ m/s, which is a relativistic speed that is much faster than the likely speed of retraction of the cable. The tension in the cable will reduce to zero over a very short period. It can therefore be assumed that the retraction speed of each element i of length Δx_i is directly proportional to the specific element's distance from the fixed point. By using this relationship, the speed of the conductor's broken end can be calculated as a function of the total retraction distance (z) at time t.

$$c_e = \sqrt{\frac{EA}{\rho}} \tag{5.6}$$

$$v_z = \sqrt{\frac{3EA}{L^2\rho}\left(\frac{2HL}{AE}z - z^2\right)} \tag{5.7}$$

$$v_{z_{MAX}} = \sqrt{\frac{3}{\rho EA}} \cdot H \tag{5.8}$$

Equation (5.7) only applies while $z \leq \Delta\ell$. The line end will undergo no more acceleration once the displacement of the broken end is bigger than the original elastic stretching. The stiffness forces will have no influence on the speed of the cable because of the small displacement under investigation in comparison to the total length of the cable. It can therefore be concluded that the two ends will depart from each other at a constant speed. The final speed due to elastic contraction is given by Equation (5.8).

Note that this final speed is independent of the span length of the line. The only variable that can influence the final separation speed is the conductor tension. This initial conductor tension has lower limits to prevent it from encroaching into the minimum clearance distance to ground and some maximum limits that is govern by safety standards and the UTS of the conductor. The final separation speed of a broken conductor due to elastic forces will therefore have very specific top and bottom speed limit. This speed will also be totally independent of the position of failure relative to the span.

It is further possible to calculate the time required to reach this maximum speed by integrating Equation (5.7) over time for a distance of $\Delta\ell$. The full derivation of Equation (5.9) is given in Appendix II. The expression shown in Equation (5.9) shows the relationship between the time to reach maximum speed t_M and the line parameters E, A, ρ and L. The ratio of the cross sectional area of the conductor A to the mass per unit length ρ as well as the Youngs Modulus E should be constant for homogeneous conductors. This ratio and Youngs Modulus should also not vary too much for non-homogeneous conductors such as ACSR conductors. The time required to reach this maximum speed is therefore a strong function of the span length and type of conductor.

$$t_M = \frac{\pi L}{2} \cdot \sqrt{\frac{\rho}{3EA}} \tag{5.9}$$

5.2 Evaluation of dynamic behaviour of breaking conductors

The elastic forces will cause an initial acceleration of the broken end. After this initial acceleration, the ends will separate at a constant velocity. Gravity will cause an increasing acceleration until the conductor reaches the ground. In this section, the influence of the two different causes of displacement will be discussed. The aim will be to determine if one of the two causes of conductor separation is dominant so that the non-dominant force can be ignored.

For this purpose, data of typical conductors used on medium voltage systems will be used (Table 4.1). The displacement of the conductor end can be calculated by using Equation (5.4) and the integral of Equation (5.7). The type of insulator used will have some influence on the displacement of the conductor. Pin, post and standoff insulators are all fixed insulators. No freedom of movement exists as in string insulators. The span length of the overhead line can be used as conductor length in Equation (5.7). Conductor failure on an overhead line with string insulators will be more complex. The influence of string insulators will be discussed later.

The actual tension, H, of the cable depends on the design and environmental conditions. British Standards requires that a safety factor of 2 be used for the design of an overhead line [69] as this loading condition will prevail under the worst possible environmental conditions. A typical overhead line design must make provision for a maximum wind force of 383Pa [69]. Because the overall diameter for an Apple conductor is 9.00mm, allowance must be made for a horizontal force of 3.5N/m. If one takes into account that gravitation will cause a vertical force of 1.71N/m on the conductor and the vector sum of the two forces is 3.9N/m, then the weight will be accountable for approximately 40% of the total maximum allowable tension in the cable. Near perfect conditions will be assumed for the purpose of this study. A tension of 50% of the maximum allowable design tension will be used. The value for the tension, H, in Equation (5.8) will be 25% of the ultimate tensile strength of the cable. This will be the most difficult condition to detect, since it will cause the lowest acceleration of the cable after failure. Typical displacement values of the end of the conductor are shown in Table 5.1. These displacement values were

calculated using Equation (5.8) and data in Table 4.1. Incident values where calculated up to 80ms after the instance of conductor failure.

Table 5.1: Comparison of gravitation and elastic displacement 80ms after conductor failure. It is assumed that the initial tension of the conductor is 25% of the UTS of the specific conductor.

Conductor Type:	*Apple*		*Grape*		*Paw-Paw*	
Spanlength (m)	60	120	60	120	60	120
Mid-span break – gravitation displacement	0	0	0	0	0	0
Endpoint break gravitation displacement (mm)	31.4	31.4	31.4	31.4	31.4	31.4
Mid-span break-elastic displacement (mm)	1238	1181	1339	1278	1130	1079
Speed after initial acceleration (m/s)	7.5	7.5	8.1	8.1	6.85	6.85
Time to reach maximum speed due to elasticity (ms)	4.4	8.6	4.4	8.6	4.4	8.6

Table 5.1 shows that the conductor separation will be dominated by the broken end separation due to elastic forces. The influence of the gravitational force on the displacement within the first 80ms is negligible. The horizontal velocity of the conductor end is constant after the original acceleration and it is expected that the velocity of the conductor will be approximately constant until arc extinction. The time required to reach maximum speed due to elastic forces is identical for all three types of ACSR conductor. Table 5.1 shows that the time required to reach the maximum speed are dependent on the length of the broken conductor. Note that the given values in Table 5.1 are relative to a fixed position. The displacements and speeds relative to the other end of the broken conductor are double the values shown in Table 5.1.

The data in Table 5.1 assumes that fixed type insulators are used. An increased effective conductor length is used for overhead lines constructed with strings of insulators. The effective conductor length is equal to the distance from the point of failure to the nearest strain tower at the instant of conductor failure. This length will reduce to the span length as the tension in the cable is increased. This increase in cable tension is caused by the reduction in the freedom of insulator movement due to the contraction of the cable. The displacement curve will be identical to that of a fixed type insulator once this state is reached. A length of 146mm is a typical length

of a string insulator on an 11kV line [70]. The effective conductor length is reduced to the length between the broken end and nearest pole once the total horizontal displacement is equal to 146mm. The same linear displacement will be present after the initial freedom of the string insulator is eliminated.

It can be concluded that gravitation can be ignored in the initial acceleration of the broken ends of a conductor. The conductor will have an initial acceleration after conductor failure. The two endpoints of the conductor will separate at a constant velocity once the initial acceleration period has passed. These conditions will be independent of the type of insulator used on the overhead line. This high-speed constant arc length increase is a unique feature on power systems and can be used for conductor failure identification.

5.3 Modelling a mechanical failure of a conductor in a network

In this work, distribution lines are the main area of concern regarding a downed conductor. The area of research concentrates on radial feed systems because the majority of distribution lines fall in this category. Figure 5.2 indicates a typical single line diagram of a radial feed system and will be used as the base case for simulation studies.

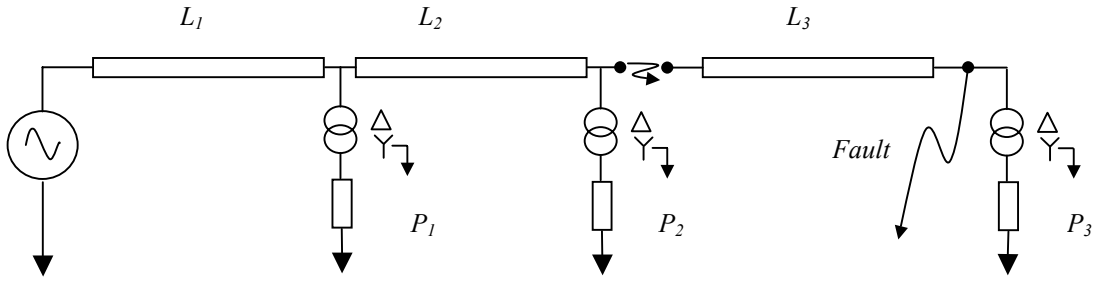

Figure 5.2: Single line diagram for simulation tests *5.1-5.18*

The failure of a conductor can either be under normal operating conditions or faulted conditions. Two arcs will be in series if the conductor failed mechanically during an arc fault condition. The simulation of two Mayr modelled arcs in series caused an unstable system. A square wave was used as an approximation to the arc voltage at

the point of fault. Table 3.1 specifies the network parameter data that was used for the simulations.

5.4 Identification of a breaking conductor using arc voltage

The question arises as to whether it is possible to identify a failed conductor from the dynamic properties of the estimated fault arc voltage. Radojevic *et. al.* [6] developed an algorithm to estimate the arc voltage and distance to fault. The authors originally proposed that the estimate arc voltage should be used to make a more informed decision on the automatic re-close of a feeder after a fault. Faults due to conductor touching results in low arc voltages whereas insulator flashover results in a temporally arc voltage. This algorithm can also be used to estimate the arc voltage on a seemingly healthy circuit.

The speed of the conductor separation can be used as the unique feature of a conductor failure. Stokes empirical equation (Table 2.2) will be used in calculating the theoretical relationship between the arc voltage gradient and conductor separation speed. Stoke's original empirical equation calculates the arc power as a function of the arc length and current. The equation was re-formulated in Table 2.2 to estimate the arc voltage as a function of arc length and current.

Radojevic's differential equation method [6] can be used to calculate the amplitude of the arc voltage using measured values of voltage and current at the supply-end of the feeder. The actual value obtained is the RMS value of the arc voltage since the least square method is used. The RMS value is equal to the amplitude of a square wave. It is accepted that the change in the RMS current during the fault condition will be negligibly small because the arc voltage across the arc will be small comparing with the supply voltage. Stokes' empirical equation is therefore differentiated to produce Equation (5.10). This equation will be used to estimate the separation speed of a broken conductor.

$$\frac{dz_g}{dt} = \frac{1}{0.53(I_{RMS})^{0.12}} \frac{dV_a}{dt} \tag{5.10}$$

5.4.1 Arc current, separation speed and arc voltage gradients

In the previous section, it was proposed that Radojevic's algorithm be used for the arc voltage estimation. In this section, the influence of arc current and separation speed on the estimated arc voltage will be investigated. It will be shown that the estimated arc voltage can be used to detect a breaking conductor.

In theory the arc voltage should increase proportional with the current (Table 2.2), although Radojevic's algorithm assumed a constant arc voltage for the duration of the data window. This will be untrue as a rapidly increased arc voltage is expected as the gap between the two broken ends increase. Radojevic's differential Equation (2.4) was modified to cater for this rapid but linear arc voltage amplitude increase. Equation (5.11) presents an extra term representing the linear arc voltage increase where m is the average arc voltage amplitude increase and T is the sampling period between two consecutive samples. It is important that the sample number k must start at zero at the beginning of the data window. The unknown values for the arc voltage (U_a) and gradient (m) is estimated using the least square method.

$$u_k = \left\{ r i_k + \frac{x}{2T\omega_0} \left[i_{k+1} - i_{k-1} + K_L \left(i_{0(k+1)} - i_{0(k-1)} \right) \right] \right\} \ell + \operatorname{sgn}(i_{0k}) U_a + \operatorname{sgn}(i_{0k}) kTm + i_{0k} R_e + \varepsilon_k \tag{5.11}$$

Simulations 5.1, *5.2* and *5.3* were executed to compare the accuracy of the Radojevic's differential equation algorithm with the modified algorithm shown as Equation (5.11). Details of these simulations are shown in Table 5.3.

The gradient of both the true arc voltage and Radojevic's estimated arc voltages was calculated over the full 0.05 seconds period that the arc was present. The least square method was used to calculate the best fit for a straight line. The modified algorithm estimates the gradient automatically. The average value of the last 100 estimated gradients was used in the statistical analysis. The estimated conductor separation speed was normalised with the true separation speed.

Table 5.3: Details of simulations used to compare the accuracy of Radojevic's algorithm with the modified algorithm.
Details on P_1, P_2, P_3, L_1, L_2 and L_3 are shown in Figure 5.2. (refer to Equation (5.11))

	Simulation 5.1	*Simulation 5.2*	*Simulation 5.3*
Circuit Parameters	Table 3.1	Table 3.1	Table 3.1
Fault Arc model	None	None	None
Conductor separation arc model	Mayr model	Mayr model	Mayr model
Conductor Separation	Constant speed of 10m/s	Constant speed of 20m/s	Constant speed of 40m/s
Conductor Type	N/A	N/A	N/A
Ruling Span length	N/A	N/A	N/A
Load Conditions	P1: 0kW	P1: 0kW	P1: 0kW
(Using a 0.96 power factor)	P2: 0kW	P2: 0kW	P2: 0kW
	P3: Varied	P3: Varied	P3: Varied
Line Lengths	L1: 2km	L1: 2km	L1: 2km
	L2: 2km	L2: 2km	L2: 2km
	L3: 2km	L3: 2km	L3: 2km
Time of fault inception	N/A	N/A	N/A
Time of conductor failure	0.03s	0.03s	0.03s
Time of arc extinction	0.08s	0.08s	0.08s

The normalised conductor separation speed based on the true arc voltage was 0.996p.u. with a standard deviation of 1.51%. Figure 5.3 indicates the results of *simulation 5.1-5.3* that were obtained for both Radojevic's differential equation as well as the modified algorithm. The accuracy of the algorithm proposed by Radojevic tends to decrease with an increase in arc currents. Radojevic's algorithm gave a 0.973p.u. average normalised speed with a standard deviation of 37.4%. The modified equation with the linearly increasing voltage term gave values that are more acceptable. The average normalised conductor separation speed was 1.04p.u. with a standard deviation of only 6.9%. The decrease in the normalised speed at high currents is less notable for this modified algorithm.

These simulations indicate that the modified differential equation algorithm will produce more accurate estimations of the conductor separation speed. The smaller standard deviation obtained by the modified algorithm indicates results that are more reliable. It shows that the modified algorithm is more suitable for arc voltage gradient calculations than the originally algorithm.

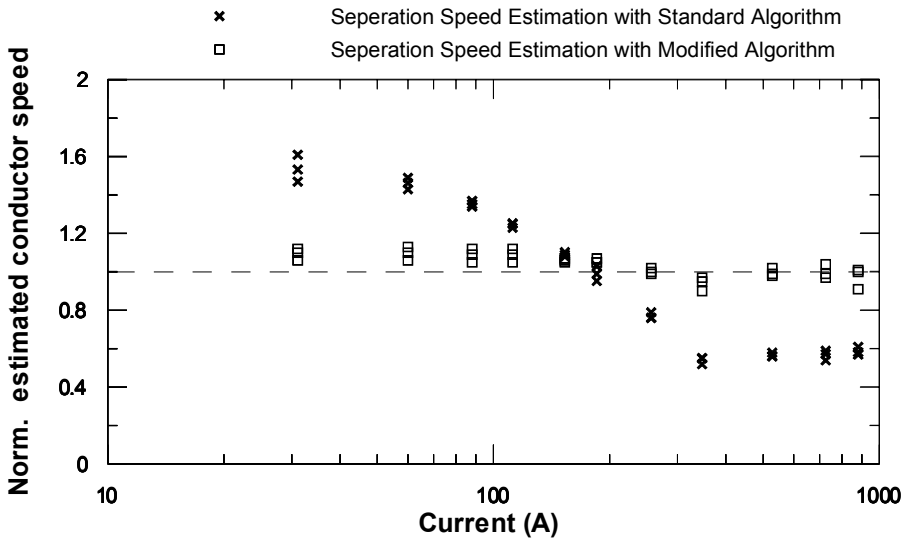

Figure 5.3: Normalised estimated conductor separation speed vs. current for the modified algorithm. Results are shown for 10, 20 and 40m/s but are not significantly different as shown on graph.

5.4.2 Guarding against transients

A fault on the network can also produce an arc. The algorithm will produce faulty data during the initial stages of the fault due to the transients. The linearity of the arc voltage increase is the unique property of a breaking conductor. False trips due to transients can be prevented if the linearity of the voltage amplitude is checked. The correlation coefficient is proposed to eliminate false trips due to transients. The correlation coefficient is positive or negative according as to whether the arc voltage tends to increase or decrease for time over time. The closer this coefficient is to 1, the stronger the linear relationship between the estimated arc length and time. The final borders of the correlation coefficient must be obtained using experimental data. A minimum limit of 0.8 was set for this theoretical study.

5.4.3 Development and testing of arc voltage algorithm on a simulated network

The previous section investigated the relationship between the estimated arc voltage gradient and the conductor separation speed of a broken conductor. The simulations indicated that it is possible to derive a secure algorithm to detect a conductor failure. The following algorithm is proposed for conductor failure detection:

(a) Filter out all high frequencies (>700Hz) of both the current and voltage signals.

(b) Calculate arc voltage using Radojevic's standard differential equation algorithm.

(c) The true arc current should be calculated once an arc voltage is detected. The post fault current must be subtracted from the current during the fault.

(d) The true arc voltage gradient can be calculated using the modified algorithm.

(e) Calculate the actual conductor separation speed.

(g) The feeder must be tripped if the estimated speed is greater than a pre-set value for specific time duration and the correlation coefficient of the estimated arc voltage is greater than 0.8. A typical speed set point should be 5m/s but should be govern by the construction of the overhead line..

The arc voltage output of Radojevic's algorithm converges faster to a steady increase than the modified algorithm. Only the shape is required to secure the algorithm using the correlation coefficient. Radojevic's algorithm is used to increase the time to identify the steady arc voltage increase.

Table 5.4: Simulation used to test the proposed algorithm to detect a breaking conductor. The initial tension is 25% of the UTS. Details on P_1, P_2, P_3, L_1, L_2 and L_3 are shown in Figure 5.2.

	Sim 5.4	*Sim. 5.5*	*Sim. 5.6*
Circuit Parameters	Table 3.1	Table 3.1	Table 3.1
Fault Arc model	None	None	±500V square
Conductor separation arc model	Myar model	Myar model	Myar model
Conductor Separation	Equation (5.7)	Equation (5.7)	Equation (5.7)
Conductor Type	Banana	Banana	Banana
Ruling Span length	100m	100m	100m
Load Conditions	P1: 0kW	P1: 600kW	P1: 600kW
	P2: 0kW	P2: 600kW	P2: 600kW
	P3: 600kW	P3: 600kW	P3: 600kW
Line Lengths	L1: 2km	L1: 2km	L1: 2km
	L2: 2km	L2: 2km	L2: 2km
	L3: 2km	L3: 2km	L3: 2km
Time of fault inception	N/A	N/A	0.02s
Time of conductor failure	0.08s	0.08s	0.08s
Time of arc extinction	0.15s	0.15s	0.15s

A fault on a system with a Banana conductor was simulated for different scenarios as detailed in Table 5.4. *Simulation 5.4; 5.5* and *5.6* were executed to determine the effectiveness of the proposed algorithm under different conditions.

The proposed algorithm was applied to the current and voltage waveforms that were produced by the simulations as detailed in Table 5.4. The results of the algorithm are shown in Table 5.5. It shows that the algorithm is able to successfully detect a broken conductor even during a fault condition as simulated by *Simulation 5.6*.

Table 5.5: Results for the proposed algorithm to detect a broken conductor. Algorithm applied on voltage and current waveforms obtained from simulation results (Table 5.4).Note that the true conductor separation speed is 14.4m/s.

	Sim. 5.4			*Sim 5.5*			*Sim 5.6*		
Time (ms)	V_g *(m/s)*	*r (p.u.)*	*Trip signal*	V_g *(m/s)*	*r (p.u.)*	*Trip signal*	V_g *(m/s)*	*r (p.u.)*	*Trip signal*
60	0	0.10	0	0.2	0.05	0	9.1	0.31	0
70	0	0.19	0	0	0.07	0	60.6	-0.30	0
80	0.1	-0.6	0	0	-0.1	0	32.0	-0.23	0
90	0.1	0.10	0	0.2	0.39	0	50.4	0.16	0
100	3.7	0.64	0	5.1	0.67	0	13.5	0.48	0
110	11.5	0.82	1	12.6	0.84	1	11.7	0.79	0
120	15.3	0.92	1	14.8	0.93	1	21.0	0.79	0
130	15.4	0.97	1	14.1	0.98	1	19.4	0.97	1
140	14.5	0.99	1	14.0	0.99	1	20.0	0.99	1
150	14.6	0.99	1	14.1	0.85	1	19.7	0.97	1
160	17.5	0.70	0	8.3	0.68	0	6.6	0.66	0
170	71.8	0.50	0	26.9	0.38	0	-3.8	-0.38	0
180	254	0.72	0	17.0	-0.01	0	-3.1	-0.71	0
190	326	0.37	0	3.9	-0.46	0	6.9	-0.67	0

The separation starts at 80ms and arc extinction is at 150ms. The algorithm requires 30ms to converge. *Simulation* 5.6 represents a conductor failure during an earth fault. The transients cause an extra 20ms before the algorithm could converge. The last 50ms estimated arc voltage signal is used to calculate the correlation factor. It is possible to increase the response time by reducing the data window for the correlation factor calculations. The algorithm would not have been able to identify the fault if the conductor failed within the first 10ms after the fault inception. The calculated speed after fault inception is within the trip zone but the correlation factor prevents a false trip.

The estimated separation speeds are very accurate for *Simulation 5.4* and *5.5*. The true separation speed is 14.4m/s in comparison with the estimated values between 14m/s and 15m/s. A poor result on the separation speed estimation was obtained from *Simulation 5.6*. The error is caused by the automatic subtraction of the post fault current. An earth fault or phase-to-phase fault will cause a collapse of the phase voltage. The actual load current to the healthy parts of the circuit is therefore

reduced dramatically due to the voltage collapse. The voltage and current to the healthy parts would return to the normal values after the fault. The estimated arc current during the faulted condition will therefore be smaller than the true arc current which will cause the algorithm to over estimate the actual arc voltage. The algorithm has provided correct speed estimations when the true measured current be used. It is therefore proposed that the measured current be used under faulted conditions while the estimated current is used under normal operational conditions.

5.5 Identification of a breaking conductor using arc resistance variations

In the previous section, a conductor failure was identified using the estimated arc voltage amplitude gradient. The algorithm that was used is, however, slow to converge should a conductor failure happen coincidentally with a fault. A second method based on arc resistance variations is therefore proposed. The resistance of an arc is primarily dependent on the arc current and length and increases dramatically during the zero crossing of the current. An increase in the arc length would also cause an increase in the arc resistance. It is however impossible to calculate the arc resistance without knowing the line and load resistance as the model assumes all elements to be in series. The load resistance is also varying continuously. It is therefore clear that the average resistance will not be suitable in the detection of a downed conductor. The resistance variation of an arc during current zero periods is however unique. This variation can be used to estimate the arc length variation.

5.5.1 Resistance Estimation Algorithms

A time domain algorithm must be used for the estimation of the resistance as a frequency domain algorithm will not provide the high frequency change in arc resistance. Three time domain numerical methods exist for the estimation of the system resistances [23, 56]. These numerical algorithms were all derived from the same differential Equation (2.2). Tests indicated that all three algorithms produced

exactly identical results and any of the three algorithms can therefore be used for the calculation of the arc resistance.

The algorithm was derived using the assumption that the resistance is constant for the duration of the three-sample data window. The error of this assumption needs to be checked before using any of these algorithms. Figure 5.4 indicates the result of the algorithm versus the true arc resistance. The low pass filters cause the phase shift that is evident in Figure 5.4. An alternative algorithm (Equation (5.12)) is also presented, indicating a more accurate peak resistance. This algorithm assumed a constant change in arc resistance during the data window instead of a constant resistance. The solution of Equation (5.12) is also shown in Figure 5.4.

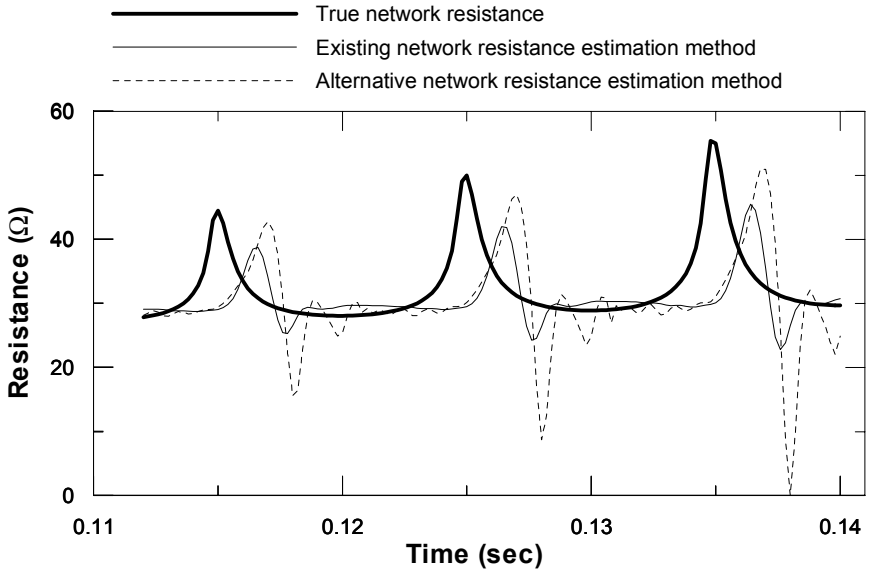

Figure 5.4: Estimated and true network resistance during breaking of a conductor. The circuit details are shown in Table 5.4 (*Simulation 5.4)*

$$\begin{bmatrix} v_k \\ v_{k+1} \\ v_{k+2} \end{bmatrix} = \begin{bmatrix} \frac{(i_{k+1} - i_{k-1})}{2T_s} & i_k & -T_s i_k \\ \frac{(i_{k+2} - i_k)}{2T_s} & i_{k+1} & 0 \\ \frac{(i_{k+3} - i_{k+1})}{2T_s} & i_{k+2} & +T_s i_{k+2} \end{bmatrix} \begin{bmatrix} L \\ R \\ m \end{bmatrix} \tag{5.12}$$

where

T_s sampling interval

L system inductance

R system resistance

m rate of change of the system resistance.

Equation (5.12) estimates the peak values during the current zero periods more accurately. The overall estimated resistance waveform is more distorted. It was later established that this distortion started influencing the results negatively at high currents. The existing algorithms were therefore the best alternative for resistance estimation.

The sampling frequency was increased to 50kHz and the low pass filter was removed. This was done to overcome the distortion. The result that was obtained with this system was the same. No real reason for the distortion of the resistance signal could be found during the investigation of resistance estimations.

5.5.2 Wavelet spectrum of the estimated network resistance

Figure 5.4 shows the increase in the resistance peaks as the arc length increases. The absolute values of the peaks are also influenced by the line and load resistivity. The resistance increases during the current zero period is however only dependant on the properties of the arc. The aim of this section is to determine a method to isolate the arc resistance peaks so that it can be used in estimating the speed of arc length increase.

Three options exist in the isolation of the resistance peaks during the current zero periods. The first option is to use a band filter; isolating the resistance variation during current zero periods from high frequency noise and low frequency load changes. The second option will be to use a windowed Fourier transformation to isolate a specific frequency sinusoidal component while the third option is using wavelet with a Kerr function that resembles the arc resistance variance as close as possible. The arc resistance variation does not only consist of a single frequency but rather a wide band of frequencies. To accommodate these frequencies the band filter will require a wide band. This will make it possible for results to be more easily affected by harmonics since a wide band filter is used. A windowed Fourier transformation will only allow a specific frequency pass. Wavelet transformation is

identical to a windowed Fourier transformation with the exception of the Kerr function. A windowed Fourier transformation uses a sinusoidal wave as the Kerr function while Wavelet transformations uses a variety of functions. The Fourier transformation identifies the specific harmonic present in the signal. A wavelet transformation will identify a specific signal that has the same properties as the Kerr function in the signal. A "Mother" wavelet with the same properties as the arc resistance variation will isolate the arc resistance variation from network resistance. A wavelet transformation will amplify a range of frequencies with a specific ratio making it ideal to isolate a specific signal.

Figure 5.5 shows a "Mexican hat" wavelet superimposes on the estimated arc resistance variation. The resistance was simulated using the circuit details as specified in Table 5.4 (*Simulation 5.4*). The "Mexican hat" Kerr function is a simple one-dimensional function. Figure 5.5 shows that this mother wavelet is ideal to isolate the resistance variations during the current zero periods.

Table 5.6 shows the details of the network simulations used to determine the effect on different wavelet levels. The aim of these simulations was to determine the best wavelet level to be used as filter in isolating the arc resistance variation during current zero periods. A sampling frequency of 5kHz is used in sampling the voltage and current waveforms. The results for these simulations are presented in Figure 5.6. It shows that the 3^{rd}, 4^{th} and 5^{th} level wavelet coefficients are a maximum during the current zero periods. The 5^{th} level wavelet coefficient will be used as it represents a lower frequency band than the 3^{rd} and 4^{th} level coefficient and is therefore less likely to be influenced by high frequency transients.

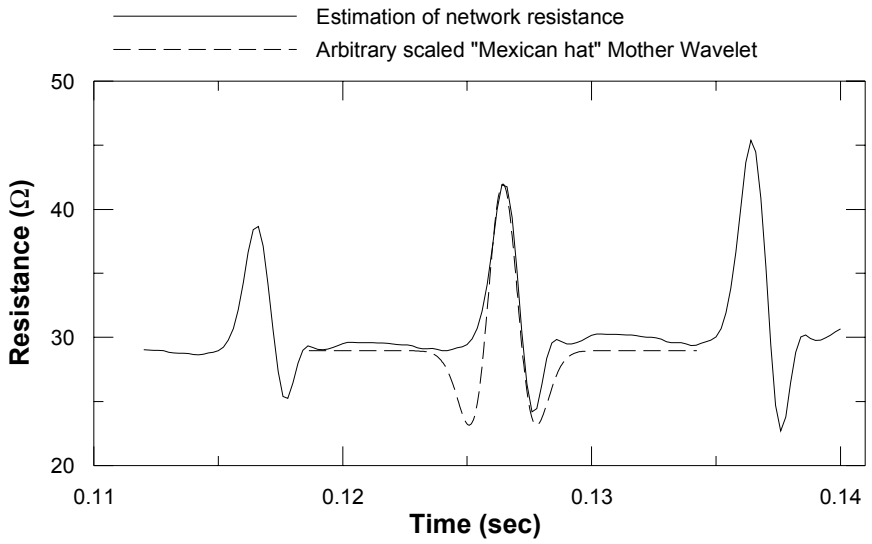

Figure 5.5: Arbitrarily scaled "Mexican hat" mother wavelet superimposed on a estimated network resistance during conductor failure.
Simulation data is in accordance with Table 5.4 (*Simulation 5.4*)

Table 5.6: Detail of simulation circuit to determine wavelet level spectrum of the network resistance during current zero periods. Details on P_1, P_2, P_3, L_1, L_2 and L_3 are shown in Figure 5.2.

	Sim 5.7	*Sim 5.8*	*Sim 5.9*
Circuit Parameters	Table 3.1	Table 3.1	Table 3.1
Fault Arc model	None	None	None
Conductor separation arc model	Meyr model	Meyr model	Meyr model
Conductor Separation	2000mm	500mm	500mm
Conductor Type	N/A	N/A	N/A
Load Conditions	P1: 0kW	P1: 0kW	P1: 0kW
	P2: 0kW	P2: 0kW	P2: 0kW
	P3: 4200kW	P3: 4200kW	P3: 4200kW
Line Lengths	L1: 2km	L1: 2km	L1: 2km
	L2: 2km	L2: 2km	L2: 8km
	L3: 2km	L3: 2km	L3: 8km
Time of fault inception	N/A	N/A	N/A
Time of conductor failure	N/A	N/A	N/A
Time of arc extinction	N/A	N/A	N/A

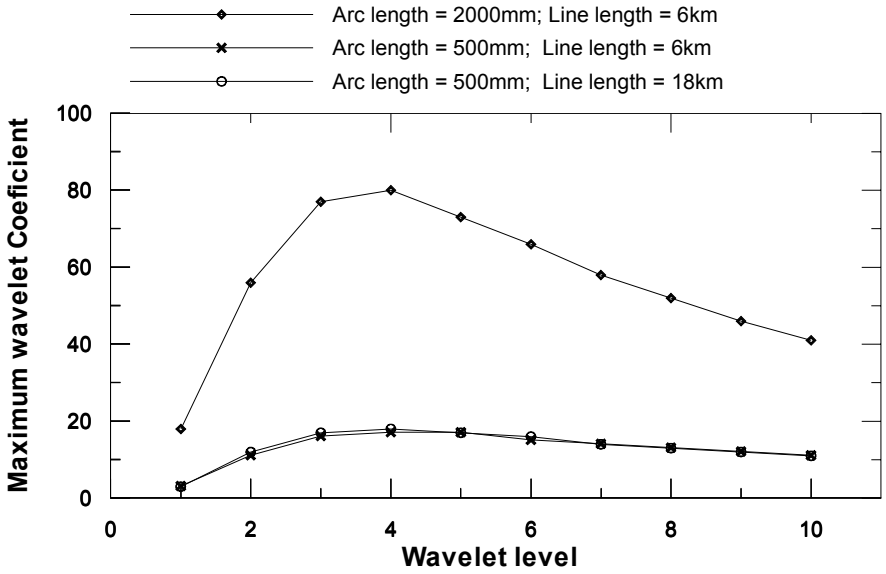

Figure 5.6: Maximum wavelet Coefficients for various wavelet levels of the estimated network resistance during current zero period for various arcs in a network described by Table 5.6.

5.5.3 Influence of a static arc on the wavelet coefficient

The arc resistance of the model used in the simulations is influenced by arc current and length. The arc resistance is proportional to the arc length while approximately inversely proportional to the arc current (Table 2.2). The influence of arc current, line length and arc length on the peak 5th level wavelet coefficient of the estimated network resistance during the current zero periods is unknown and will be explored in this section. Three sets of simulations were executed to determine the influences of the different parameters, varying one parameter while keeping the other parameters constant (Table 5.7).

The results of these simulations indicated that the fifth level wavelet coefficient is proportional to the arc length (Figure 5.7) and inversely proportional to the arc current (Figure 5.9). Figure 5.8 shows that the maximum fifth level wavelet coefficient is independent from the length of the line. An increase in the line length causes a decrease in the peak wavelet coefficient of the estimated network resistance, which is explained, by the increase in circuit inductance. As previously stated, the current and circuit inductance are responsible for the initial breakdown and arc ignition. The circuit inductance would help keep the arc resistance down during the

current zero periods. The overall influence of the inductance is relatively small. It will be assumed that this influence is negligible, but will be further investigated in the next paragraph. The exact relation of the arc length and arc current is estimated by Equation (5.13).

Table 5.7: Detail of simulations conducted to investigate the relationship of the estimated arc resistance peaks (wavelet coefficient), arc current, line length and arc length. Details on P_1, P_2, P_3, L_1, L_2 and L_3 are shown in Figure 5.2.

	Sim. 5.10	*Sim. 5.11*	*Sim. 5.12*
Circuit Parameters	Table 3.1	Table 3.1	Table 3.1
Fault Arc model	None	None	None
Conductor separation arc model	Mayr model	Mayr model	Mayr model
Conductor Separation	200mm to 2000mm	1000mm and 2000mm	1000mm and 2000mm
Load Conditions	P1: 0kW P2: 0kW P3: 600kW and 1200kW	P1: 0kW P2: 0kW P3: 1200kW	P1: 0kW P2: 0kW P3: 600kW to 4200kW
Line Lengths	L1: 2km L2: 2km L3: 2km	L1: 2km L2:2;4;8;16;32km L3:2;4;8;16;32km	L1: 2km L2: 2km L3: 2km
Time of fault inception	N/A	N/A	N/A
Time of conductor failure	N/A	N/A	N/A
Time of arc extinction	N/A	N/A	N/A

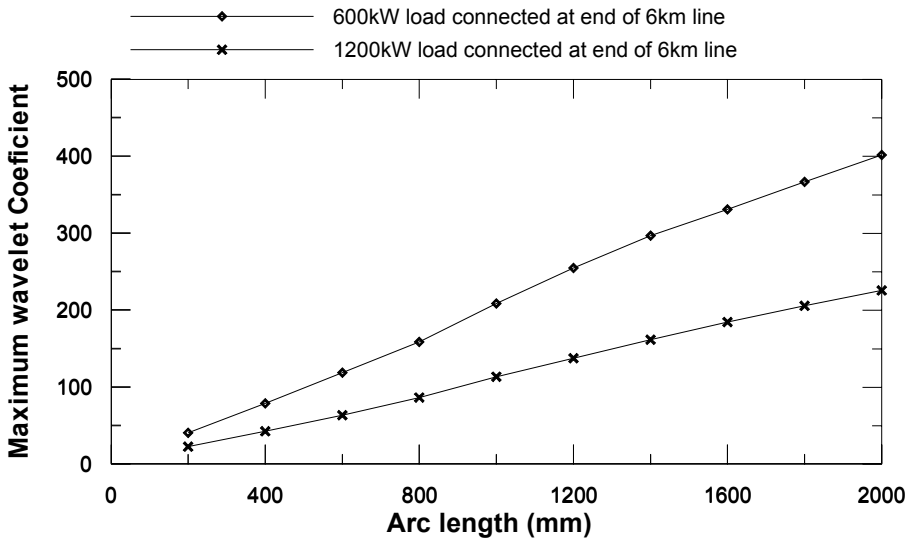

Figure 5.7: Influence of arc length on the peak wavelet coefficient of the estimated arc resistance. The circuit is specified by Table 5.7 (*Simulation 5.10*)

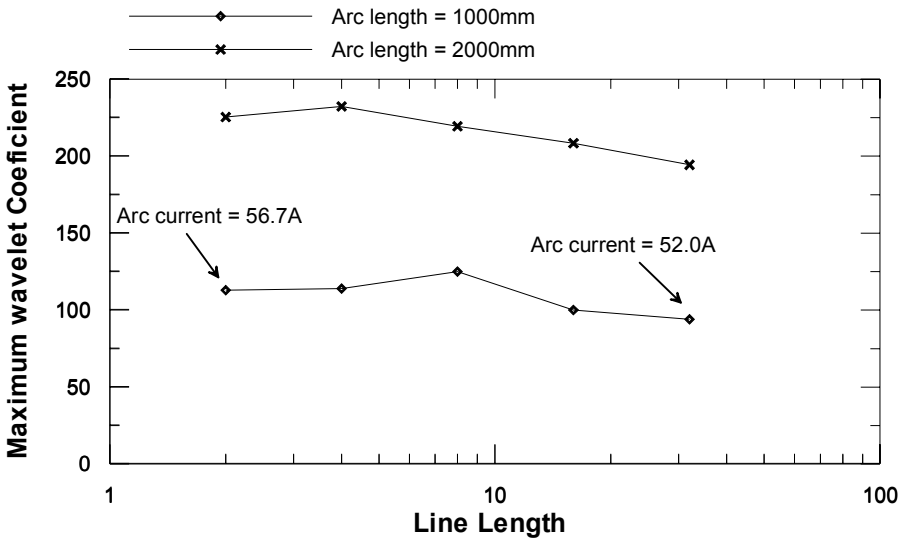

Figure 5.8: Influence of line length on the peak wavelet coefficient of the estimated arc resistance. The circuit is specified by Table 5.7 (*Simulation 5.11*)

$$z_g = \frac{(I_{arc})^x}{K_s} C_5 \tag{5.13}$$

In Equation (5.13), K_s is defined as the static constant, C_5 is the 5th level wavelet coefficient, I_{arc} is the RMS value of the arc current and z_g is the arc length. The static constant K_s is calculated for each plotted point in Figure 5.9 using Equation (5.13). The value of x, in Equation (5.13), is graphically estimated using MATLAB to give the smallest standard deviation as a percentage of the average value of all the estimated K_s values.

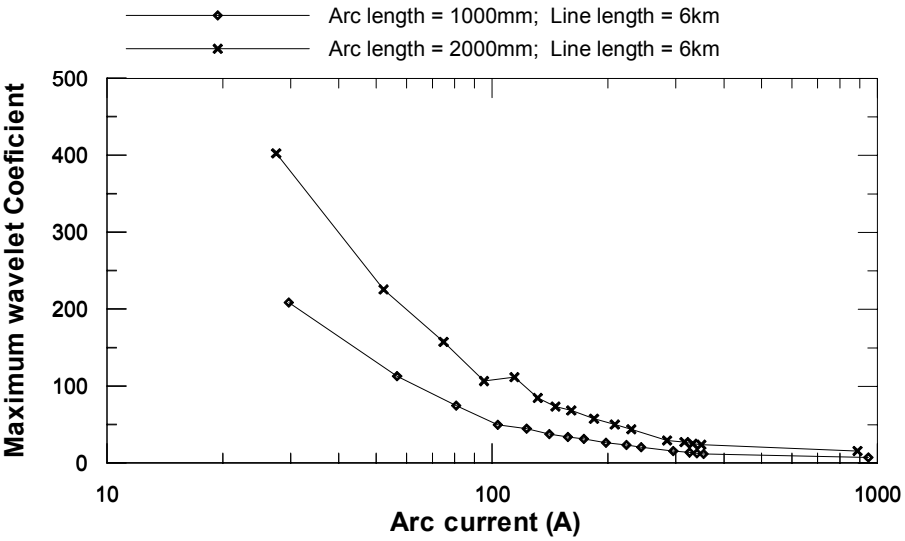

Figure 5.9: Influence of arc current on the peak wavelet coefficient of the estimated arc resistance. The circuit is specified by Table 5.7 (*Simulation 5.12*)

A standard deviation of 307 (8.7%) and mean of 3513 was calculated for an optimum x value of 0.9. Figure 5.10 give an indication of the distribution of estimated K_s values for the various data points presented in Figure 5.9.

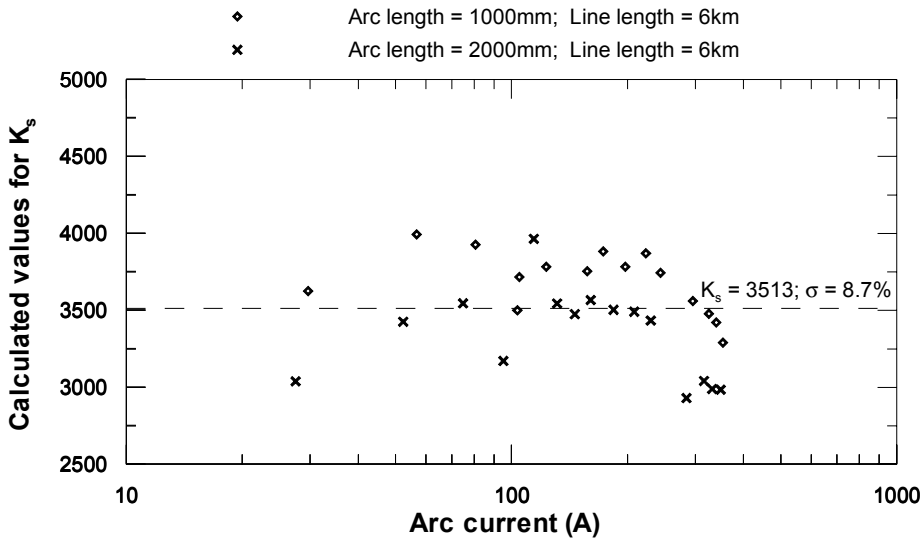

Figure 5.10: Calculated values of K_s vs. current for data points as shown in Figure 5.9. K_s is using Equation (5.11) with a x value that will produce a minimum standard deviation for the specific data set.

5.5.4 Influences of a dynamic arc length on the wavelet coefficient gradient

The relationship between the wavelet coefficient, arc current and arc length of a static arc was investigated in the previous section. It was shown that the arc length is proportional to the estimated network resistance wavelets coefficient. The same proportional relationship should exist between the conductor separation speed and the gradient of the maximums of the wavelet coefficient. The Mayr model explains the influence of the arc length and current variation on the arc resistance. The static arc resistance is a function of current and arc length (Table 2.2). The Mayr model implements a time delay in the variation of the arc resistance. The dynamic behaviour of the arc resistance would therefore be influenced by the rate of change (speed) of the arc length. Equation (5.13) was changed for this reason to Equation (5.14) to accommodate the rate of change in the arc length while the network induction is introduced as a third parameter in Equation (5.14). The influence of the

line length was tested in the previous section but ignored by Equation (5.13). It was speculated that the inductance of the line has an insignificant influence on the wavelet coefficient. The arc voltage should rise faster with a high inductance during the current zero periods causing a lower arc resistance.

$$\left(v_g\right)^y = \frac{\left(I_{arc}\right)^x X^z}{K_d} m_{c5} \tag{5.14}$$

where

K_d	Dynamic gradient constant
m_{c5}	Gradient of the maximum 5th level wavelet coefficients
v_g	Conductor separation speed
x, y, z	Unknown constants to be calculated.
X	Total inductance

The simulations that were conducted were aimed at proving the relation of Equation (5.14) and estimating values for the unknown constants x, y, z and K_d. The first set of simulations (Table 5.8 – *Simulation 5.13*) was used to investigate the influence of the separation speed on the wavelet coefficient. The load (current and impedance) was proved to be constant. The second set of tests was done, varying the load (including the inductance) with a constant conductor separation speed (Table 5.8 – *Simulation 5.14*). The gradient of both maximum wavelet coefficients of the estimated and true network resistance was calculated over the full 0.05 seconds period that the arc was present. The average gradient of the wavelet coefficient peaks was calculated using the least square method for curve fitting.

The results for *Simulation 5.13* (Table 5.8) are presented in Figure 5.11 as separation speed vs. the gradient of the peak wavelet coefficient. These results confirm a strong linearity between the conductor separation speed and the 5th level peak wavelet coefficient gradient of the network resistance. There is a slight non-linear increase of the coefficient at high currents indicating that the value of x in Equation (5.14) will be bigger than one.

Table 5.8: Circuit details of simulations done to test the influence of conductor separation speed on the wavelet coefficient.
Details on P_1, P_2, P_3, L_1, L_2 and L_3 are shown in Figure 5.2.

	Sim 5.13	*Sim 5.14*
Circuit Parameters	Table 3.1	Table 3.1
Fault Arc model	None	None
Conductor separation arc model	Mayr model	Mayr model
Conductor Separation	Constant speeds of 2m/s to 20m/s	Constant speeds of 10m/s; 20m/s; 40m/s
Conductor Type	N/A	N/A
Ruling Span length	N/A	N/A
Load Conditions	P1: 0kW	P1: 0kW
(Using a 0.96 power factor)	P2: 0kW	P2: 0kW
	P3: 600kW; 1200kW; 3600kW	P3: Varies from 0 to 900A
Line Lengths	L1: 10km	L1: 10km
	L2: 10km	L2: 10km
	L3: 20km	L3: 20km
Time of fault inception	N/A	N/A
Time of conductor failure	0.03s	0.03s
Time of arc extinction	0.08s	0.08s

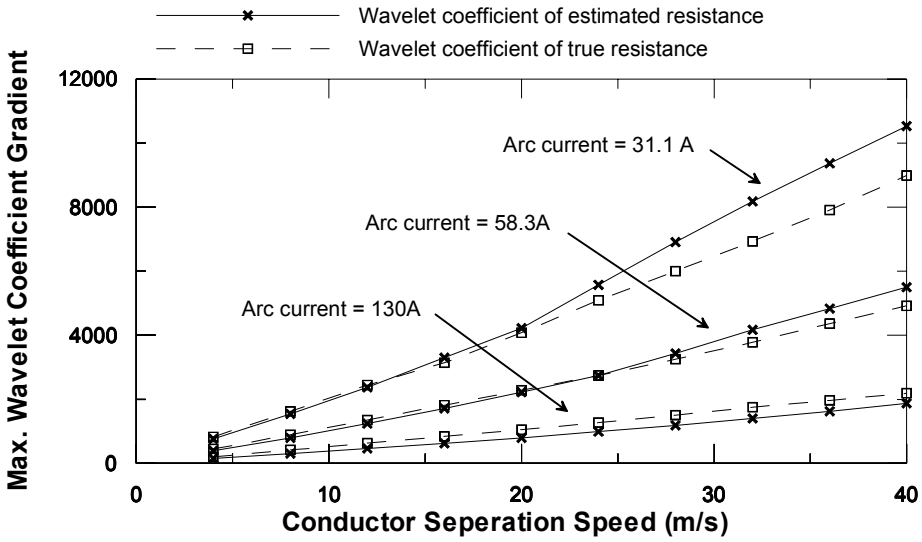

Figure 5.11: Influence of load current and separation speed on the gradient of the peak wavelet coefficients of the estimated and true resistance network resistance. (*Simulation 5.13*)

Equation (5.13) was tested to check if the same constant, K_d, would hold under a variable arc length. The arc length z_g of Equation (5.13) was replaced with the actual separation speed v_g while the maximum wavelet coefficient C_5 was replaced by the gradient of consecutive peak wavelet coefficients m_{c5}. The speed and current values

presented in Figure 5.11 were used in this modified equation. However, unacceptably large errors were obtained confirming the theory that a different constant will be needed under dynamic arc lengths.

The second set of tests was done with three constant conductor separation speeds but variable loads (Table 5.8 – *Simulation 5.14*). The mean gradient of the wavelet coefficient, inductance and current was measured for each simulation. The results of *Simulation 5.14* are shown in Figure 5.12. It shows that the gradient of peak wavelet coefficients is inversly proportional to the arc current. The optimum values for x, y and z were estimated by using Equation (5.14) and the data obtained from *Simulation 5.14*. The optimum point was again defined as the point with the smallest percentage standard deviation. The estimated values for x, y and z were 1.12, 1.12 and 0.06 respectively. The small z value indicated the low influence of inductance on the system and the inductance parameter X in Equation (5.14) was therefore discarded. A standard deviation of 519 (6.8%) was calculated with an average dynamic constant K_d of 7591. The distribution of the individually calculated K_d values for the data shown in Figure 5.12 is presented in Figure 5.13.

$$v_g = \left(\frac{m_{c5}}{K_d}\right)^{1/1.12} I_{arc} = 3.431\times10^{-4} I_{arc} \left(m_{c5}\right)^{1/1.12} \tag{5.15}$$

Equation (5.15) can be used to estimate the separation speed of a broken conductor based on the current zero period resistance variation due to arcing. This equation was tested on a case study using a simulated conductor separation speed of 28m/s. The network load was varied to obtain load currents of 628A, 345A, 343A and 108A and the estimated inductances of the circuit were 46.5mH and 174mH. The estimated conductor separation speed for the different scenarios was 26m/s, 22m/s, 21m/s and 24m/s respectively. These values are accurate enough to detect an arc on a network due to conductor separation. It can be concluded that Equation (5.15) is accurate enough to be used in the detection of a breaking conductor.

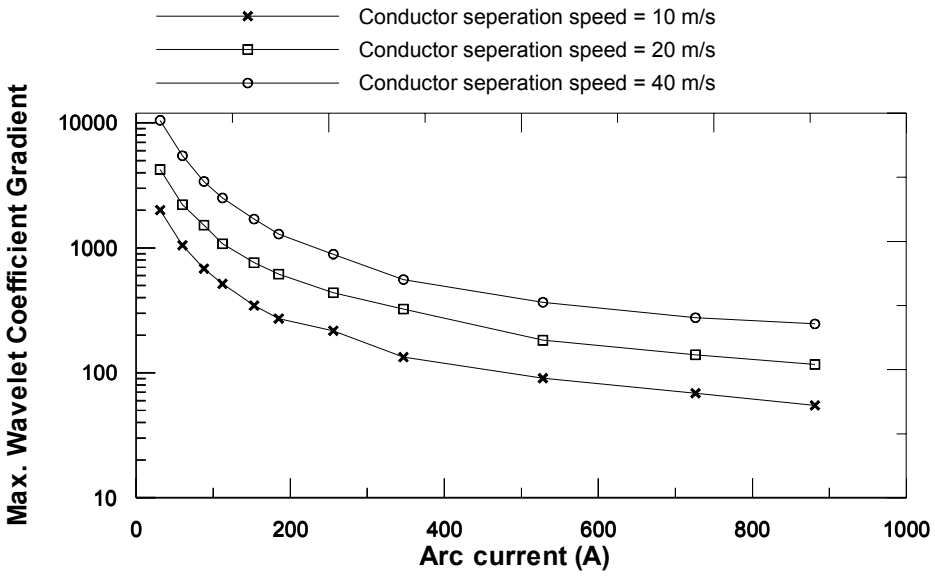

Figure 5.12: Gradient of peak wavelet coefficients of the estimated network resistance for various arc current and separation speed relations.

Circuit details are described by Table 5.8 (*Simulation 5.13*).

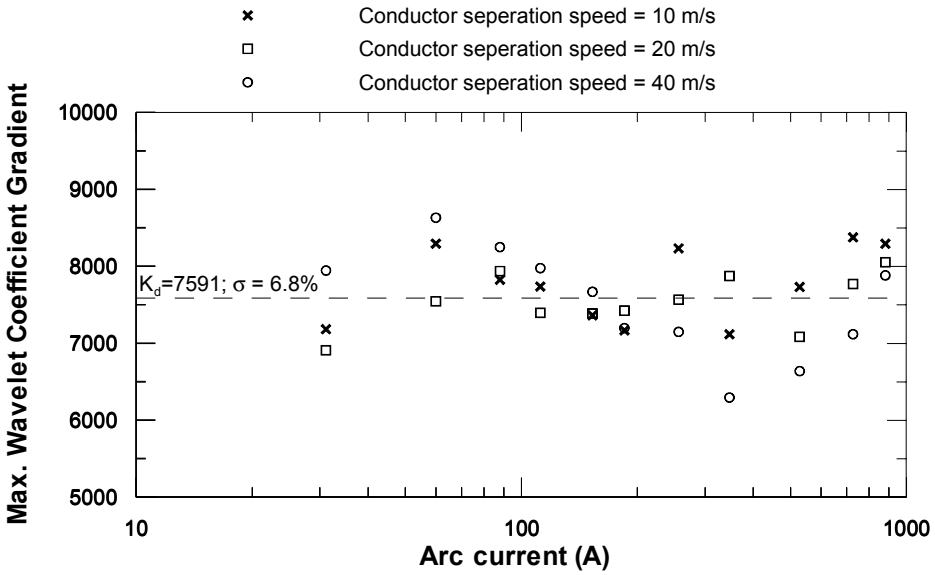

Figure 5.13: Distribution of individually calculated K_d values using Equation (5.12) and data points shown in Figure 5.12.

5.5.5 Influence of the Mayr model time constant on the wavelet coefficient

Equation (5.15) was derived from simulations that assume a constant Mayr model time constant. This constant is in fact variable as shown by Equation (2.7). The factors influencing the arc model time constant are arc current and arc length (Equation (2.7)). The time constant for a long, low current arc would be much smaller than for a short, high current arc. The peak resistance for this long, low current arc during current zero periods would be much higher in comparison to an arc with a long time constant.

The algorithm that is under investigation uses these peaks as primary measurements. It is therefore important that the influence of the variation of the time constant on the peak 5th level wavelet coefficient of the estimated resistance be investigated. The results can be extrapolated to the rate of change during conductor failure. A constant arc length of 500mm was used for the purpose of the tests (Table 5.9).

Table 5.9: Influence of the Mayr Model arc time constant on the peak wavelet coefficient of the estimated network resistance during current zero period. Details on P_1, P_2, P_3, L_1, L_2 and L_3 is shown in Figure 5.2.

	Sim. 5.16	*Sim. 5.17*	*Sim. 5.18*
Circuit Parameters	Table 3.1	Table 3.1	Table 3.1
Fault Arc model	None	None	None
Conductor separation arc model	Mayr model	Mayr model	Mayr model
Conductor Separation	500mm	500mm	500mm
Conductor Type	N/A	N/A	N/A
Ruling Span length	N/A	N/A	N/A
Load Conditions	P1: 0kW	P1: 0kW	P1: 0kW
(Using a 0.96 power factor)	P2: 0kW	P2: 0kW	P2: 0kW
	P3: 600kW	P3: 1200kW	P3: 3600kW
Line Lengths	L1: 2km	L1: 2km	L1: 10km
	L2: 2km	L2: 2km	L2: 10km
	L3: 2km	L3: 2km	L3: 20km
Time of fault inception	N/A	N/A	N/A
Time of conductor failure	N/A	N/A	N/A
Time constant	0.05;0.1; 0.2; 0.4; 0.6; 0.8; 1ms	0.05;0.1; 0.2; 0.4; 0.6; 0.8; 1ms	0.05;0.1; 0.2; 0.4; 0.6; 0.8; 1ms

The results are shown in Figure 5.14 as calculated static constant K_s values using Equation (5.13). It shows the influence of the Mayr model time constant on the wavelet coefficient of the estimated resistance. The arc resistance peaks are much

larger but of shorter time duration than for longer time constants. The 2nd level wavelet has become the dominant wavelet, indicating the high frequency nature of the resistance peak. It was previously shown that the 4th and 5th level wavelet coefficients are the dominant levels for a time constant of 500ms. For long time constants, the amplitude and frequency of the arc resistance peaks decreases. This causes a decrease in the 5th level wavelet coefficient but also in the peak resistance value during the current zero periods.

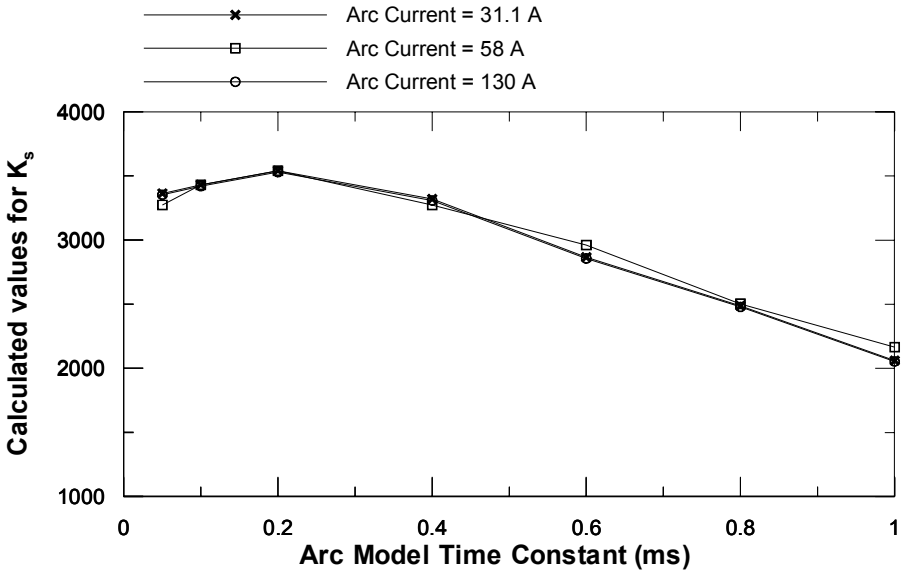

Figure 5.14: Calculated values for the static constant for simulations with various arc currents and Mayr model time constant.
Simulation details are shown in Table 5.9.

The normalised maximum wavelet coefficient of the estimated resistance is acceptable for time constants between 0.05ms and 0.6ms. A maximum error of 15% could be expected in these regions. The exact reason for the high level of invariance becomes evident in Figure 5.15.

As an example a conductor with the broken ends separating at 10m/s in the centre of a 4km line was simulated with a arc model time constant of 0.5ms as well as 0.05ms. Figure 5.15 shows the true and estimated network resistance for both time constants. The results in Figure 5.15 clearly show that the invariance of the wavelet coefficient under different time constants is due to the poor performance of the resistance estimation technique. The true resistance that was simulated with a 0.05ms time

constant peak at 89Ω, in comparison with the peak estimation of 23Ω for a 0.5ms arc model time constant. These peaks are of very short period lasting less than 4 samples. The resistance estimation algorithm uses at least three current and voltage samples under the assumption that the resistance is constant. It is therefore expected that the algorithm will not be able to produce accurate results during these very short and high resistance peaks. One can therefore conclude that a variance in the arc model time constant will only have a minor influence in the speed estimation algorithm.

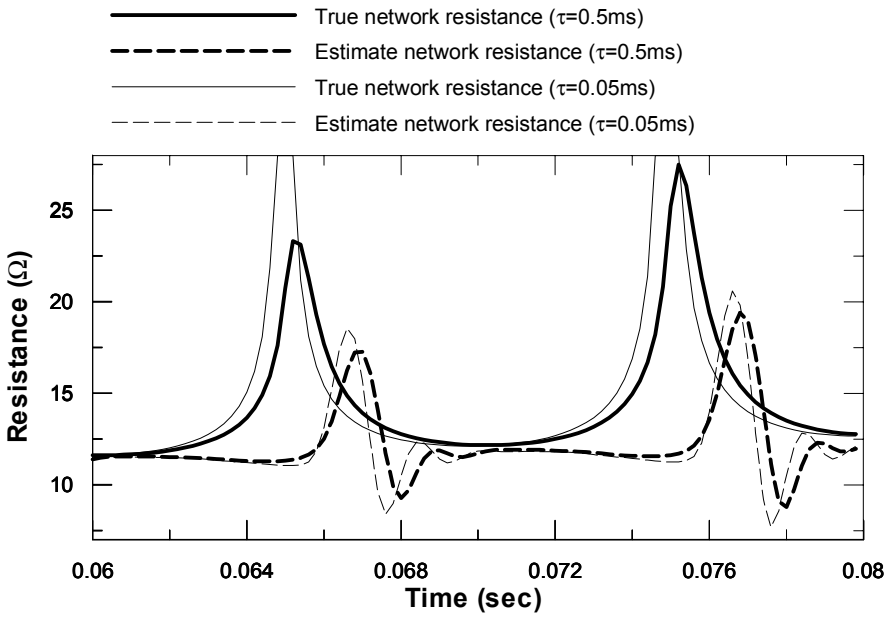

Figure 5.15: Estimated and true network resistance for a 4km simulated line with a 300A load. The arc was simulated between broken end points of a conductor with a separation speed of 10m/s and Mayr time constant of 0.5ms and 0.05ms.

5.5.6 Guarding against transients

The most important factor in securing the system is making sure that the estimated resistance peaks are caused by an arc. An arc would cause an increase in the resistance during the current zero periods. The ideal algorithm must use the first maximum current peak after the current zero. On an unbalance radial network, the arc current is calculated by subtracting the post-incident current from the current during the possible fault. This method will not always be that accurate due to load

and voltage variations. Short time durations before and after the calculated arc current zero periods should be checked for the possible maxima of the wavelet due to this inaccuracy of the true arc current estimation. A coefficient of 0 must be used if no maximum is detected in this region.

The linearity of the estimated conductor displacement must also be checked. This will help to identify false trips due to transients using the correlation coefficient as a test to eliminate these false trips. A much higher limit of 0.95 was set for the theoretical study. Only 5 samples will be used per test and would require a much stricter limit as in the case of the estimated arc voltage algorithm.

5.5.7 Development and testing of the wavelet algorithm on a simulated network

The following algorithm is proposed for conductor failure detection:

(a) Filter out all high frequencies (>700Hz) of both current and voltage signals.
(b) Calculate the network resistance.
(c) Apply a continuous wavelet transformation with a “Mexican hat” as the mother wavelet.
(d) Apply Equation (5.13) to detect any possible arc.
(e) A marker must be placed as a starting point if at least 3 peaks are detected during the current zero periods larger than a pre-set value.
(f) These peaks should disappear within 150ms. The true arc current is calculated by subtracting the post arc current from the current during the arc.
(g) Re-calculated the arc resistance using the true arc current.
(h) Apply a continuous wavelet transformation to this new estimation of resistance.
(i) Estimate the speed of separation with Equation (5.15).
(j) Calculate the correlation factor of the zero current coefficient peaks for the last 50ms data.
(k) Activate the alarm if the gradient is above 5m/s and the correlation factor is above 95%.
(l) Trip the feeder if the alarm is activated for a period longer than 20ms.

The algorithm was applied on current and voltage waveforms obtained from *Simulation 5.4, 5.5* and *5.6* (Table 5.5). The results of the simulations are shown in Table 5.10. The limits were set on a minimum conductor separation speed of 5m/s with a required correlation of 95%. The algorithm identified the conductor failures of all three scenarios. Speeds above the 5m/s limit are estimated during fault inception. These faulty estimations are due to the initial arcing during the fault inception. The algorithm detects a sudden increase in the wavelet coefficient and calculates an average separation speed of the two broken ends of the conductor. The correlation factor is used to calculate the linearity of the arc length increase. The correlation factor is 0.7 for a step signal at 50% of the data window. This are the typical values obtain at fault inception (*Simulation 5.16*) and at the start of the conductor separation (*Simulation 5.14 and 5.15*). There is some concern about the accuracy of the estimated conductor separation speed. The theoretical separation speed of the Banana conductor under 25% of the ultimate tensile strength is 14m/s. The algorithm estimates a speed of only 8m/s for *Simulation 5.5* and 20m/s for *Simulation 5.6*. The poor estimation of the separation speed for *Simulation 5.6* is explained in Section 5.4.2. A speed of 14m/s is estimated if the measured fault current is used and not the estimated current by subtracting the post-fault current from the current during the fault.

Table 5.10: Results of the proposed wavelet gradient algorithm to detect a broken conductor. The algorithm was applied on voltage and current waveforms obtain from simulation results (Table 5.4). Note that the true conductor separation speed is 14.4m/s.

	Sim. 5.4			*Sim 5.5*			*Sim 5.6*		
Time (ms)	V_g *(m/s)*	*r (p.u.)*	*Trip signal*	V_g *(m/s)*	*r (p.u.)*	*Trip signal*	V_g *(m/s)*	*r (p.u.)*	*Trip signal*
60	0	0.72	0	0.1	0.58	0	15.2	0.67	0
70	0	0.36	0	0	0.07	0	20.5	0.74	0
80	0.1	0.72	0	0.2	-0.8	0	16.9	0.70	0
90	1.6	0.71	0	1.4	0.66	0	9.7	0.47	0
100	4.6	0.86	0	3.8	0.83	0	-0.3	-0.03	0
110	7.8	0.96	1	5.8	0.93	0	11.18	0.91	0
120	10.0	1.00	1	7.1	1.00	1	15.39	0.96	1
130	10.6	1.00	1	7.7	1.00	1	19.6	1.0	1
140	10.7	1.00	1	8.0	1.00	1	19.6	1.0	1
150	10.9	1.00	1	8.6	1.00	1	20.3	1.0	1
160	241	0.66	0	7.1	0.97	1	40.9	0.81	0
170	69	0.33	0	1.2	-0.3	0	0.1	0.1	0
180	1.2	0	0	0	-0.7	0	0	-0.4	0
190	0.5	0	0	0	-0.8	0	0	-0.6	0

5.5.8 Limitations

The algorithm presented in this section is able to identify a mechanical failure of a conductor under normal load and faulted conditions. The resolution of the speed calculation is lost on radial networks feeding a multitude of loads. Poor estimations were also obtained during an actual earth fault condition. The system will perform better on conductor installations with a high breaking speed because a large enough buffer can be left between other possible arc length increases and that of a failed conductor. The second limitation to the system is the requirement for a large enough current, as a small current would generate an insufficiently short arc and will make the algorithm ineffective.

5.6 Conclusion

Two new algorithms for conductor failure detection were presented. The first algorithm makes use of the estimated arc voltage. This algorithm produces stable conductor separation speed estimations. However, the response time of the algorithm is very slow in comparison to the second algorithm. The second algorithm makes use of the resistance variation caused by an arc on a network. A wavelet transformation was used to isolate this variance. An empirical equation was derived to describe the relationship between the wavelet coefficients and circuit parameters and is more immune to transients. It lacks however the accuracy of the first algorithm. The optimum algorithm would therefore be a combination of the two algorithms. For best results, the correlation factor must be calculated using the estimated resistance wavelet coefficients while the separation speed is estimated using the arc voltage algorithm.

Both the algorithms are based on empirical equations and models. The arc voltage algorithm is based on Stokes' work on free burning arcs whereas the wavelet algorithm is based on the Mayr model. The second algorithm will be much more easily influenced by inaccuracies of the model than the arc voltage algorithm. It is therefore recommended that the second algorithm should be used for arc identification rather than the actual speed estimation. The arc voltage algorithm must be used for the conductor separation speed estimation.

6. DETECTION OF CONDUCTOR CLASHING

Chapter 5 investigates the possibility of using the properties of an arc to identify a broken conductor. The investigation revealed that the arc length would increase linearly after the initial acceleration of the broken ends. This linear increase in arc length was used to identify a broken conductor. Chapter 6 will investigate the possibility of using the same philosophy to identifying clashing conductors due to high winds.

There are two, well researched, categories of conductor oscillation; Aelonian oscillation and Galloping. Aelonian oscillation is a high frequency, small amplitude oscillation that will not cause conductor clashing. This type of oscillation will however cause conductor fatigue. The second type of conductor oscillation is galloping that is a low frequency oscillation due to ice forming on the conductor. The ice layer breaks the symmetry of turbulence forces and causes an upward force. This oscillation has large amplitudes and is not only restricted to in-line oscillations.

A third, less researched, oscillation is caused by extremely high wind speed that vary in speed. The conductor starts oscillating due to variation in the wind speed. The oscillation consists of harmonic frequencies with the first order natural frequency of the line as base frequency [59]. These oscillations of the three conductors are normally synchronised. It is however quite possible that these oscillations can become out of synchronisation under certain conditions and cause conductor clashing.

The aim of this section is to investigate the possibility in detecting this phenomenon. A typical line under high wind conditions with a second harmonic oscillation will be simulated. The simulation will be used to investigate the speed of arc length increase to determine if the same method is viable as discussed in Chapter 5.

6.1 Method for modelling of clashing conductors

6.1.1 Theory of model

At present no model exists to simulate the possible clashing of two conductors. The simulation of clashing conductors will be based on a description of May [59]. A conductor will act as a rigid object in low wind velocities and the natural frequency of such oscillation is also calculated accordingly. The oscillation is caused by a variation in the wind speed. The motion of the oscillation is contained in two parabolas, one deeper than the other such that the mean position is permanently displaced if viewed in plan [59]. The swing tends to be in synchronism with the other phases since large differences in the sag are necessary to influence the frequency. Equations for the calculation in the difference of the two conductors' frequencies are presented in the *Transmission Line Reference Book* [3].

May [59] however reported that for larger swing angles the rigid body analogy fails. The span started to behave as a set of elastically connected pendulums, each swinging around its own swing fulcrum. Viewed in plan, the mean position of this motion is again a parabola and onto this mean a single oscillating sinusoidal cycle is superimposed. This is a form of resonance and which continues undamped for a considerable time. Adjacent conductors do not necessarily have the same period of motion and tend to move in and then out of synchronism. According to May, conductor clashing is most likely to happen when the conductor oscillation moves out of synchronism [59].

Louredo-Souza reported simulating a possible conductor clashing in a wind tunnel [71]. He was however studying dynamic forces on parallel conductors under high wind conditions. It was reported that the possible conductor clashing occurred when turbulences was caused by a person inside the wind tunnel. Loredo-Souza *et. al* is currently working on a theoretical model describing this phenomena.

The model described by May [59] is the best available model and will therefore be used to simulate conductor clashing. The finite element conductor model that was developed in Chapter 4 will be used to describe clashing of two conductors. The magnetic force poses as a problem for very short distances between the two conductors. The equation used for calculating the magnetic force assumes the radius

of the cable is negligibly small in comparison to the distance between the conductors. Equation (4.2) will therefore only holds for distances larger than 100mm.

May stated that the conductor wave will consist of first order and second order standing waves under large deflections of the conductor. However, the first order standing waves of two adjacent conductors will be in phase. The second order standing waves will be out of phase and will cause the conductor clashing. As the purpose of this calculation is to determine the speed of separation after conductor clashing, the first order standing wave can be ignored and only the second order standing wave will be used as initial conditions.

There exists an infinite number of initial conditions. No known theoretical model exists for the calculation of the amplitude of the conductor deflection under high wind conditions. However, it is well known that conductors do clash under high winds. The minimum amplitude of the conductor deflection that will cause conductor clashing could be half the conductor spacing as the second harmonic oscillation of the adjacent conductor should be 180° out of phase for the two conductors to clash. These conditions will be used as the original initial conditions of the wave equations.

Equations (4.2) and (4.3) are second order differential equations and therefore require two time consecutive initial conditions. Two identical standing waves are used as initial conditions for the above scenario. This implies that the conductor was at its turning point when it clashed with the adjacent conductor. The initial conditions can vary considerably if the difference in phase angles is not equal to 180°.

Stokes *et. al.* showed that an arc between two parallel conductors will move away from the supply until the end of the conductors is reached [54]. The same phenomenon is expected for an arc that originated after two conductors clashed. Stokes reported a speed of 60m/s for a conductor spacing of 165mm and peak current of 20kA. A typical 11kV distribution line will have a 750mm conductor spacing and 5kA RMS fault current. The forces responsible for the arc movement are proportional to $\delta(Li^2)/\delta x$ [54] where L represents the total line inductance, i

represents the current and x is the position of the arc. It can therefore be expected that the speed of the arc on the line will be more or less the same magnitude as measured by Stokes *et. al.*

The simulation will also assume a radial network with the line being fed only at one end. Therefore only a part (a quarter or three quarters) of the conductor span will be exposed to the magnetic field, depending on the direction of feed. The speed of the arc will influence the rate at which a larger part of the span is exposed to the magnetic forces. It is therefore essential that this arc property is included in the simulation. A constant speed of 60m/s will be used to simulate the movement of the arc. A predefined constant speed is use to simplify the problem.

6.1.2 Testing of Model

The model will be tested on the same line parameters than what was used in Chapter 4 (Table 4.1). It will be assumed that the fault will be cleared within 500ms. The dynamic evaluation is therefore only required up to 500ms. MATLAB is used to solve the discrete differential equations based on Equation (4.2) and (4.3). The simulation was checked using the natural frequency of the overhead line. Equation (6.1) can be used to calculate the natural frequency f_n, for the n^{th} harmonic, analytical [60]. In Equation (6.1) H represents the conductor tension; ρ represents the mass per unit length and L the span length. A slightly higher frequency is obtained from the simulation if the fault current is set to 0A. It must be noted that this equation was derived for small amplitude in-plane cable oscillations with the assumption that the conductor tension H is constant. It can be explained by the tension variation in the cable due to in-plane oscillation. The simulation produced a steady state second order standing wave if the magnetic forces are ignored.

$$f_n = \frac{n}{2L}\sqrt{\frac{H}{\rho}} \tag{6.1}$$

Figure 6.1 is a typical horizontal displacement figure of a clashing conductor. The line consists of a Grape conductor with 750mm conductor spacing and tensioned to

25% of the UTS of the conductor (Table 4.1). The ruling span length of the line is 80m with a 8kA fault level. The conductor profile is shown after every 20ms. The fault position in Figure 6.1 is at 20m. Only parts of the conductor are exposed to the magnetic field which is dependent on the direction which it is fed from. The conductor between 20m and 80m is exposed to the magnetic field for Figure 6.1(a) while the conductor between 0m and 20m is exposed to the magnetic field for Figure 6.1(b).

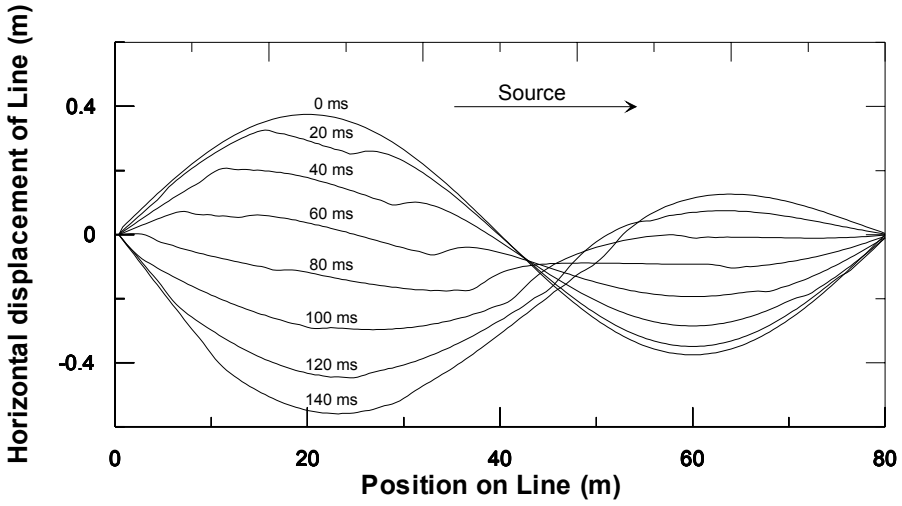

(a)

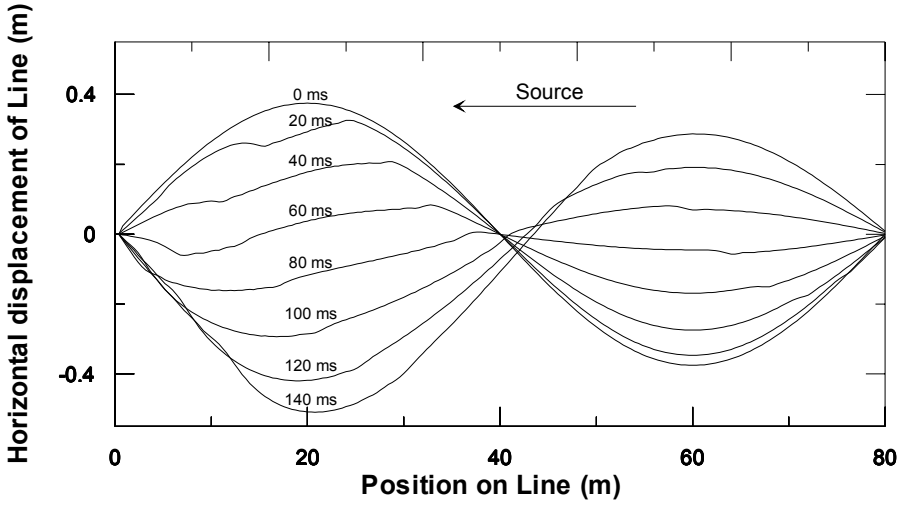

(b)

Figure 6.1: Horizontal displacement of line with a fault starting at 20m. The line is constructed of Grape conductor at 25% of UTS; 750mm conductor spacing; 8kA fault current; 80m span length (a) Conductor between 20m and 80m is exposed to magnetic field (b) Conductor between 0m and 20m is exposed to magnetic field.

The proposed simulation model produces realistic results if it is used without any magnetic forces but was not proven experimentally. It is however based on existing mathematical wave equations and physical techniques and should produce accurate results. The magnetic force term will, however, only be valid for distances larger than 10 times the conductor diameter. One must therefore assume that the simulated fault starts out as a flashover.

6.2 Results of simulations

The speed at which the conductors are separating is highly dependent on the line parameters and size of magnetic force during the faulted conditions. The line parameters (cable tension, conductor mass, span length and conductor spacing) will influence the natural frequency of the oscillation in accordance with Equation (6.1). The fault current will again cause the initial acceleration of the two conductors away from each other just after clashing. The aim of this investigation is to search for a unique characteristic that can be used to identify the clashing of the conductors. The study will start with the simplest case where the two clashing conductors have an anti-symmetric movement relative to each other. The fault current, cable tension and span length will be specifically looked at since these parameters can vary on the same line at different locations.

Fault Current:

A change in the source impedance, fault impedance or position of the fault on the line will influence the fault level. The fault current is responsible for the initial acceleration of the conductors away from each other. The fault current was varied on a simulated line constructed with Grape conductor and tensioned to 25% of the UTS. The span length of the conductor was 80m while the spacing between phases was 750mm. The results for a 0kA and 16kA fault current are shown in Figure 6.2.

The simulation done with no fault current represents the natural oscillation of the conductor. There is a slow initial acceleration of the conductor until it reaches the natural rest position where upon it decelerates. A conductor with a 16kA fault

current will have a large initial acceleration and start decelerating at the same time as would have happened without any fault current.

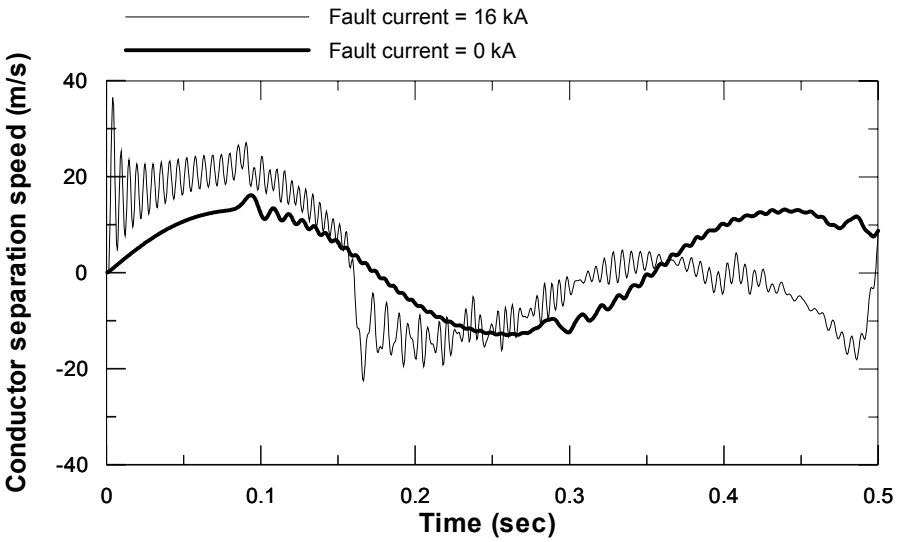

Figure 6.2: Arc length gradient after conductor clashing for 25% UTS cable tension. Line parameters: 80m span length; Grape conductor; 750mm conductor spacing.

Initial conductor tension

The cable tension H will increase the natural frequency of the conductor in accordance with Equation (6.1). The magnetic field will have less influence on a line with a high cable tension since the natural frequency is already high. However, conductor clashing is most likely to be found on low-tensioned cables. Figure 6.3 shows the speed of arc length increase for a line tensioned only to 10% UTS. The span length and conductor spacing of this line was kept on 80m and 750mm respectively.

The results indicate a much slower natural frequency in comparison to Figure 6.4 for no fault current. The fault current also has a more prominent influence on the maximum speed of the conductor in comparison to the results shown in Figure 6.2 which uses a cable tension of 25% UTS. The conductor separation speed increases for almost 100ms to reach a maximum speed of less than 10m/s. However, the conductors will accelerate within less than 10ms to a maximum separation speed of 18m/s if the conductor carries a large fault current (16kA).

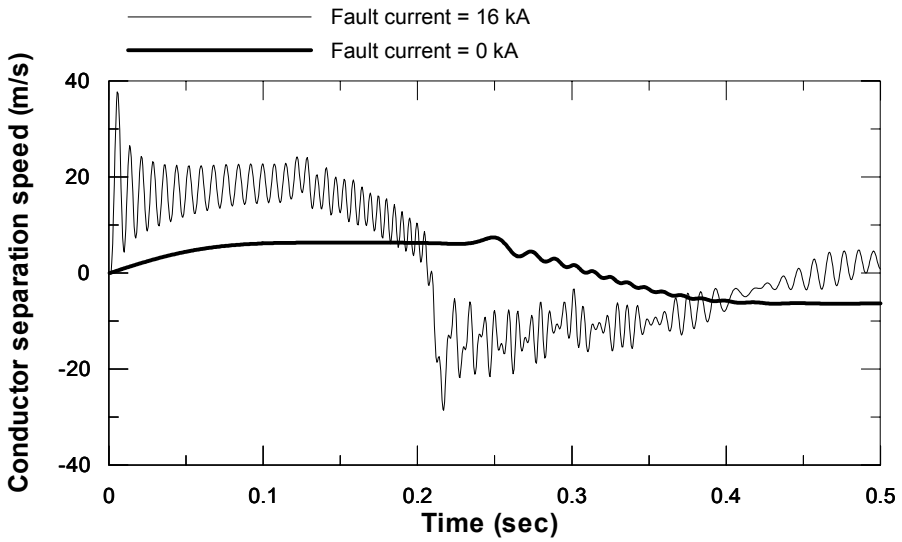

Figure 6.3: Arc length gradient after conductor clashing for 10% UTS cable tension. Line parameters: 80m span length; Grape conductor; 750mm conductor spacing.

Span length of conductor

The span length on a line is highly variable and depends on the geographical route of the line. Long spans are expected over valleys while short spans are expected over hill crests. The natural frequency of the oscillation described by Equation (6.1) decreases with increase in the span length. This decrease in the natural frequency will have a major impact on the conductor separation speed after conductor clashing. A line with a 16 kA fault was simulated for a 50m and 100m span length. The line parameters were 25% UTS cable tension; 750mm conductor spacing and constructed with Grape conductor.

The results of the simulations are presented in Figure 6.3. It clearly shows that the shorter span length reaches the maximum speed much faster and this speed is also much higher than for the longer span length. The time required before the conductor separation speed decelerates is almost double that than for a line with a 100m span length.

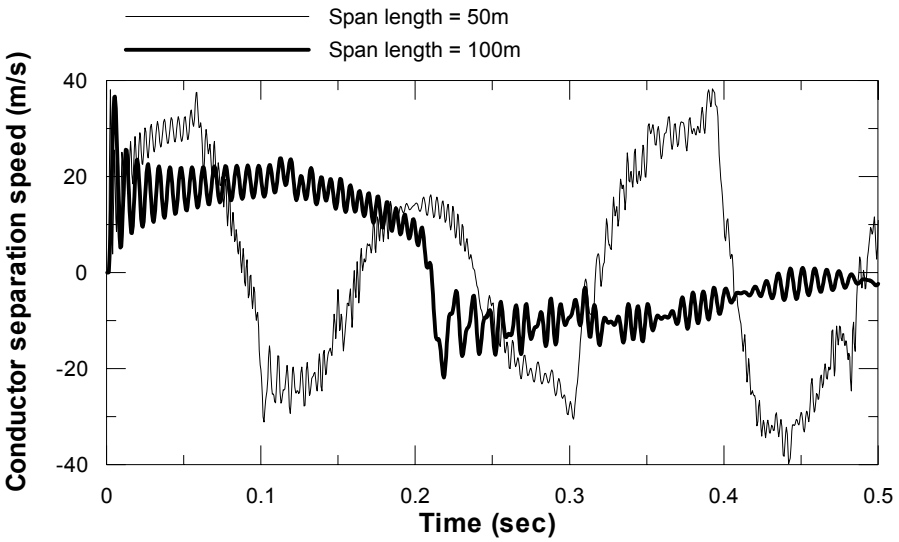

Figure 6.4: Arc length gradient after conductor clashing for various span lengths. Line parameters: 25% UTS cable tension; 16kA fault current; Grape conductor; 750mm conductor spacing.

6.3 Discussion

The results of the simulations are shown in the previous section. These simulations are based on a very specific type of conductor clashing as discussed in [59]. The simulation results indicate that the separation speed profile of the conductor is highly variable depending on the line parameters. From the above simulations it is clear that the maximum conductor separation speed is especially dependant on the fault current (Figure 6.2 and 6.3) and span length (Figure 6.4). Speeds of less than 10 m/s were obtained from the simulations for low fault current faults with a span length of 80m. The separation speed increases to a maximum value of 30 m/s once this span length is reduced to 50 m and the fault current is increased to 16kA.

This highly variable maximum separation speed makes it impossible to use the maximum speed to identify conductor clashing. It will be possible to normalise the maximum speed with the current but it is impossible to normalise it the span length since the span length is unknown. A possibility might exist to normalise the maximum separation speed to the oscillation frequency. The problem in this concept is that the relay will need to determine the oscillation frequency between 70ms (Figure 6.4) and 300 ms (Figure 6.3). This time period might be longer than time to clear the fault.

The most unique feature of the separation speed due to conductor clashing is the deceleration of the rate of increase in the arc length and the ultimate shortening of the arc length. This is the ideal characteristic for identifying clashing conductors. Again, it will require that the relay does not operate before it detects a negative speed after the initial positive speed was detected.

This method would be ideal for lines with a high natural frequency. A high natural frequency will decrease the time the relay is required to wait before a negative speed is detected. However, a line with a high natural frequency will have a short span length and high initial cable tension. These are also the lines with the lowest risk of conductor clashing. Figure 6.3 show that a poorly tensioned line will have a negative conductor separation speed only after 200ms at high fault currents and after 300ms for a very low fault current.

The evaluation in this chapter assumes only one initial condition, which will occur when the two adjacent conductors' second harmonic oscillation is exactly 180° out of phase. This initial condition provided that the two adjacent conductors second harmonic oscillation is at the turning point when flashover occurs. The conductor clashing can however be far more complex for other initial conditions. The magnetic force during the clashing can cause a magnetic force in the opposite direction to the momentary momentum of the conductor and will cause a much slower increase in the arc length.

6.4 Conclusion

Only a very specific type of conductor clashing was simulated. The simulations indicated that the only method in detecting these specific clashing conductors is by detecting a negative conductor separation speed after the initial positive speed. This will however require that the feeder may not clear the fault for up to 400ms, which is unacceptably long. It is therefore impractical to identify clashing conductors by monitoring the arc length.

The arc length and current are the only two variables required to simulate a free-burning arc. It is therefore evident that it is impossible to identify clashing conductors based on the existing arc model used in this work. Stokes mentioned in his paper that the arc voltage between two parallel conductors varies more that that between two electrodes [54]. This is due to the cooling of the arc caused by the lateral movement of the arc between two parallel conductors. It is however unknown what the amplitude and frequency is of this variation. Should the frequency be small enough, it might just be possible to detect this variation. Further experimental data is however required to explore this possibility.

7 ESTIMATION OF VOLTAGE DIPS USING AN EXISTING DIFFERENTIAL EQUATION ALGORITHM

In this section further development of basic work undertaken in Section 3 is proposed. Power quality is a major concern for utility companies. One of the criteria for Power Utility companies is the limitation of the amount, total duration and amplitude of the supply voltage dips and sags on the network. The actual measurement of such voltage dips is not always practical on MV distribution networks as the faults causing dips can occur at any point in the network. The supply busbar is normally the only point in distribution networks that has sufficient measuring equipment to monitor voltage dips. It is impractical to install this kind of equipment at every point of delivery for small electricity users.

In this section, a new method is proposed for estimating the voltage waveforms along the faulted line during voltage dips. The method relies only on the measured voltage and current waveforms at the supply busbar.

The proposed distance to fault locator algorithm of Radojevic *et. al.* [6] forms the base in the estimation of the line supply voltage under faulted conditions. The algorithm uses the least square method as an estimation technique with the inclusion of the non-linear properties of fault arcs that are represented by flat-topped waveforms. This algorithm enables the estimation of the arc voltage and constant fault resistance for supply busbar measurements. In this section the estimated fault voltage at the point of fault will be used to determine the line voltage at other positions along the line.

7.1 Proposed Algorithm for Voltage Estimation during faulted conditions on a MV feeder

Radojevic's fault locator algorithm's [2] output is an estimated square wave arc voltage amplitude as well as a resistance value that includes the fault resistance.

Radojevic *et. al.* suggested that the arc voltage amplitude estimation must be part of the decision making process for auto re-closing of a tripped overhead line feeder breaker. The actual voltage at the point of fault can be estimated by the use of these results from the fault locator algorithm. Equation (7.1) describes the estimated voltage v_f at the point of fault as a function of the line's positive (r) and negative sequence (r_0) resistance per unit length, estimated arc voltage amplitude U_a, estimated distance ℓ to fault and zero sequence line current (i_{a0}). The subscribt k represents the sample number.

$$v_{f_k} = U_a \cdot sign\left(i_{a0_k}\right) + i_{a0_k} \cdot \left(R_e - \ell \cdot \left(r_0 - r\right)\right) \tag{7.1}$$

The resistance R_e in Equation (7.1) represents an equivalent resistance that includes the linear part of the fault resistance as well as the positive and zero sequence resistance of the overhead line. This resistance is one of the algorithm's outputs that are readily available.

Only high current faults will have a dramatic influence on the voltage levels on the MV network. The fault current will therefore be the principal cause of the voltage dip along the fault current route. It is assumed that the rate of voltage decrease is linear along the fault current route. This assumption is based on the fact that load current may not cause a voltage drop larger than 10%. The estimated voltage v_e at any point along the line with a distance a from the point of measurement is described by Equation (7.2).

$$v_{e_k} = v_{f_k} + \left(\frac{\ell_k - a}{\ell_k}\right) \cdot \left(v_{m_k} - v_{f_k}\right) \tag{7.2}$$

In Equation (7.2), the voltage v_m is the voltage measured at the supply end of a feeder and ℓ_k is the estimated distance to the fault. The influence of the variation in the load along the line is ignored. This will be true if the fault current is significantly larger than the load current. The second restriction is the use of voltage regulators along the line. The influence of the regulator will be determined by its tap position at the time of inception of the fault. Equation (7.2) does not support a line with a voltage

regulator. It is however a simple procedure to change Equation (7.2) to allow for a voltage regulator if the tap position is known. The simulations will be done without any voltage regulators.

Once the arc voltage is determined by Radojevic's method it is possible to estimate the actual line voltage along the fault current route. It is virtually impossible to estimate the voltage along a healthy tee that is connected somewhere along the faulted route without knowing the actual current in the tee. This voltage drop will be small compared to the voltage drop cause by the fault current. It is assumed that the fault current is significantly larger than the pre-load current. The voltage level at the end user along a healthy branch will therefore be estimated as the voltage at the tee along the fault current route.

7.2 Testing the proposed algorithm on a simulated network

The effectiveness of this method will be discussed and evaluated based on a radially fed medium voltage system. A "teed" network is shown in Figure 7.1 that will be used for testing the proposed algorithm under simulated conditions. A fault will be induced at the end of the MV line. The voltage of the faulted phase will be estimated at both point A and B. These estimated values would be compared with the actual voltage. The RMS value of the estimated voltage waveform will be compared for various arc lengths and earth fault resistance. The RMS values are used in the evaluation since the power quality specifications [72] specify the voltage dip in terms of the RMS value. No mention is made in [72] of very short durations of harmonics caused by the arc on the network. The actual voltage waveform is therefore of less importance than the RMS value.

The simulation of the fault makes provision to include a constant fault resistance as well as an arc. This is to determine the effect of the fault resistance on the accuracy of the algorithm. All other simulation parameters are specified in Table 3.1 while Figure 7.1 shows the circuit used for the simulation model. The three loads were chosen such that it caused a 130A load current in each tee circuit.

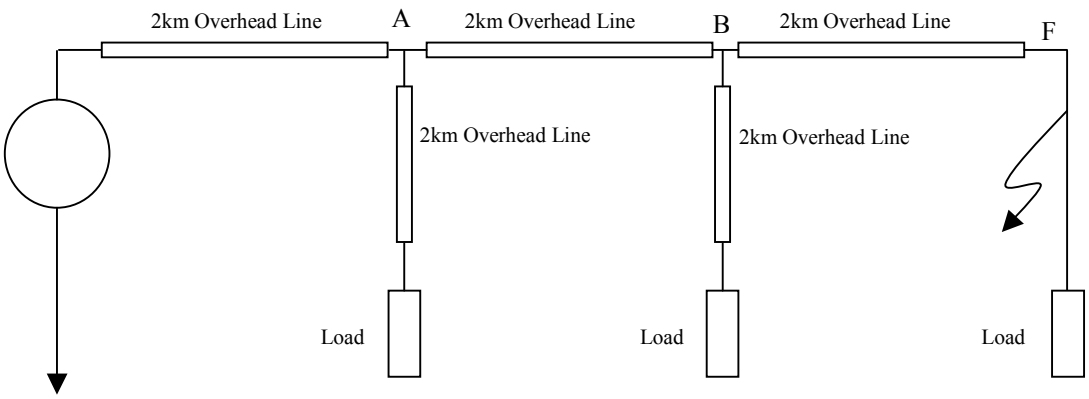

Figure 7.1: Single-line schematic diagram of teed distribution network with a single-phase to ground fault at point F.

7.2.1 Comparison of the actual waveform estimation with the true voltage

The original distance to fault locator algorithm [2] estimates the arc voltage as a square wave. In reality this may not be true. The Mayr model [50] causes a slight delay in changes in the arc's dynamic resistance. The arc voltage also tends to increase for currents higher than the critical arc current. This critical arc current is dependant on the arc length and was discussed in Section 1 [54]. All these factors cause a deviation from the idealised square arc voltage waveform that is estimated by Radojevic's algorithm. The algorithm makes use of the least square error method to determine arc voltage. The actual arc resistance is therefore represented by a square wave plus a sinusoidal wave due to voltage drop across R_e.

Figure 7.2 shows the true arc voltage waveform at the fault position and the arc voltage estimated from measurements at the supply busbar. Figure 7.3 shows the estimated and true line voltage 2km from the fault. The simulation was done for the worst-case scenario with no linear fault resistance since this would only dominate the non-linear resistance of the arc. The non-linear arc resistance is the only fault resistance used. The main difference between the estimated and true voltage waveform at the fault (Figure 7.2) is the high frequency components present in the

true voltage waveform. They are however attenuated and decrease with distance from the fault.

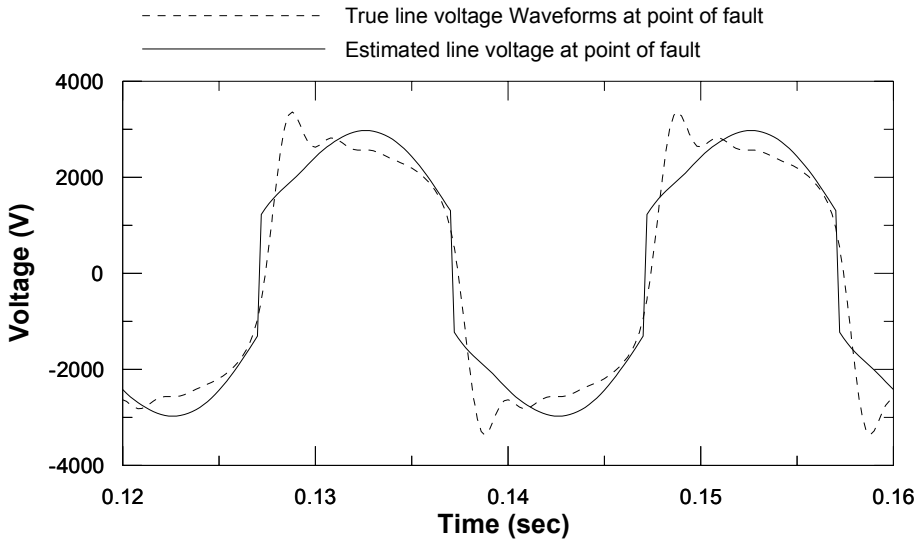

Figure 7.2: Line voltage at point of arc fault (F) with a 2.0m long arc. The network is described by Figure 7.1.

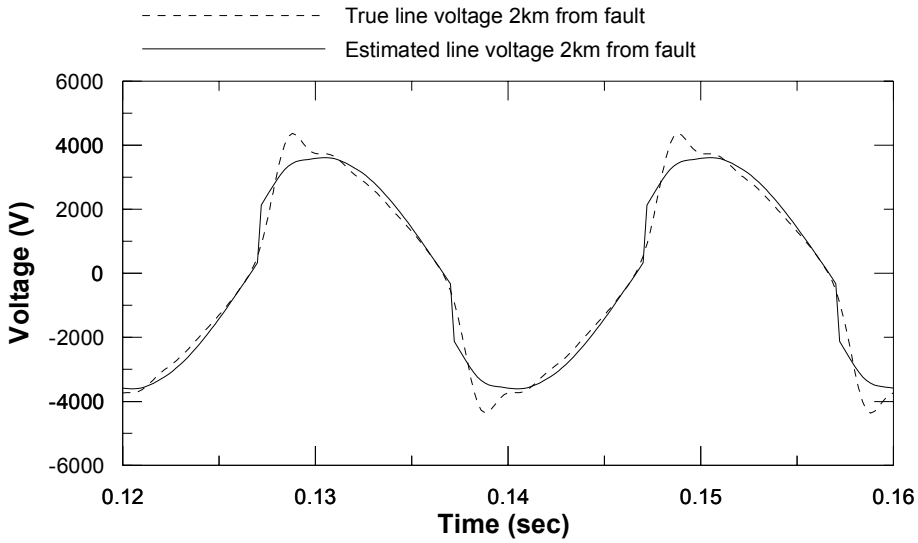

Figure 7.3: Line voltage 2km (B) from the arc fault with a 2.0m long arc. The network is described by Figure 7.1.

7.2.2 Influence of Fault Resistance on the accuracy of the estimation

Earth fault on MV overhead lines are mainly restricted by the arc resistance, tower footing resistance and other material (such as timber poles) in the circuit. The

influence of this resistance on the estimated fault voltage was already discussed. The same simulation circuit was used as discussed in Section 7.2.1 to test the influence on the estimated RMS voltage level. The constant fault resistance was varied between 0Ω to 5Ω. The fault current for a 5Ω fault resistance on an infinite bus is 1.2kA, smaller than most distribution line fault levels. Fault resistances larger than 5Ω will result in only minor voltage dips. The results of these simulations are shown in Table 7.1.

Table 7.1: Accuracy of Algorithm for various fault resistances in series with a 1m long arc.

Fault Resistance	*Error of estimated Voltage (rms) at positions*		
	A	*B*	*F*
0Ω	0.3%	0.6%	1.6%
1Ω	0.4%	0.1%	0.9%
2Ω	0.4%	0%	0.2%
3Ω	0.2%	0.3%	0.4%
4Ω	0.4%	0.1%	0.6%
5Ω	0.4%	0%	0.9%

The distance to fault is 6km. Figure 7.1 defines position A, B and F.

The algorithm clearly shows an improvement in the accuracy for small increases in the fault resistance. This is caused by the decrease in the percentage non-linearity of the total fault resistance. The accuracy decreases again for larger resistance values. This decrease in accuracy is due to the decrease in the overall accuracy of the algorithm under larger resistance values. A more comprehensive discussion on this decrease in accuracy can be found in section 3. The overall accuracy of the algorithm for the different fault resistances is still high enough for the accurate estimation of the supply voltage to the end users during the faulted conditions.

7.2.3 Influences of the arc length on the accuracy of the algorithm

An increase in the arc length will cause an increase in the total non-linear resistance of an arc. One can therefore expect an increase in the error with the increase in the arc length due to the increase in the percentage non-linear fault resistance. The same simulation was used as discussed in section 7.2.2 for various arc lengths and a fault resistance of 0Ω. The results of these simulations are indicated in Table 7.2.

Table 7.2: Accuracy of algorithm for various arc lengths and no fault resistance.

Arc Length (mm)	*Error of estimated Voltage (rms)*		
	A	*B*	*F*
250	1.5%	3.1%	26%
500	1.1%	1.6%	10%
750	0.7%	0.3%	4.5%
1000	0.3%	0.6%	1.6%
1250	0%	1.2%	0.1%
1500	0.3%	1.8%	1.3%
1750	0.5%	2.1%	2.2%
2000	0.7%	2.4%	2.3%

The distance to fault is 6km. Positions A, B and F are defined by Figure 7.1.

The accuracy of the estimated voltage is very poor for arc lengths of 250mm and 500mm. The arc voltage amplitude in these cases is small. The estimated arc voltages are about 100V higher than the true fault voltage. This value is relatively small in comparison to the system voltage of 11kV but significant with reference to the true fault voltage of only a few hundred volts. The large error for short arc lengths is therefore not a major concern. The accuracy of the algorithm is therefore acceptable for all conditions.

7.2.4 Influence of distance to fault on the accuracy of the algorithm

Radojevic *et. al.* tested the accuracy of the their algorithm over a wide range of distances to fault [6]: the accuracy of their distance to fault algorithm was within 5% for distances up to 290km and fault resistances smaller than 10Ω. The accuracy decreased dramatically for large fault resistances. For networks with supplies at both ends of the line, remote in feed into the fault will also cause a decrease in the accuracy [6]. Distribution networks are mostly radial fed networks and remote infeeds are not expected to play a major role in the accuracy of the algorithm. No accuracy test has yet been done on the estimated arc voltage over a wide range of distance to faults. The network shown by Figure 7.1 was used with a constant arc length of 1.0m to examine accuracy of arc voltage estimation. It has already been shown in the previous paragraphs of section 7.2 that accuracy decreases as the ratio between the fault current and the load currents decreases. The load currents were therefore reduced to less than 1A to exclude the influence of the different branch load currents. The measuring points for evaluation purposes were kept at a third and

two thirds of the distance to fault as well as at the fault position. The results of this set of simulations are shown in Table 7.3.

Table 7.3: Accuracy of voltage estimation for various distances to fault.

Distance to fault (km)	*Fault current*	*Error of estimated Voltage (rms) at*		
		A	*B*	*F*
3	1179A	1.71%	4.16%	5.07%
6	852A	1.41%	3.94%	5.00%
9	667A	1.25%	3.74%	4.93%
12	548A	1.07%	3.60%	4.87%
15	465A	1.13%	3.61%	4.98%
18	404A	1.06%	3.46%	4.88%
21	357A	1.01%	3.34%	4.82%

Figure 7.1 define position A, B and F. All line elements shown in Figure 7.1 were the length shown in the column above. The fault consists of a 1m long arc between phase and ground.

The results indicate the independence of the accuracy of the algorithm to the distance to fault. The error in the estimation is roughly constant at a specific point for the various distances that were simulated. The same simulations were done for high load currents for a distance to fault of 21km. The loads are simulated using constant impedances. The load currents were set to be 40% of the fault current while the fault was present on the network. The branch load currents at point A and B were 108A and 93A respectively (Figure 7.1) while the fault current was simulated to be only 261A, which is a condition that would be rather unusual in practice where fault currents would be significantly greater than load current. The accuracy of the algorithm for these conditions reduces dramatically. For the simulation the error in the voltage estimation at the point of fault increases to -21% while the errors at point A and B increase to –8% and –4% respectively. The accuracy of this voltage estimation algorithm is still acceptable for distances away from the fault of a third of the distance to fault.

7.2.5 Limitations of proposed method

This three-phase differential equation algorithm is derived using the equivalent single-phase sequence component circuit shown by Figure 3.6. The algorithm also makes use of the assumption that the sequence current components are constant between the feeder and the point of fault. This is however not the case in some distribution lines with “teed” networks. The positive sequence current will start off

large at the feeder but disperse to loads and down "tees" along the line. This wrong assumption starts to become significant for small fault currents.

Fault levels on the end of long distribution lines are low. These lines also tend to have a lot of teed points. The effect of these long lines with "tees" along the lines was studied by using the network circuit shown in Figure 7.1. The lengths of the lines were increased from 2km to 30km each. A fault is therefore simulated at the end of a 90km lines. The loads in Figure 7.1 were change to produce load currents of 50A under normal operating conditions. The fault was simulated as an arc with a length of 200mm and is grounded through an earthing resistance of 3Ω.

This simulation show that under normal operating conditions a voltage drop of 10% exists from the feeder to the end of the line. The voltage drops however from 5530V to 467V at the end of the line after the fault was incepted. The algorithm made an estimation error of 213%. The estimation voltage levels 30km and 60km from the fault was however more accurate with a 11.5% and 2.8% error at the respective positions. The true and estimated waveforms are shown in Figure 7.4.

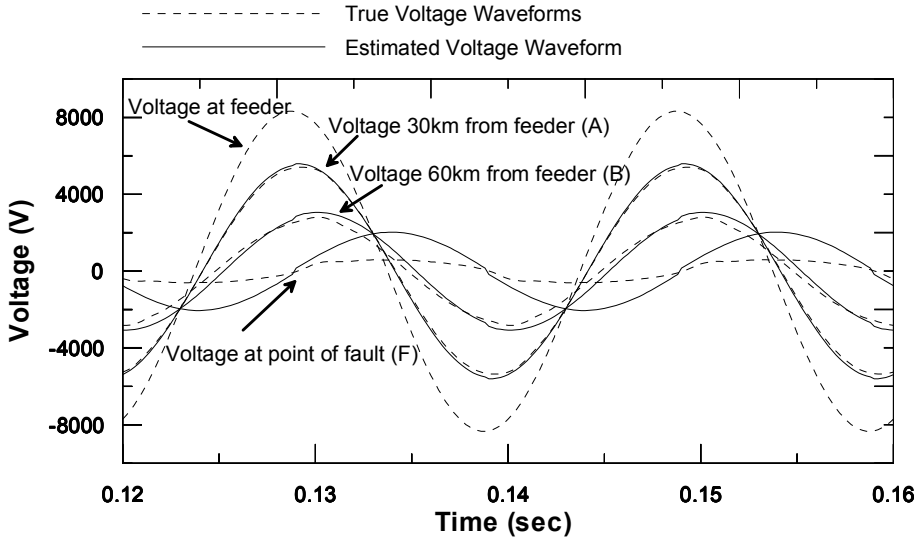

Figure 7.4: Estimated and true voltage at various distances from the fault on a 90km long line. The fault consists of a 200mm long arc and a 3Ω footing resistance.

The voltage was overestimated at the point of fault. The amplitude of the arc voltage was more accurately calculated but the resistance estimated was as too big. The reason for this over estimation of the fault resistance is the load currents splitting at

the “teed”-points. The over estimation of the fault resistance causes the over estimation of the voltage at the point of fault. Assuming a fault voltage of 0V would have provided more accurate results.

Faults at the end of long lines will have very low voltages due to the high impedance of the long line. This high source impedance will cause the voltage at the faulted point to be very low. The proposed algorithm can therefore not be applied on long lines except if most of the loads are at the end of the line. The main usage of the algorithm will be on short lines with high fault levels.

7.3 Improvement of Fault Location by “Triangulation” in teed networks

One of the primary assumptions made in the previous section was that the actual fault current path is known. However, most distribution networks are radially fed, “teed” circuits and a distance to fault measurement will not give an indication in which of the branches the fault occurs. The fault can occur at any of the branches with a distance of at least equal to the distance to fault measured. It is therefore not possible to estimate the voltage level at different positions of a radial feeder without knowing the exact position of the fault.

This section investigates a possible method determining more precisely position of faults in a medium voltage networks. It will be assumed that the voltage at the end of the main branch is known, and thereby making it possible to calculate the distance to the tee-off of the faulted branch.

7.3.1 Basic philosophy of method

The installation of modern re-closers [73] with on board voltage transducers and radio communications makes it possible to relay the voltage at that specific point back to the substation feeder. If the re-closer is installed along the main branch beyond the fault point, this information can be used to determine in which sub-branch the fault has occurred, narrowing down the location of the fault dramatically.

Figure 7.5 shows a typical single line diagram of a medium voltage radial fed distribution network.

The distance between feeder A and the faulted branch tee-off point C can be estimated if the voltage drop between point A and point C is known. The voltage at point D during the fault can be transmitted back to the substation or feeder at point A if a recloser is installed at point D. The change in voltage between point C and D is mainly by load current. This voltage drop should be relatively small with reference to the nominal system voltage for an average loaded network. A good estimation of the distance to the faulted tee-off point C can be made by sending the voltage at point D back to the relay at the feeder / substation and assuming that the voltage at the faulted teed is equal to this value. The distance to fault can be estimated with a standard fault locator algorithm using a voltage value equal to the difference in the measured voltage at point A and point D. This distance can be used to determine on which branch the fault may have occurred. It will now be possible to calculate the exact position of the fault if this philosophy is used. It will also be possible to calculate the dips and sags on the total MV feeder during the fault, using the method described in section 7.2, if the fault position is known.

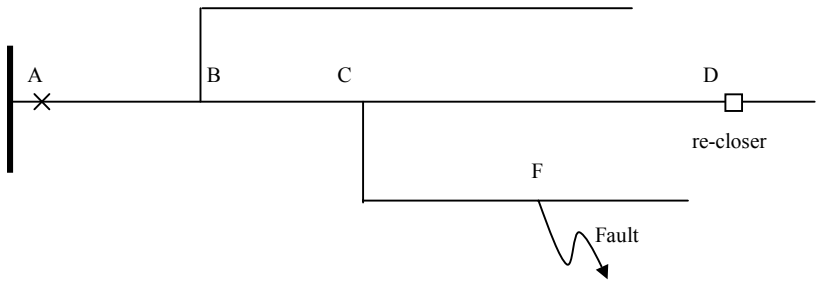

Figure 7.5: A typical radial fed distribution network with a fault at point F

7.3.2 Simulation model for testing of method

Figure 7.6 shows the distribution circuit that was simulated to test the accuracy of the estimation from the feeder to the tee-off point. Again, Table 3.1 gives the detail of the line parameters and voltage source.

This method was tested for both a single phase to ground and a phase-to-phase fault. The faults were simulated as a 1m long arc in the middle of the indicated line (Figure 7.6). The tests were conducted over a wide range of loading conditions. The loads (Load B and Load D) were increased to values that are at least 50% of the fault current. These are extreme conditions, which is used as the worst-case scenario. It can be safe to assume that a fault current will always be significant larger than the load current and that the probability of these worst-case scenarios are very small.

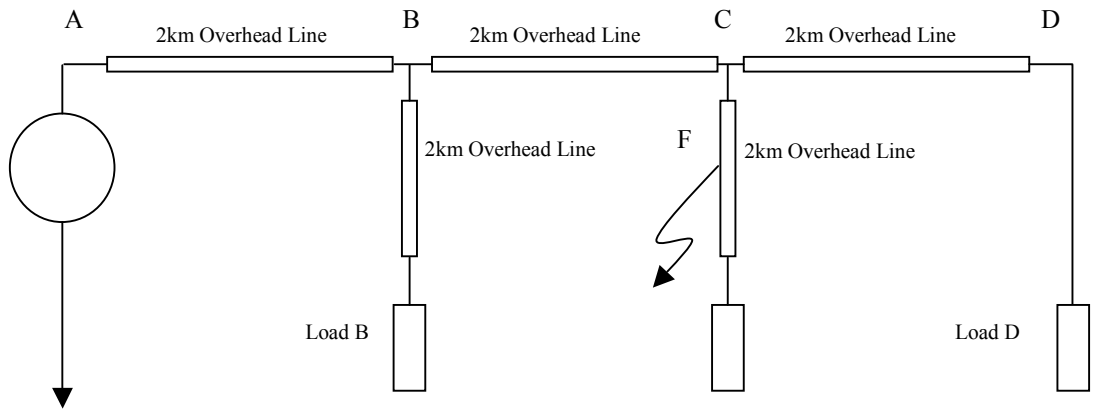

Figure 7.6: Single-line schematic diagram of teed distribution network with a single-phase to ground fault at point F.

7.3.3 Results of Simulations

Table 7.4 gives the results of the simulation for phase to ground faults. Load B was kept constant for the first set of tests. For the second set of tests Load D was again kept constant on what was assumed to be a realistic current (150A) while Load B was increased. The results of the phase-to-phase faults are given in Table 7.5.

Table 7.4: Estimation error for the distance to faulted tee-of position for single-phase to ground faults (bolted fault). Position B, F and D is defined by Figure 7.6.

Amplitude of current to Loads during fault			*Estimated*	*Error (%)*
Load B	*Fault F*	*Load D*	*distance to tee*	
9A	932A	8A	4.0001	0
9A	927A	38A	4.0155	0.4%
9A	917A	74A	4.0351	0.9%
9A	893A	181A	4.0937	2.3%
9A	837A	344A	4.1926	4.8%
8A	708A	599A	4.3990	10.0%
40A	887A	181A	4.0783	2.0%
78A	880A	180A	4.0599	1.5%
361A	802A	167A	3.9028	-2.4%
631A	686A	147A	3.7005	-7.5%

Table 7.5: Estimation error for the distance to faulted tee-of position for phase-to-phase faults. (bolted fault). Position B, F and D is defined by Figure 7.6.

Amplitude of current to Loads during fault			*Estimated*	*Error (%)*
Load B	*Fault F*	*Load D*	*distance to tee*	
9A	1152A	8A	4.0009km	0%
9A	1156A	37A	4.0095km	0.2%
9A	1149A	73A	4.0204km	0.5%
8A	1132A	176A	4.0526km	1.3%
7A	1103A	318A	4.1026km	2.6%
6A	1047A	497A	4.2009km	5.0%
4A	869A	698A	4.4977km	12.4%
8A	1132A	176A	4.0526km	1.3%
35A	1128A	174A	4.0432km	1.1%
68A	1124A	172A	4.0322km	0.8%
161A	1109A	164A	3.9982km	0%
289A	1082A	150A	3.9424km	-1.4%
460A	1020A	123A	3.8298km	-4.3%

7.3.4 Discussion

The results indicate a maximum estimation error of 12%. The load current flowing through the re-closer tends to increase the estimated distance while the current flowing to loads between the faulted branch and the feeder decreases the estimated distance. This tends to reduce the overall error. Therefore, distance estimations for faults on branches near to the feeder will tend to be an over estimation since most of the load current flows past the faulted branch tee-off. Distance estimations for faults near the end of feeder line will tend to be under estimated since most of the load current never reaches the tee-off of the faulted branch.

This method will not suit all distribution line topologies. The most important requirement for using this method is to ensure that the distances between the tee-offs of the different branches are large enough. Two tee-offs in close proximity might cause confusion since the algorithms output is not exact. Lightly loaded lines will further be more suitable for this application than heavy overloaded lines.

The voltage signal from the remote end needs to be transmitted and synchronised to the voltage signal at the feeder. This type of technology is already used on transmission systems as an answer to the feedback problem on fault locators as discussed in the literature review. The technology for this proposal therefore already exists.

7.4 Conclusion

A method was introduced which can be used to estimate the supply voltage of different consumers on a single MV feeder circuit during fault conditions. This algorithm can be a valuable tool for utility companies to determine the actual voltage dip at any point of the network should a fault occur somewhere on the distribution network. The results indicate accurate estimations that include the actual wave shape of the supply voltage. It was shown that the method has limitations in estimating the fault voltage for long distribution lines. The reason for these limitations are (i) the currents flowing into the braches although the algorithm assumes that the total measured current flows up to the point of fault and (ii) the long line reduces the fault current causing the load current flowing in the branches to be more dominant than for short lines.

The method assumes a recloser at the end of the main branch. Sub-branches normally do not have any reclosers. It will not be possible to determine the position of the fault should there be a tee on the sub branch. However, such branches are normally short and will not have a major influence on the accuracy of the voltage estimation.

A second problem with this method is that the exact fault current route along the radially fed, branched distribution network is unknown. By using line voltage measured by modern reclosers with voltage measuring capabilities and communication links a new method is proposed to detect the sub-branch containing the fault. It was shown that the proposed method in the calculation of the distance to the tee-off position of the faulted branch is relatively accurate. This algorithm can therefore be used to estimate the actual fault current route in the MV network.

8. SUMMARY

The aim of this thesis has been to investigate the influences of fault arcing on time domain fault locator algorithms as well as to look into the possibilities of using the properties of an arc fault to identify specific fault conditions. The work was, however, expanded to include an investigation into the influence of magnetic forces during faulted conditions on the accuracy of impedance type fault locator algorithms. Finally, an existing fault locator algorithm was used to test the possibility of using it in estimating the voltage level on a faulted distribution line for power quality monitoring purposes.

8.1 Influences on the accuracy of impedance type fault locator algorithms

A fourth technique for deriving differential equation fault locator algorithms was introduced by the use of a convolution operator. Two algorithms were derived using this new technique. The first algorithm was derived using an array of impulse functions that simulate the measured voltage signal. A second algorithm was derived using a piece-wise linear voltage signal.

Both the algorithms were tested on a single-phase circuit that uses a PI-model distribution line. It was shown that large fault resistances have a negative influence on the algorithm. The accuracy of the algorithms did not change for sampling periods shorter than 0.3ms but decrease rapidly for longer sampling periods.

The algorithm derived from the impulse functions was successfully transformed to a three-phase circuit by the use of an equivalent single-phase sequence component circuit for a phase-to-ground and phase-to-phase fault. This algorithm does not require the use of matrix calculations as required by the existing algorithms for three-phase circuits. Simulation tests show that the accuracy of this algorithm is much less dependent on the fault resistance than the equivalent single-phase circuit. The reason for this is that the algorithms for the single-phase circuit ignores the line charging

current while the three-phase algorithm includes the line charge current in the calculation of the zero-sequence current.

The algorithm also shows a high level of independency from load current during a single-phase to ground fault if all the loads' neutrals are ungrounded. The simulations showed an error in the distance estimation of only 1.6% for a fault current of 200A and load current of 620A on a 20km long medium voltage line. This independency from the load current is only valid for phase-to-ground fault. A second requirement is that no neutral on the load side of the network is allowed to be grounded.

The standard differential equation algorithm is however unstable and inaccurate under arc fault conditions. This inaccuracy is caused by the variation in the arc resistance during the current zero periods. A 40^{th} order median filter was used to increase the stability. The standard deviation of the fault locator algorithm output, for a fault on a 20km line with a 2m long arc, decrease form 40% to 9% while the error in the distance estimation decrease from 40% to 10% with the inclusion of this filter.

The differential equation type algorithm proposed by Radojevic *et.al.* [2], that estimates the fault arc voltage as a square wave and uses the least square method as parametric resolution technique, produces much better results under fault arcing. This algorithm produces errors smaller than 7% with a negligibly small standard deviation for a 2m long arc fault on a 20km line. The standard deviation of the distance estimation only becomes significant for arc length variations greater than 10m/s. For an increase in arc length of 18m/s, it is expected that the standard deviation of the distance estimation is still smaller than 2%.

A phase-to-phase fault will cause large current in opposite directions in the two faulted conductors that will produce an opposing magnetic field. This magnetic field will force the conductors away from each other and changing the geometric distance between the conductors. A finite element analysis based on existing wave equations indicated that a line using Grape conductor with a ruling span of 80m and conductor spacing of 750mm can expect a maximum deflection of 0.8m during a phase-to-

phase fault current of 12kA. This deflection will change the inductance of the line and cause an estimation error of up to 12% in impedance type fault locator. The parameters that will influence the deflection are the initial cable tension, span length, conductor spacing and fault level. The fault locator algorithm will under estimate the distance to fault due to the increase of the true inductance.

8.2 Monitoring of Overhead Lines

The two broken end points of a breaking conductor accelerate away from one another due to gravitation and retraction of the stretched line. It was shown that the acceleration of the broken end due to gravitation is negligibly small and could be ignored. A typical retraction speed for ACSR conductors if tensioned to 25% of the UTS is 7.5m/s and this speed is reached within 8.6ms for a 120m span length. The final speed is however highly dependent upon the initial tension in the cable while the time required for reaching the final speed is dependent on the total length of the span. The broken ends will have a constant speed after this initial acceleration since stiffness will have no effect on the conductor for the first few meters of travel.

Two algorithms were derived using this constant increase in arc length as the unique property to identify a broken conductor. The first technique uses the increase in arc voltage while the second technique uses the increase in non-linear properties of the arc resistance due to the arc length increase. The linearity of the arc length increase was tested by calculating the correlation coefficient of either the arc voltage estimation or the maximum wavelet coefficients of the network resistance during the current zero periods. Both these techniques were successfully simulated on a breaking Banana conductor on a 11kV distribution network. It was shown that the algorithms were able to detect a breaking conductor under normal operating conditions and line-to-ground arc fault conditions.

Clashing conductors due to wind forces were also simulated using the same finite element model as described in Section 6.1. The simulations indicate that the separation speed of the conductor is highly variable depending on the initial line tension, span length, fault level and conductor mass. This highly variable separation speed of the conductor makes it impossible to identify a clashing conductor using the

same technique described for detecting a breaking conductor. The simulations indicated that there is a small possibility that the proposed algorithm for detecting a breaking conductor might wrongly identify a clashing conductor as a breaking conductor. Under certain special conditions it might happen that the arc length increases after conductor clashing is equal to that of a breaking conductor and that this speed is almost constant for a small period of time. This will however only occur under phase-to-phase fault conditions while a conductor can break under any normal or fault condition.

Radojevic's equation was also used to determine the voltage at the point of fault. The voltage level in the rest of the network can be estimated using a linear relationship between the voltage and distance from the measuring point to the position of the fault. The simulations indicated voltage estimation errors smaller than 2.3% for a fault at the end of a 6km distribution line. The error in the voltage estimation of the arc voltage increased to 26% for a 250mm long arc. The small true fault voltage mainly causes this large percentage error.

The estimation of the fault voltage at the end of very long lines (90km) is very inaccurate. The main reason for this inaccurate estimation is the loads along the line. Inaccuracies are worst when the fault current on such long lines is comparable to the load current. The algorithm assumes that the measured current flows at least up to the fault. This assumption is however more inaccurate on long lines with distributed loads along the line than for short lines.

8.3 Further Work

In the author's opinion, experimental work should be done on the detection of breaking conductor. The proposed algorithm was derived from pure theoretical simulations. Both mechanical cable failure as well as electrical arc testing during the cable failure is required for further development of the algorithm.

It was also shown that conductor clashing cannot be identify on the increase in the arc length alone. The detection of conductor clashing requires further experimental work to determine if a horizontal, travelling arc, have some special characteristics

that can be used in identifying conductor clashing. The experimental work should focus on arc length variations caused by the extra convection cooling due to the high travelling speed of the arc between the two horizontal conductors.

APPENDIX I: DERIVATION OF ALGORITHMS

Derivation of Differential Type Fault Locator Algorithms for single-phase network

The overhead line is modelled as an inductor in series with a resistance. Line capacitance is ignored to simplify the derivation of the algorithm.

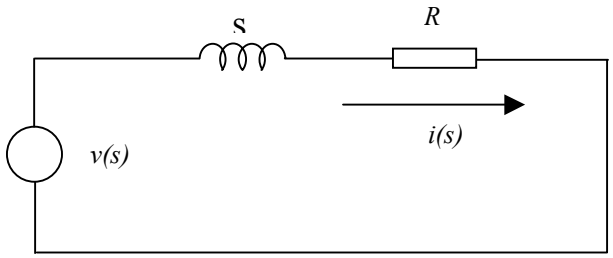

Figure A1.1: A R-L Series circuit modelling an overhead line.
The fault resistance is included in the resistance *R*.

The current *i(s)* in the circuit shown by Figure A1.1 can be calculated for a voltage *v(s)*, circuit resistance *R* and inductance *L* using Equation (A1.1).

$$i(s) = \frac{v(s)}{R + sL} = \left(\frac{1}{L}\right)\left(\frac{1}{R/L + s}\right)v(s) \tag{A1.1}$$

Equation (A1.2) is obtained by inverting Equation (A1.1)

$$\mathcal{L}^{-1}\{i(s)\} = \mathcal{L}^{-1}\left\{\left(\frac{1}{L}\right)\left(\frac{1}{R/L + s}\right)v(s)\right\}$$

$$i(t) = \left(\frac{1}{L}e^{-\frac{t}{L/R}}\right) \otimes v(t) \tag{A1.2}$$

Equation (A1.2) describes the relationship between the voltage and current signal using a convolution operator. This equation needs to be simplified even further before it can be used as a fault locator algorithm and Equation (A1.2) can be simplified further if the voltage waveform is known.

The voltage signal will firstly be estimated as an array of impulse functions and secondly as a linear function.

Estimating the voltage signal as an array of impulses

The standard convolution operation in the discrete form is given by equation (A1.3) [63]:

$$i(\lambda_n) = \sum_{i=0}^{n} h(\lambda_n - \lambda_i) \cdot \Delta\lambda \cdot v(\lambda_i) \tag{A1.3}$$

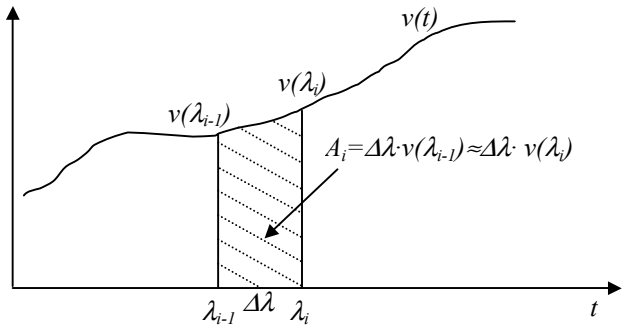

Figure A1.2: Area A_i of impulse function for voltage estimation

The standard convolution equation [63] can also be written as shown in Equation (A1.4) using alternative samples in calculating the area shown in Figure A1.2. Equation (A1.3) used the voltage at sample *i* to calculated the area A_i while Equation (A1.4) uses the *i-1* sample to calculate the same area (Figure A1.2).

$$i(\lambda_n) = \sum_{i=0}^{n} h(\lambda_n - \lambda_i) \cdot \Delta\lambda \cdot v(\lambda_{i-1}) \tag{A1.4}$$

The simulations showed that the algorithm derived from Equation (A1.3) is less accurate than the algorithm derived from Equation (A1.4) at high fault resistances. Equation (A1.4) was therefore used to derive the required algorithm.

The transfer function described by Equation (A1.2) is substituted into Equation (A1.4) to obtain Equation (A1.5). In Equation (A1.5), the time constant is defined as $\tau = L/R$.

$$i(\lambda_n) = \sum_{i=0}^{n} \left(\frac{1}{L}\right) e^{-\frac{\lambda_n - \lambda_i}{\tau}} \cdot \Delta\lambda \cdot v(\lambda_{i-1}) \tag{A1.5}$$

The summation in Equation (A1.5) can be expanded as shown in Equation (A1.6)

$$i(\lambda_n)=\left(\frac{1}{L}\right)e^{-\frac{\lambda_n-\lambda_n}{\tau}}\cdot\Delta\lambda\cdot v(\lambda_{n-1})+\sum_{i=0}^{n-1}\left(\frac{1}{L}\right)e^{-\frac{\lambda_n-\lambda_i}{\tau}}\cdot\Delta\lambda\cdot v(\lambda_{i-1}) \tag{A1.6}$$

Equation (A1.6) assumes that the voltage estimated impulses are evenly spaced. This will be true if the sampling frequency of the fault locator is constant.

$$\lambda_n=\lambda_{n-1}+\Delta\lambda \tag{A1.7}$$

Equation (A1.6) is simplified further by substituting Equation (A1.7) into Equation (A1.6).

$$i(\lambda_n)=\left(\frac{1}{L}\right)e^{-0}\cdot\Delta\lambda\cdot v(\lambda_{n-1})+\sum_{i=0}^{n-1}\left(\frac{1}{L}\right)e^{-\frac{\Delta\lambda+\lambda_{n-1}-\lambda_i}{\tau}}\cdot\Delta\lambda\cdot v(\lambda_{i-1})$$

$$i(\lambda_n)=\left(\frac{1}{L}\right)\Delta\lambda\cdot v(\lambda_{n-1})+\left(\sum_{i=0}^{n-1}\left(\frac{1}{L}\right)e^{-\frac{\lambda_{n-1}-\lambda_i}{\tau}}\cdot\Delta\lambda\cdot v(\lambda_{i-1})\right)e^{-\frac{\Delta\lambda}{\tau}} \tag{A1.8}$$

Equation (A1.9) is obtained by re-writing Equation (A1.4) to describe the current at time $t=\lambda_{n-1}$.

$$i(\lambda_{n-1})=\sum_{i=0}^{n-1}\left(\frac{1}{L}\right)e^{-\frac{\lambda_{n-1}-\lambda_i}{\tau}}\cdot\Delta\lambda\cdot v(\lambda_{i-1}) \tag{A1.9}$$

Equation (1.8) can now be written as a function of the transfer function and the last two sampled currents as well as voltage by replacing Equation (A1.9) into the second term of Equation (A1.8). The result of this simplification is shown in equation (A1.10)

$$i(\lambda_n)=\left(\frac{1}{L}\right)\cdot\Delta\lambda\cdot v(\lambda_{n-1})+(i(\lambda_{n-1}))e^{-\frac{\Delta\lambda}{\tau}} \tag{A1.10}$$

Assuming that the current and voltage signals are sampled at time $t=\lambda_n$ and $t=\lambda_{n-1}$, the variables v_k and v_{k-1} represent the voltage samples while i_k and i_{k-1} represent the current samples. These variables can be used in Equation (A1.10) to obtain Equation (A1.11).

$$i_k=i_{k-1}e^{-\frac{\Delta t}{L/R}}+\frac{1}{L}\Delta t\cdot v_{k-1} \tag{A1.11}$$

A second set of samples (v_k, v_{k+1}, i_k and i_{k+1}) was used to obtain Equation (A1.12)

$$i_{k+1}=i_ke^{-\frac{\Delta t}{L/R}}+\frac{1}{L}\Delta t\cdot v_k \tag{A1.12}$$

Equation (A1.11) can be re-written as:

$$e^{-\frac{\Delta t}{L/R}}=\frac{1}{i_{k-1}}\left(i_k-\frac{1}{L}\Delta t\cdot v_{k-1}\right) \tag{A1.13}$$

Equation (A1.13) can be replaced back into Equation (A1.12) to calculate the inductance L.

$$i_{k+1} = i_k \left\{ \frac{1}{i_{k-1}} \left(i_k - \frac{1}{L} \Delta t \cdot v_{k-1} \right) \right\} + \frac{1}{L} \Delta t \cdot v_k$$

$$i_{k+1} = \frac{i_k \cdot i_k}{i_{k-1}} - \frac{\Delta t \cdot v_{k-1} \cdot i_k}{L \cdot i_{k-1}} + \frac{1}{L} \Delta t \cdot v_k$$

$$\frac{\Delta t}{L} \left(\frac{v_{k-1} i_k}{i_{k-1}} - v_k \right) = \frac{i_k i_k}{i_{k-1}} - i_{k+1}$$

$$\frac{\Delta t}{L} \left(\frac{v_{k-1} i_k - v_k i_{k-1}}{i_{k-1}} \right) = \frac{i_k i_k - i_{k+1} i_{k-1}}{i_{k-1}}$$

$$L = \Delta t \cdot \left(\frac{v_{k-1} i_k - v_k i_{k-1}}{i_k i_k - i_{k+1} i_{k-1}} \right) \tag{A1.14}$$

The total inductance L is the product of the total length ℓ and the inductance per unit length L_e.

$$L = \ell \times L_e \tag{A1.15}$$

This relationship can be used to calculate the actual distance to fault. Equation (A1.16) is obtained by replacing Equation (A1.15) into Equation (A1.14).

$$\ell = \frac{\Delta t}{L_e} \left(\frac{v_{k-1} i_k - v_k i_{k-1}}{i_k i_k - i_{k+1} i_{k-1}} \right) \tag{A1.16}$$

Equation (A1.16) is the final equation for the algorithm that can be used to estimate distance to fault on an equivalent single-phase circuit.

Assuming that the voltage signal is linear signal during a sampling period

Equation (A1.17) gives the transfer function that relates the current to the voltage in Figure A1.1 and is derived from Equation (A1.2):

$$h(t) = \frac{1}{L} e^{-\frac{t}{L/R}} = \frac{1}{L} e^{-\frac{t}{\tau}} \tag{A1.17}$$

The voltage signal is assumed to be piece-wise linear function using equation (A1.18) as approximation. This approximation is shown in Figure A1.3.

$$v(t) = m_v (t - t_0) + c \tag{A1.18}$$

In Equation (A1.18), the constant m_v represents the voltage gradient between two samples and the c represents the voltage at time $t = t_0$.

The convolution function will only be taken during the data window with a Δt period. Normally it is assumed that the voltage signal starts at time $t = 0$. In this case, however, it will be assumed that the voltage signal started in the past when $t = -\infty$, and the evaluation period is from $t = -\infty$ to $t = \Delta t$. In effect it is assumed that $t_0 = 0$. This assumption was made to simplify the convolution operation. Figure A1.3 shows the assumptions graphically.

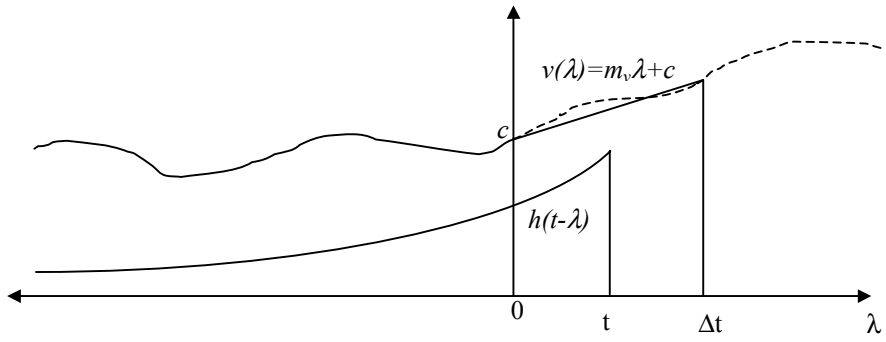

Figure A1.3: Convolution of linear estimated voltage signal and transfer function

The current can be described by the following convolution equation:

$$i(t) = \int_0^t h(t-\lambda)\cdot v(\lambda)d\lambda + \int_{-\infty}^0 h(t-\lambda)\cdot v(\lambda)d\lambda$$

$$i(t) = \int_0^t \left(\frac{1}{L}e^{-\frac{t-\lambda}{\tau}}\right)(m_v\lambda + c)d\lambda + \int_{-\infty}^0 h(t-\lambda)\cdot v(\lambda)d\lambda \qquad \text{(A1.19)}$$

The current at $t = 0$ is considered to be known as a sample is taken at this point. It is assumed that this current is i_{k-1}. The current due to the voltage up to time 0 will have a natural decay with the same time constant as the defined transfer function. The second term on the right hand side is therefore replaced by this naturally-decaying current component. The mathematical derivation is the same as the derivation of the second term of Equation (A1.10).

$$i(t) = \left(\frac{1}{L}e^{-\frac{t}{\tau}}\right)\times\int_0^t \left(m_v\lambda e^{-\frac{\lambda}{\tau}} + ce^{-\frac{\lambda}{\tau}}\right)d\lambda + i_{k-1}e^{-\frac{t}{\tau}}$$

$$i(t)=\left(\frac{1}{L}e^{-\frac{t}{\tau}}\right)\times\left(m_v\tau e^{\frac{\lambda}{\tau}}(\lambda-\tau)+\tau c e^{\frac{\lambda}{\tau}}\right)\Bigg|_0^t+i_{k-1}e^{-\frac{t}{\tau}}$$

$$i(t)=\left(\frac{1}{L}e^{-\frac{t}{\tau}}\right)\times\left(m_v\tau e^{\frac{t}{\tau}}(t-\tau)+\tau c e^{\frac{t}{\tau}}-m_v\tau e^{\frac{0}{\tau}}(0-\tau)-\tau c e^{\frac{0}{\tau}}\right)+i_{k-1}e^{-\frac{t}{\tau}}$$

$$i(t)=\left(\frac{1}{L}e^{-\frac{t}{\tau}}\right)\times\left(m_v\tau e^{\frac{t}{\tau}}(t-\tau)+\tau c e^{\frac{t}{\tau}}+m_v\tau^2-\tau c\right)+i_{k-1}e^{-\frac{t}{\tau}}$$

The next set of samples will be taken at $t = \Delta t$. This set of samples is defined as sample number k.

$$i_k=i(\Delta t)=\left(\frac{1}{L}e^{-\frac{\Delta t}{\tau}}\right)\times\left(m_v\tau e^{\frac{\Delta t}{\tau}}(\Delta t-\tau)+\tau c e^{\frac{\Delta t}{\tau}}+m_v\tau^2-\tau c\right)+i_{k-1}e^{-\frac{\Delta t}{\tau}}$$

$$i_k-i_{k-1}e^{-\frac{\Delta t}{\tau}}=\frac{1}{L}\left(m_{v(k-1)}\tau\Delta t+\left(\tau c_{k-1}-m_{v(k-1)}\tau^2\right)\left(1-e^{-\frac{\Delta t}{\tau}}\right)\right) \qquad \text{(A1.20)}$$

A second equation can also be calculated using the same method for sample points k and $k+1$. This equation is:

$$i_{k+1}-i_k e^{-\frac{\Delta t}{\tau}}=\frac{1}{L}\left(m_{v(k)}\tau\Delta t+\left(\tau c_k-m_{v(k)}\tau^2\right)\left(1-e^{-\frac{\Delta t}{\tau}}\right)\right) \qquad \text{(A1.21)}$$

Both these two equation (A1.20) and (A1.21) can be divided into each other to eliminate the unknown inductance. The resulting equation will have only one unknown variable, which is the time constant τ.

$$\frac{i_{k+1}-i_k e^{-\frac{\Delta t}{\tau}}}{i_k-i_{k-1}e^{-\frac{\Delta t}{\tau}}}=\frac{m_{v(k)}\tau\Delta t+\left(\tau c_k-m_{v(k)}\tau^2\right)\left(1-e^{-\frac{\Delta t}{\tau}}\right)}{m_{v(k-1)}\tau\Delta t+\left(\tau c_{k-1}-m_{v(k-1)}\tau^2\right)\left(1-e^{-\frac{\Delta t}{\tau}}\right)}$$

$$\left(i_{k+1}-i_k e^{-\frac{\Delta t}{\tau}}\right)\left(m_{v(k-1)}\tau\Delta t+\left(\tau c_{k-1}-m_{v(k-1)}\tau^2\right)\left(1-e^{-\frac{\Delta t}{\tau}}\right)\right)$$

$$-\left(i_k-i_{k-1}e^{-\frac{\delta t}{\tau}}\right)\left(m_{v(k)}\tau\Delta t+\left(\tau c_k-m_{v(k)}\tau^2\right)\left(1-e^{-\frac{\Delta t}{\tau}}\right)\right)=0$$

Above equation can be used to determine the time constant τ. The time constant is substituted back into Equation (A1.20) or Equation (A1.21) to determine the inductance from the point of measurement to the fault.

Derivation of differential equation type fault locator algorithm for three phase systems

Figure A1.4 describe the equivalent single-phase circuit for a single-phase to ground fault on a three phase system.

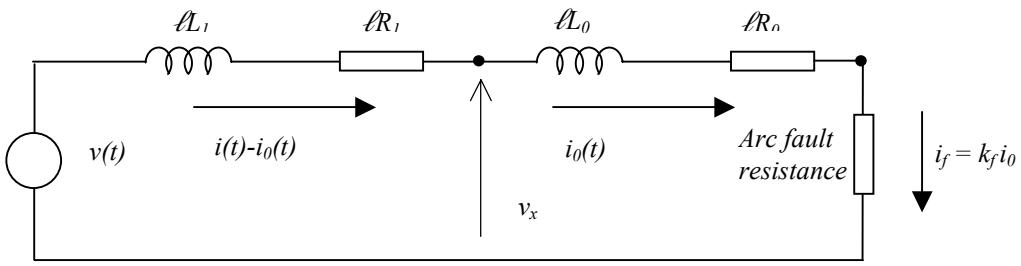

Figure A1.4: Equivalent single-phase circuit for a single-phase to ground fault on a three phase network.

Equation (A1.22) and (A1.23) is derived from Figure A1.4 using the voltage-current relationship described by Equation (A1.11).

$$i_{k+1} - i_{0_{k+1}} = \left(i_k - i_{0_k}\right)e^{-\frac{\Delta t}{\tau_1}} + \left(\frac{\Delta t}{\ell L_1}\right)\left(v_k - v_{x_k}\right) \tag{A1.22}$$

$$i_{0_{k+1}} = i_{0_k} e^{-\frac{\Delta t}{\tau_0}} + \left(\frac{\Delta t}{\ell L_0}\right) v_{x_k} \tag{A1.23}$$

Equation (A1.23) can be re-written as:

$$v_{x_k} = \left(\frac{\ell L_0}{\Delta t}\right)\left(i_{0_{k+1}} - i_{0_k} e^{-\frac{\Delta t}{\tau_0}}\right) \tag{A1.24}$$

Equation (A1.24) can be substituted back into equation (A1.22).

$$i_{k+1} - i_{0_{k+1}} = \left(i_k - i_{0_k}\right)e^{-\frac{\Delta t}{\tau_1}} + \left(\frac{\Delta t}{\ell L_1}\right)\left(v_k - \left(\frac{\ell L_0}{\Delta t}\right)\left(i_{0_{k+1}} - i_{0_k} e^{-\frac{\Delta t}{\tau_0}}\right)\right)$$

$$\left(i_{k+1} - i_{0_{k+1}}\right) - \left(i_k - i_{0_k}\right)e^{-\frac{\Delta t}{\tau_1}} = \left(\frac{\Delta t}{\ell L_1}\right) v_k - \frac{L_0}{L_1}\left(i_{0_{k+1}} - i_{0_k} e^{-\frac{\Delta t}{\tau_0}}\right)$$

$$\left(i_{k+1} - i_{0_{k+1}}\right) - \left(i_k - i_{0_k}\right)e^{-\frac{\Delta t}{\tau_1}} + \left(\frac{L_0}{L_1}\right)i_{0_{k+1}} = \left(\frac{L_0}{L_1}\right)i_{0_k}e^{-\frac{\Delta t}{\tau_0}} + \left(\frac{\Delta t}{\ell L_1}\right)v_k \qquad \text{(A1.25)}$$

Equation (A1.25) can be re-written in a more familiar way as used in the derivation of the single-phase algorithm. This simplified equation is shown be Equation (A1.26).

$$p_{k+1} = q_k e^{-\frac{\Delta t}{L/R}} + \frac{1}{\ell L_1}\Delta t \cdot v_k \qquad \text{(A1.26)}$$

where

$$p_{k+1} = \left(i_{k+1} - i_{0_{k+1}}\right) - \left(i_k - i_{0_k}\right)e^{-\frac{\Delta t}{\tau_1}} + \left(\frac{L_0}{L_1}\right)i_{0_{k+1}}$$

$$q_{k+1} = \left(\frac{L_0}{L_1}\right)i_{0_k}$$

$$\tau_1 = \frac{L_1}{R_1}$$

The distance to fault is calculated in the same way as shown by the derivations from Equations (A1.11) to (A1.15). The final equation to be used as the distance to fault algorithm is given by equation (A1.27).

$$\ell = \frac{\Delta t}{L_1}\left(\frac{q_{k+1}v_{k-1} - q_k v_k}{p_k q_{k+1} - p_{k+1}q_k}\right) \qquad \text{(A1.27)}$$

APPENDIX II: DYNAMICS OF BREAKING CONDUCTORS

Derivation of equations describing the dynamic properties of a overhead line conductor after breaking.

When a conductor breaks, gravitation and elastic forces will tend to cause the ends of the conductor to accelerate away from each other due to elastic and gravitational forces. These two causes of movement of the conductor will be investigated independently. Some dependency will exist between the two movements. However, it is believed that the acceleration due to elasticity will dominate the movement, making the gravitational acceleration negligible small.

Displacement caused by gravitation:

It is assumed that the conductor breaks in the centre of the span. The conductor is horizontal at the midpoint. The only forces that have an influence on the dynamics of the end point of the conductor is the horizontal force due to the forces the cable on the end element as well as the vertical gravitational forces. The line element should therefore not be able to turn since no momentum exists on the line element.

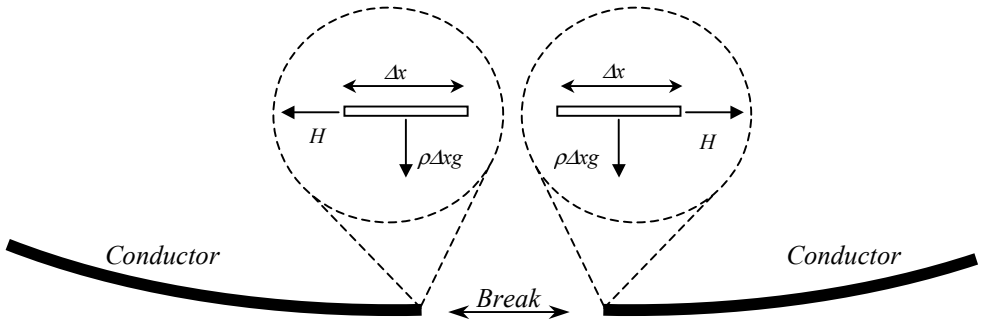

Figure A2.1: Forces acting on broken ends of lines

The method of this derivation is based on the principle that the cable profile and position will always change to the next lowest possible potential energy state. This

will be true if there is no initial kinetic energy and elastic movement is insignificant. However, the conductor profile must adhere to the following two limitations:

(a) The broken end of the conductor must stay horizontal since no resulting momentum is acting on element on the end of the line.

(b) The length of the conductor is constant.

Consider the previous illustration in Figure (A2.1). The profile of the conductor can be calculated by applying a horizontal force, equal to the cable tension before breaking, at the broken end of the conductor (see inset in Figure A2.1). This position is seen as the steady state position before breaking. If the horizontal force is reduced, the conductor profile will change to a lower potential energy level. The only difference between this profile and the original profile is the higher tension present in the cable. This profile will therefore be equal to a healthy conductor with the same length as the original sag span but with a smaller span length. Reducing the horizontal force even further or reducing the span length of a healthy conductor simulates the next lower potential energy level. The locus of the conductor movement after a break in the conductor will always follow the lowest possible energy levels. The locus of the end point of the conductor is therefore the same as the locus of the midpoint of a sag span conductor with a reducing span length.

Equation (A2.1) describes the sag profile of a healthy conductor of an overhead line under steady state conditions [65].

$$f(x') = \frac{\rho x'^2}{2H} \tag{A2.1}$$

In equation (A2.1), ρ is defined as the mass per unit length of the conductor and H the cable tension. The origin of the Cartesian axes for equation (A2.1) is defined to be at the minimum point of the span at $x'=0$. We now define a new set of Cartesian axes with the origin at the fixed end of the conductor. This formula will also be a parabolic equation that crosses the Y-axis at the origin. Equation (A2.2) gives the general parabolic equation for the conductor profile relative to the new axis.

$$f(x) = ax^2 + bx \tag{A2.2}$$

The first derivative of $f(x)$ will zero at the centre of the sag span.

If the variable X is the value of x at the centre of the span, then

$$\left.\frac{df}{dx}\right|_{x=X} = 2aX + b = 0 \tag{A2.3}$$

Therefore

$$b = -2aX \tag{A2.4}$$

The sag at this point is also known and is described by Equation (A2.1). The unknown constant *a* can be calculated if both Equations (A2.1) and (A2.4) are substituted into equation (A2.2) for *x=X*.

$$f(X) = aX^2 - 2aX \cdot X = -\frac{\rho X^2}{2H}$$

Hence,

$$a = \frac{\rho}{2H}$$

The value of *b* is determined by substituting the expression for *a* into equation (A2.4).

$$b = -2aX = -2\left(\frac{\rho}{2H}\right)X = -\frac{\rho X}{H}$$

The line sag profile can therefore be described by equation (A2.5) with the origin of the x-axis at the fixed end of the conductor.

$$f(x) = \left(\frac{\rho}{2H}\right)x^2 - \left(\frac{\rho X}{H}\right)x \tag{A2.5}$$

Equation (A2.5) describes a sag span profile under steady state conditions in a Cartesian axis with the origin at the fixed end of the conductor. The position of the broken end is given by equation (A2.5) for *x=X*. The value of the reducing equivalent cable tension *H* during the falling of the conductor is unknown. The true length of the conductor is known and described by equation (A2.6) [65].

$$L \approx x\left(1 + \frac{x^2\rho^2}{6H}\right) \tag{A2.6}$$

When $x = X$ is substituted into equation (A2.6).

$$L \approx X\left(1 + \frac{X^2\rho^2}{6H}\right)$$

This expression can be further simplified to determine the tension *H* as a function of the conductor length and span length.

$$6HL = 6HX + X^3\rho^2$$

$$H = \sqrt{\frac{X^3 \rho^2}{6(L-X)}} \tag{A2.7}$$

The expression for the cable tension (equation (A2.7)) can now be substituted back into equation (A2.5) to eliminate the unknown value of the cable tension *H*.

$$f(X) = \left(\frac{\rho}{2H}\right)X^2 - \left(\frac{\rho X}{H}\right)X = -\frac{\rho X^2}{2H} = -\frac{\rho X^2}{2\sqrt{X^3\rho^2/6(L-X)}}$$

$$f(X) = -\frac{\rho X^2 \sqrt{6(L-X)}}{2\rho X^{3/2}}$$

$$f(X) = -\sqrt{\frac{3}{2}X(L-X)} \tag{A2.8}$$

This equation for conductor sag is only a function of the distance to the centre point and constant conductor length. This equation will therefore also describe the locus of the broken end of a perfect non-elastic cable.

Gravitational forces are the only vertical forces acting on the broken end of the conductor. The second derivative of this equation to time will give the downward acceleration of the conductor and should be equal to the gravitational constant *g* since no other vertical forces except gravitation are present on this element.

$$\frac{d^2 f(X)}{dt^2} = g \tag{A2.9}$$

$$f(X) = \int_0^t \left(\int_0^t -g \cdot dt \right) \cdot dt = \frac{1}{2}gt^2 + C_1 t + C_2 \tag{A2.10}$$

The downward velocity of the conductor at *t=0* is zero. The integration constant C_1 for the first integration is therefore zero. The initial condition for the second integral is equal to the initial sag before the breaking of the conductor. This initial sag is defined as D_0 ($D_0 = C_2$). Equation (A2.10) is substituted into equation (2.8) to obtain equation (A2.11).

$$f(X) = -\sqrt{\frac{3}{2}X(L-X)} = \frac{1}{2}gt^2 + D_0$$

Rearranging the above equation:

$$X^2 - LX + \left(\frac{1}{6}g^2t^4 + \frac{2}{3}gt^2 D_0 + \frac{2}{3}{D_0}^2\right) = 0$$

and

$$X = \frac{1}{2}\left(L \pm \sqrt{L^2 - \frac{2}{3}g^2t^4 - \frac{8}{3}gt^2D_0 - \frac{8}{3}{D_0}^2} \right) \tag{A2.11}$$

Equation (A2.11) is checked using by comparing it with equation (A.12) at time *t=0*. Equation (A2.12) from [65] describes the conductor length as a function of the sag and span length.

$$L - S = D^2\left(\frac{8}{3S} \right) \tag{A2.12}$$

Equation (A2.13) is therefore describes the horizontal movement of the broken end of a conductor after breaking.

$$X(t) = \frac{1}{2}\left(L + \sqrt{L^2 - \frac{2}{3}g^2t^4 - \frac{8}{3}gt^2D_0 - \frac{8}{3}{D_0}^2} \right) \tag{A2.13}$$

Calculation of the contraction speed of the conductor:

The elastic force due to compression or stretching is defined by equation (A2.14).

$$H = \frac{EA}{L}\Delta\ell = k \times \Delta\ell \tag{A2.14}$$

In equation (A2.14), E represents the Young-Modulus, A the cross sectional area of the conductor, L the static length of the object under specific conditions and $\Delta\ell$ the amount of stretching due to extra forces other than that applied under the original steady state conditions. The constant H in equation (A2.14) represents the applied force that causes the stretching of the object.

Figure A2.2 shows a typical stretched conductor. The variable z is defined as the amount of retraction while $\Delta\ell$ indicates the total amount of stretching before conductor breaking.

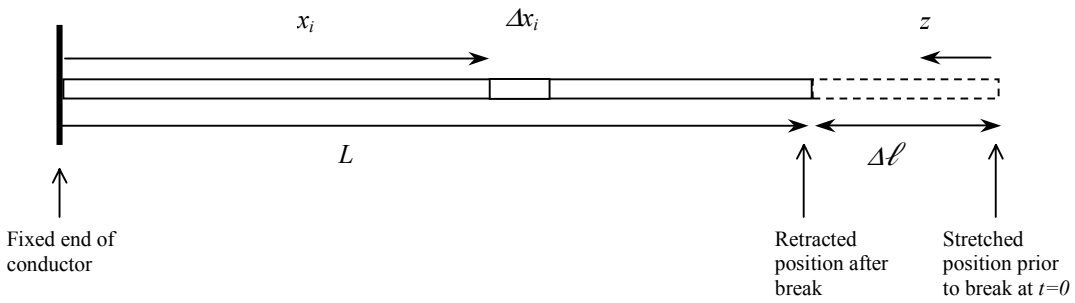

Figure A2.2: Definition of variables for a typical stretched conductor during retraction.

Equation (A2.15) is a general description of the conductor movement based on an energy balance equation that ignores wind resistance, cable stiffness and heat generation during the retraction.

$$E_p(t=0) = E_p(t=t_0) + \sum_i E_{k(i)}(t=t_0) \tag{A2.15}$$

In equation (A1.15), E_p is the elastic potential energy and $E_{k(j)}$ is the kinetic energy of a specific line element i. Equation (A2.16) is a more detailed equation based on equation (A2.15) that describes the dynamic properties of a conductor during the breaking of the conductor

$$\frac{1}{2}k(\Delta\ell)^2 = \frac{1}{2}k(\Delta\ell - z)^2 + \sum_{i=0}^{n}\frac{1}{2}(\Delta x_i\rho)\left(\frac{dx_i}{dt}\right)^2 \tag{A2.16}$$

It is shown in paragraph 5.1.2 that the speed of wave propagation in a cable is $2\text{x}10^6$m/s. This is a relativistic speed that is a lot faster than the likely speed of retraction of the cable. The tension in the cable will reduce to zero almost immediately after breaking. It can therefore be assumed that the retraction speed of each element i in of length Δx_i is directly proportional to the specific element's distance from the fixed point as shown by equation (A2.17).

$$\frac{dx_i}{dt} = -\frac{x_i}{L}\times\frac{dz}{dt} \tag{A2.17}$$

The speed of the individual line elements (Equation (A2.17) is substituted into equation (A2.16).

$$\frac{1}{2}k(\Delta\ell)^2 = \frac{1}{2}k(\Delta\ell - z)^2 + \sum_{i=0}^{n}\frac{1}{2}(\Delta x_i\rho)\left(-\frac{x_i}{L}\times\frac{dz}{dt}\right)^2$$

$$\frac{1}{2}k(\Delta\ell)^2 = \frac{1}{2}k(\Delta\ell - z)^2 + \int_0^L \frac{\rho x^2}{2L^2}\left(\frac{dz}{dt}\right)^2 dx$$

$$\frac{1}{2}k(\Delta\ell)^2 = \frac{1}{2}k(\Delta\ell - z)^2 + \frac{\rho L^3}{6L^2}\left(\frac{dz}{dt}\right)^2$$

$$\left(\frac{dz}{dt}\right)^2 = \left(\frac{3k}{\rho L}\right)\left(2\Delta\ell z - z^2\right) \tag{A2.18}$$

But k is described by equation (A2.14) and the variable v_z is also defined as the horizontal speed of the conductor. Equation (A2.18) is now simplified to equation (A2.19) using above-mentioned relationships.

$$v_z{}^2 = \left(\frac{3EA}{\rho L^2}\right)\left(\frac{2HL}{AE}z - z^2\right)$$

$$v_z = \sqrt{\left(\frac{3EA}{\rho L^2}\right)\left(\frac{2HL}{AE}z - z^2\right)} \tag{A2.19}$$

Equation (A2.19) describes the horizontal speed of the broken end of a conductor and this equation is only valid until $z=\Delta\ell$. Hence, no retraction forces will be present for $z>\Delta\ell$ and it can be assumed that the broken end of the conductor will retain it speed for short displacements beyond $z=\Delta\ell$ as long as the bending of the cable is insignificant in comparison to the total length of the cable.

The final speed is calculated substituting the value of $\Delta\ell$ from Equation (A2.14) into Equation (A2.19). Equation (A2.20) therefore describes the final maximum speed value.

$$v_{z_{MAX}} = \sqrt{\left(\frac{3EA}{\rho L^2}\right)\left(\frac{2HL}{AE}\left(\frac{HL}{EA}\right) - \left(\frac{HL}{EA}\right)^2\right)}$$

$$v_{z_{MAX}} = \sqrt{\frac{3}{\rho EA}} \cdot H \tag{A2.20}$$

The time required to reach the maximum speed is calculated by integrating equation (A2.18). The integration of equation (A2.18) is shown below:

Equation (2.18) gives: $$\left(\frac{dz}{dt}\right)^2 = \left(\frac{3k}{\rho L}\right)\left(2\Delta\ell z - z^2\right)$$

Rearranging $$dz = \pm\sqrt{\left(\frac{3k}{\rho L}\right)\left(2\Delta\ell z - z^2\right)}dt$$

Integrating $$\int_0^{\Delta\ell} \frac{dz}{\sqrt{\left(2\Delta\ell z - z^2\right)}} = \pm\int_0^t \sqrt{\frac{3k}{\rho L}}\,dt$$

The general solution of the integral on the left hand side of the equation is [63]:

$$\int \frac{dx}{\sqrt{(ax+b)(px+q)}} = \begin{cases} \frac{2}{\sqrt{ap}} \ln\left(\sqrt{a(px+q)} + \sqrt{p(ax+b)}\right) \\ \frac{2}{\sqrt{-ap}} \tan^{-1}\left(\sqrt{\frac{-p(ax+b)}{a(px+q)}}\right) \end{cases}$$

The first general solution will give imaginary results while the second solution will produce real solutions.

$$\pm\sqrt{\frac{3k}{\rho L}} \times t\Big|_0^{t_M} = \frac{2}{\sqrt{1}} \tan^{-1}\left(\sqrt{\frac{-\left(-z+2\Delta\ell\right)}{-z}}\right)\Bigg|_0^{\Delta\ell}$$

$$\pm\sqrt{\frac{3k}{\rho L}} \times t_M = \frac{2}{\sqrt{1}} \tan^{-1}\left(\sqrt{\frac{\left(-\Delta\ell+2\Delta\ell\right)}{\Delta\ell}}\right) - \frac{2}{\sqrt{1}} \tan^{-1}\left(\sqrt{\lim_{z\downarrow 0}\frac{\left(-z+2\Delta\ell\right)}{z}}\right)$$

$$\pm\sqrt{\frac{3k}{\rho L}} \times t_M = 2\tan^{-1}\left(\sqrt{1}\right) - 2\left(\frac{\pi}{2}\right)$$

$$\pm\sqrt{\frac{3k}{\rho L}} \times t_M = 2\left(\frac{\pi}{4}\right) - 2\left(\frac{\pi}{2}\right)$$

$$t_M = \sqrt{\frac{\rho L}{3k}} \times \left(\frac{\pi}{2}\right) \qquad \text{(A2.21)}$$

The elastic constant k is obtained from equation (A2.21) by substituting the value of k, as defined by equation (A2.14), into equation (A2.21)

$$t_M = \sqrt{\frac{\rho L^2}{3EA}} \times \left(\frac{\pi}{2}\right)$$

$$t_M = \frac{\pi L}{2} \cdot \sqrt{\frac{\rho}{3EA}} \qquad \text{(A2.23)}$$

Equation (A2.23) is an expression for the time from the instant of conductor break to the instant when maximum velocity is obtained.

Bibliography

[1] T. Funabashi, H. Otoguro, Y. Mizuma, L. Dubè, M. Kizilcay, and A. Ametani, "Influence of fault arc characteristincs on the accuracy of digital fault locators," *IEEE Transactions on Power Delivery*, vol. 16, pp. 195-199, 2001.

[2] Z. Radojevic, V. Terzija, and M. Djuric, "Multipurpose overhead lines protection algorithm," *IEE Proceedings-Generation Transmission and Distribution*, vol. 146, pp. 441-445, 1999.

[3] L. O. Barthold, R. E. Clayton, I. S. Grant, V. J. Longo, J. R. Stewart, and D. D. Wilson, *Transmission line reference book (EPRI Research Project 260)*. Palo Alto, California: Electric Power Research Institute, 1978.

[4] L. Li and M. A. Redfern, "A review of techniques to detect downed conductors in overhead distribution systems," *IEE Proceedings : Developments in Power System Protection*, vol. 479, pp. 169-172, 2001.

[5] J. S. Thorp, "Digital Relaying," in *Electrical Power Engineering Handbook*, *The Electrical Engineering Handbook*, L. L. Grigsby, Ed.: CRC Handbook Publishers &IEEE Press, 2001, pp. 9/45-9/62.

[6] Z. M. Radojevic, V. V. Terzija, and B. Djuric, "Numerical algorithms for overhead lines arcing faults and distance and directional protection," *IEEE Transactions on Power Delivery*, vol. 15, pp. 31-37, 2000.

[7] T. Takagi, Y. Yamakoshi, M. Yamaura, R. Kondow, and T. Matsushima, "Development of a new type fault locator using the one-terminal voltage and current data," *IEEE Transactions on Power Apparatus and Systems*, vol. 101, pp. 2892-2898, 1982.

[8] T. Takagi, Y. Yamakoshi, J. Baba, K. Uemura, and T. Sakaguchi, "A new algorithm of an accurate fault location for EHV/UHV transmission lines: Part I - Fourier transformation method," *IEEE Transactions on Power Apparatus and Systems*, vol. 100, pp. 1316-1322, 1981.

[9] A. Wiszniewski, "Accurate fault impedance locating algorithm," *IEE Proceedings C: Generation, Transmission and Distribution*, vol. 130, pp. 311-314, 1983.

[10] L. Eriksson, M. M. Saha, and G. D. Rockefeller, "An accurate fault locator with compensation for apparent reactance in the fault resistance resulting from remote-end infeed," *IEEE Transactions on Power Apparatus and Systems*, vol. 104, pp. 424-436, 1985.

[11] M. S. Sachdev and R. Agarwal, "IEE Conference Publication 249," *Development in Power-System Protection, Third International Conference on*, pp. 180-184, 1985.

[12] M. S. Sachdev and R. Agarwal, "A technique for estimating transmission line fault locations from digital impedance ralay measurements," *IEEE Transactions on Power Delivery*, vol. 3, pp. 121-129, 1988.

[13] V. Cook, "Fundamental aspects of fault location algorithms used in distance protection," *IEE Proceedings C: Generation, Transmission and Distribution*, vol. 133, pp. 359-368, 1986.

[14] A. O. Ibe and B. J. Cory, "Fault location algorithm for multiphase power lines," *IEE Proceedings C: Generation, Transmission and Distribution*, vol. 134, pp. 43-50, 1987.

[15] B. Jeyasurya and M. A. Rahman, "Simulation of transmission line fault locators in a personal computer," *IEEE Transactions on Industry Applications*, vol. 27, pp. 299-302, 1991.

[16] B. Jeyasurya and M. A. Rahman, "Accurate fault location of transmission lines using microprocessors," *Developments in Power Protection, 1989., Fourth International Conference on*, pp. 13-17, 1989.

[17] D. L. Waikar, S. Elangovan, and A. C. Liew, "Symmetrical component based improved fault impedance estimation method for digital distance protection," *Electric Power System Research*, vol. 26, pp. 143-147, 1993.

[18] A. G. Phadke, T. Hlibka, and M. Ibrahim, "Fundamental basis for distance relaying with symmetrical components," *IEEE Transactions on Power Apparatus and Systems*, vol. 96, pp. 635-646, 1977.

[19] D. L. Waikar and S. Elangovan, "Fault impedance estimation algorithm for digital distance relaying," *IEEE Transactions on Power Delivery*, vol. 9, pp. 1375-1383, 1994.

[20] A. T. Johns, P. J. Moore, and R. Whittard, "New technique for the accurate location of earth faults on transmission systems," *IEE Proceedings C: Generation, Transmission and Distribution*, vol. 142, pp. 119-127, 1995.

[21] Y. Liao and S. Elangovan, "Improved symmetrical component-based fault estimation for digital distance protection," *IEE Proceedings C: Generation, Transmission and Distribution*, vol. 145, pp. 739-746, 1998.

[22] M. M. Saha, K. Wikstrom, and E. Rosolowski, "New accurate fault location algorithm for parallel lines," *IEE Proceedings: Developments in Power System Protection*, vol. 479, pp. 407-410, 2001.

[23] M. Akke and J. S. Thorp, "Improved estimatates from the differential equation algorithm by median post-filtering," *Developments in Power System Protection, Sixth Internation Conference*, vol. 434, pp. 235-238, 1997.

[24] T. Segui, P. Bertrand, M. Guillot, H. Hanchin, and P. Bastard, "Fundamental basis for distance relaying with parametrical estimation," *IEEE Transactions on Power Delivery*, vol. 16, pp. 99-104, 2001.

[25] P. Bornard and J. C. Bastide, "A prototype of multiprocessor based distance relay," *IEEE Transactions on Power Apparatus and Systems*, vol. 101, pp. 491-498, 1982.

[26] M. Fikri and M. El-Sayed, "New Algorithm for Distance Protection of High Voltage Transmission Lines," *IEE Proceedings C: Generation, Transmission and Distribution*, vol. 135, pp. 436-440, 1988.

[27] V. V. Terzija and H. J. Koglin, "Long arc in free air: testing, modeling and parameter estimation: Part I," *Harmonics and Quality of Power, 2000. Proceedings. Ninth International Conference on*, vol. 2, pp. 404-409, 2000.

[28] V. V. Terzija and H. J. Koglin, "Long arc in free air: testing, modeling and parrameter estimation: Part II," *Harmonics and Quality of Power, 2000. Proceedings. Ninth International Conference on*, vol. 2, pp. 481-486, 2000.

[29] B. Djuric and V. V. Terzija, "A new approach to the arcing faults detection for fast autoreclosure in transmission systems," *IEEE Transactions on Power Delivery*, vol. 10, pp. 1793-1798, 1995.

[30] C. G. Wester, "High impedance fault detection on distribution systems," *Rural Electric Power Conference, 42nd Annual Conference*, pp. C5/1-C5/5, 1998.

[31] A. Lazkano, J. Ruiz, E. Aramendi, L. A. Leturiondo, and J. A. Gonzalez, "Study of high impedance fault detection in levante area in Spain," *Harmonics and Quality of Power, Proceedings, Ninth International Conference on*, vol. 3, pp. 1005-1010, 2000.

[32] J. Carr, "Detection of high impedance fault on multi-grounded primary distribution system," *IEEE Transactions on Power Apparatus and Systems*, vol. 100, pp. 2008-2016, 1981.

[33] C. Huang, H. Chu, and M. Chen, "Algorithm comparison for high impedance fault detection based on staged fault test," *IEEE Transactions on Power Delivery*, vol. 3, pp. 1427-1435, 1988.

[34] H. Calhoun, M. T. Bishop, C. H. Eichler, and R. E. Lee, "Development and testing of an electro-mechanical relay to detect fallen distribution conductors," *IEEE Transactions on Power Apparatus and Systems*, vol. 101, pp. 1643-1650, 1982.

[35] E. A. Atwell, A. W. Shaffer, D. I. Jerrings, and J. R. Linders, "Performance testing of the Nordon high impedance ground fault detector on a distribution feeders," *Rural Electric Power, Conference 1990, Papers Presented at the 34th Annual Conference*, pp. C6/1-C6/7, 1990.

[36] M. Aucoin, B. D. Russell, and C. L. Benner, "High Impedance fault detection for industrial power systems," *Industrial Application Society Annual Meeting 1989, Conference*, vol. 2418, pp. 1788-1792, 1989.

[37] M. Aucion, J. Zeigler, and B. D. Russell, "Feeder protection and monitoring system, Part II: Staged fault test demonstration," *IEEE Transaction on Power Apparatus and Systems*, vol. 104, pp. 1456-1462, 1985.

[38] E. C. Senger, W. Kaiser, J. C. Santos, P. M. S. Burt, and C. V. S. Malagodi, "Broken conductors protection system using carrier communication," *IEEE Transactions on Power Delivery*, vol. 15, pp. 525-530, 2000.

[39] C. L. Benner, P. Carswell, and B. D. Russell, "Improved Algorithm for detecting arcing faults using random fault behavior," *Electric Power System Research*, vol. 17, pp. 49-56, 1989.

[40] C. J. Kim and B. D. Russell, "Analysis of distribution disturbances and arcing faults using the crest factor," *Electric Power System Research*, vol. 35, pp. 141-148, 1995.

[41] C. H. Kim, H. Kim, R. K. Aggarwal, and A. T. Johns, "Wavelet transform in the accurate detection of high impedance arcing faults in high voltage transmission lines," *Development in Power System Protection, Seventh International Conference on*, vol. 479, pp. 422-425, 2001.

[42] A. A. Girgis, W. Chang, and E. B. Makram, "Analysis of high impedance fault generated signals using kalman filtering approach," *IEEE Transactions on Power Delivery*, vol. 5, pp. 1714-1724, 1990.

[43] A. F. Sultan, G. W. Swift, and D. J. Fedirchuk, "Detecting arcing downed - wires using fault current flickers and half cycle asymmetry," *IEEE Transactions on Power Delivery*, vol. 9, pp. 461-470, 1994.

[44] M. Aucion and R. H. Jones, "High impedance fault detection implementation issues," *IEEE Transactions on Power Delivery*, vol. 11, pp. 139-148, 1996.

[45] C. L. Benner and B. D. Russell, "Practical high-impedance fault detection on distribution feeders," *IEEE Transactions on Industry Applications*, vol. 33, pp. 635-640, 1997.

[46] L. van der Sluis, *Transients in Power Systems*. Chichester, UK: John Wiley & Sons, Ltd, 2001.

[47] H. Maecker, *Theory of thermal plasma and apllication to observed phenomena*. Armindale, Australia: The University of New England, 1964.

[48] L. van der Sluis, W. R. Rutgers, and C. G. A. Koreman, "A physical arc model for the simulation of current zero behaviour of high voltage circuit breakers," *IEEE Transactions on Power Delivery*, vol. 7, pp. 1016-1024, 1992.

[49] A. M. Cassie, "Arc rupture and circuit severity: A new theory," CIGRE 102, 1939.

[50] O. Mayr, "Beitraege zur theorie des statischen und dynamischen lichtbogens," *Archiv fur elektrotechnik*, vol. 37, pp. S588-S608, 1943.

[51] T. E. Browne, "An approach to mathematical analysis of a-c arc extinction in circuit breakers," *AIEE Transactions*, vol. 78, pp. 1508-1517, 1959.

[52] K. J. Cornick, Y. M. Ko, and B. Pek, "Power system transients caused by arcing faults," *IEE Proceedings C: Generation, Transmission and Distribution*, vol. 128, pp. 18-27, 1981.

[53] A. T. Johns, R. K. Aggarwal, and Y. H. Song, "Improved techniques for modeling fault arcs on faulted EHV transmission systems," *IEE Proceedings C: Generation, Transmission and Distribution*, vol. 141, pp. 148-154, 1994.

[54] A. D. Stokes and W. T. Oppenlander, "Electric arcs in open air," *Journal of Physics D: Appl. Phys.*, vol. 24, pp. 26-35, 1991.

[55] Y. Goda, M. Iwata, K. Ikeda, and S. Tanaka, "Arc voltage characteristics of high current fault arcs in long gaps," *IEEE Transactions on Power Delivery*, vol. 15, pp. 791-795, 2000.

[56] H. Kudo, H. Sasaki, K. Seo, M. Takahashi, K. Yoshida, and T. Maeda, "Implimentation of a digital distance relay using an interpolated integral solution of a differential equation," *IEEE Transactions on Power Delivery*, vol. 3, pp. 1475-1484, 1988.

[57] H. Dommel, "Digital computer solution of electromagnetic transients in single and multiple networks," *IEEE Transactions on Power Apparatus and Systems*, vol. 88, 1969.

[58] A. T. Johns and S. K. Salman, "Differential equation based techniques," in *Digital Protection for Power Systems*, vol. 15, *IEE Power Series*, A. T. Johns and J. R. Platts, Eds. London: Peter Peregrinus Ltd., 1995, pp. 103-107.

[59] H. S. May, "The design of overhead electric lines for improved reliability," *Overhead Line Design and Construction: Theory and Practice, 1989, International Conference on*, pp. 1-5, 1988.

[60] M. Irvine, *Cable Structures*. New York: Dover Publications, 1992.

[61] R. A. Serway, *Physics for scientists and engineers with modern physics*, Fourth ed: Sauders College Publishing, 1996.

[62] A. B. Mehrabi and H. Tabatabai, "Unified finite difference formulation for free vibration of cables," *Journal of Structural Engineering*, pp. 1313-1322, 1998.

[63] R. S. Spiegel and J. Liu, *Mathematical Handbook of Formulas and Tables*, Second ed. Singapore: McGraw Hill, 1999.

[64] "Dulmison Product Catalogue," in *<http://www.dulmison.com.au/section22/22-7_files/22-7.htm>*: Dulmison Australia, 14/05/2002.

[65] D. A. Douglass and R. Thrash, "Sag and Tension of Conductor," in *Electrical Power Engineering Handbook*, L. L. Grigsby, Ed.: CRC Handbook Publishers & IEEE Press., 2001, pp. 4/89-4/129.

[66] V. K. Mehta, *Principles of Power Systems*. New Delhi: S.Chand&Company Ltd., 2001.

[67] *AS 2006-1986. High voltage ac switchgear and controlgear - circuit breakers for rated voltages above 1000V*.

[68] A. A. Tjavaras, Q. Zhu, Y. Liu, M. S. Triantafyllou, and D. K. P. Yue, "The mechanincs of highly-extensible cables," *Journal of Sound and Vibration*, vol. 213, pp. 709-737, 1998.

[69] J. R. Smith, "Overhead Lines," in *Modern Power Station Practice (third edition)*, vol. K, D. J. Littler, E. J. Davies, H. E. Johnson, F. Kirkby, P. B. Myerscough, and W. Wright, Eds. Singapore: Pergamon Press, 1991, pp. 65-125.

[70] G. G. Karaday and R. G. Farmer, "Insulators and Accessories," in *Electrical Power Engineering Handbook*, L. L. Grigsby, Ed.: CRC Handbook Publishers & IEEE Press, 2001, pp. 4/23 - 4/42.

[71] A. M. Loredo-Souza and A. G. Davenport, "Wind tunnel aerolastic studies on the behaviour of two parallel cables," *Journal of Wind Engineering and Industrial Aerodynamics*, vol. 90, pp. 407-413, 2002.

[72] *AS/NZS 61000.3.7:2001. Limits - Assessment of emission limits for fluctuating loads in MV and HV power systems*.

[73] Nu-Lec Pty Ltd., *Technical Manual for N12, N24 and N36 Pole Mounted Circuit Breaker*, 1999.